Rational Design of Electrolyte for Stable and Low-Temperature Zinc-Ion Battery

by

Han Huang

A thesis submitted in partial fulfillment of the requirements for the degree of

Master of Science

Department of Mechanical Engineering
University of Alberta

Abstract

Energy storage technology greatly influences human daily life, including the development of portable electronic devices, electric vehicles, smartwatches, etc. Researchers are seeking renewable and sustainable energy storage systems due to environmental concerns. Aqueous zinc-ion batteries are a promising energy storage system due to their low cost, high safety and environmentally friendly. The metallic Zn has the advantages of low redox potential and high theoretical capacity. However, the Zn anode suffers from serious problems with Zn dendrite growth and side reaction. The cycling stability and electrochemical performance are affected by these problems significantly. Adding organic solvent in electrolytes is a promising solution because the organic molecules can enter the solvation structure and replace water molecules, reducing water activity and inhibiting the hydrogen evolution reaction. Certain organic molecules possibly form the protective layer from the reduction reaction in the electrolyte, which the protective layer is derived from electrochemical reactions and is beneficial for uniform Zn^{2+} deposition.

Chapter 1 is an overview of electrolyte engineering in zinc-ion batteries. The mechanism of Zn dendrite formation, hydrogen evolution reaction, and Zn corrosion are discussed in detail. In addition, the advantages of SEI layer formation and solvation structure manipulation are introduced. The review of electrolyte engineering is divided into three parts: highly concentrated electrolytes, organic solvents, and additives. In the additive section, the metal-ion additive, SEI layer forming additive, and surfactant additive are discussed. All these electrolyte engineering

strategies are summarized and demonstrated with theoretical calculation and electrochemical performance. Challenges and objectives are also stated.

Chapter 2 is the methodology for analyzing the solvation structure and stability of zinc ion batteries, including physical characterizations, electrochemical characterizations and computational simulations.

Chapter 3 is a complete research project of enabling a stable zinc-ion battery by adding an organic solvent to the electrolyte. Diglyme (G2) is chosen as the organic solvent. It has affected the Zn^{2+} solvation structure, which inhibits the formation of Zn dendrite and hydrogen evolution reactions. Furthermore, the G2 molecule participates in the reduction reaction on the electrolyte-electrode interface, forming an organic-inorganic (ZnF_2-$ZnCO_3$- $ZnSO_3$) layer on the Zn surface. The electrochemical performance shows high columbic efficiency and excellent stable and long cycling performance. In addition, the G2 organic solvent also expands the cell operating temperature to -18°C. The Zn//I-AC full cell with G2 solvent is capable in low-temperature conditions. A high columbic efficiency is also obtained at a low temperature.

Preface

Han Huang originally writes this thesis under the supervision of Dr. Ge Li from the Mechanical Engineering Department at the University of Alberta.

Chapter 1 involves the literature review of my two years master's program.

Chapter 3 is a complete article that tends to publish in the future. The article is fully written by myself. Ph.D. student Pengcheng Li and Ph.D. student Ziwei Zhao have inspired me and assisted with the theoretical calculation. Dr. Ge Li has been providing advice and feedback for my work.

This thesis is dedicated to
my parents, Jianjun Huang and Fengyin Zhang,
my sister Jing Huang.
Thanks for their love and support.

Acknowledgments

First, I would like to sincerely thank my professor Ge Li. She gave me a lot of help and support in my master's career and provided me with many practical suggestions for my research topic. She exchanged ideas and knowledge with me and regulated my working behaviour. This is a lab experience that is going to benefit my career in the future.

Secondly, I sincerely thank Dr. Xiaolei Wang for giving me suggestions and feedback during each presentation.

Then I would like to sincerely thank Ph.D. students Ziwei Zhao and Pengcheng Li. Ziwei shared lots of skills and knowledge with me. He guided me into the battery career and greatly inspired me for my research topic. Pengcheng taught and assisted me in theoretical calculation for my research. He selflessly shared lots of his ideas and work experiences that helped me overcome difficulties.

I would also like to thank all the group members for their kind support and advice.

At last, I would like to thank my family for supporting my study and living in Edmonton. Their loves are the motivation for me.

Han Huang, Jun 2023

List of Contents

List of Tables

3

List of Figures

Figure 34. (a) Chronoamperometry (CA) with different volume ratios of G2 in the electrolyte. (b) Coulombic efficiency (CE) of Zn//Cu asymmetric cells in H_2O(1) - G2(1) electrolyte at 40°C.75

List of Abbreviations

Chapter 1

AZIBs	Aqueous zinc ion batteries
LIBs	Lithium-ion batteries
SEI	Solid electrolyte interface
DFT	Density functional theory
MD	Molecular Dynamic
CE	Coulombic efficiency
HER	Hydrogen evolution reaction
NMR	Nuclear magnetic resonance
SEM	Scanning electron microscope
XRD	X-ray Diffraction
LSV	Linear sweep voltammetry
DMSO	Dimethyl sulfoxide
DMC	Dimethyl carbonate
DME	1,2-dimethoxyethane
EG	Ethylene glycol
DN	Gutmann donor number
XANES	X-ray absorption near-edge structure
ft-EXAFS	X-ray absorption fine structure
CA	Chronoamperograms
LUMO	Lowest unoccupied molecular orbital
XPS	X-ray photoelectron spectroscopy
TEP	Triethyl phosphate
GO	Graphene oxide
TMA	Triethylmethylammonium
TBA_2SO_4	Tetrabutylammonium sulfate
SPS	3,3′-dithiodipropane sulfonate
SL	Sodium lignosulfonate
PEO	Polyethylene oxide

Chapter 3

G2	Diglyme
SHE	Standard hydrogen electrode
DMA	N-dimethyl acetamide
AC	Activated Carbon
DI water	Deionized water
EIS	Electrochemical impedance spectroscopy
RDFs	Radial distribution functions
CV	Cyclic voltammetry
VASP	Vienna Ab-initio Simulation Package
GGA	Generalized gradient approximation

PBE	Perdew-Burke-Ernzerhof
HUMO	Highest occupied molecular orbital

Chapter 1. Introduction of aqueous zinc ion battery

Electrolyte engineering of Zinc anode protection for aqueous zinc-ion batteries

1.1 Abstract

The increasing need for electrical energy storage has sparked a search for advanced battery solutions. The aqueous zinc-ion batteries (AZIBs) as potential alternatives to lithium-ion batteries (LIBs) have gained significant attention for their attractive features of low cost, high safety, and environmentally friendly. Significant progress has been made in exploring stable zinc anodes. However, several fundamental challenges regarding zinc dendrite growth, hydrogen evolution reaction, and zinc corrosion still hinder the advancement of zinc-based energy storage systems. The electrolyte plays a critical role in batteries, as its properties significantly influence energy storage mechanisms, reaction kinetics, side reactions, and cycling stability in ZIBs. Adjusting the electrolyte composition directly impacts overall performance. This review focuses on protecting zinc metal anode by performing electrolyte engineering from two aspects: solvation structure modification and solid electrolyte interface (SEI) formation. Critical issues and challenges of zinc metal anode will be discussed in detail. Previously reported progresses are collected and analyzed through theoretical simulations (DFT calculation, MD simulation, etc.) and electrochemical performances (morphology, cycling performance, etc.).

1.2 Background

Nowadays, since the advancement of energy storage technology, various applications such as electric vehicles and portable electronic devices have emerged in every single person's life, which significantly benefits and convenient the lifestyle of everyone. Lithium-based batteries are the most mature and market-successful energy storage devices due to their high energy density and high voltage output. However, the limited lithium metal resources and its relatively high cost have become a problem for sustainable development. Besides, the flammability of organic electrolytes in lithium-based batteries is a concern for daily use. Therefore, a more sustainable alternative must be discovered, and aqueous zinc-ion batteries (AZIBs) have emerged.

AZIBs have emerged as one of the most promising energy storage systems for great safety and electrochemical performance. The mechanism of AZIBs can be summarized as reversible intercalation. During discharge process, the zinc metal anode will lose electron and dissolve into electrolyte. All the metal ions and salt ions are transported through the electrolyte. Electrons are transported through current collectors. The zinc metal ions are eventually intercalated and stored in the cathode material. During charge process, the process is reversed. Metallic Zn as the anode has great stability in the majority of battery environments. The aqueous electrolyte environment avoids flammability, and better safety is obtained. There are much more abundant zinc metal resources on the earth compared to lithium metal resources, which leads to a lower cost of zinc metal. Furthermore, zinc metal has a low redox potential (- 0.76 V *vs* the standard hydrogen electrode (SHE) and a high theoretical capacity (820 mAh g^{-1}). However, besides all these advantages, AZIBs suffer from several critical challenges, including zinc dendrite growth, side reactions, and zinc metal corrosion.

1.3 Critical problems on zinc anode-electrolyte interface

Zinc dendrites usually tend to form unevenly on the zinc anode surface during the zinc nucleation process, which is also called the tip effect. The tip effect refers to the phenomenon where protruding tip region is formed during Zn^{2+} diffusion on the anode surface. These tips have higher current density and favorable sites for Zn^{2+} deposition, causing the Zn^{2+} to get together and store up at the same location. Then Zn dendrite forms in this way, and the formed dendrite will attract more Zn^{2+} to deposit on the existing dendrite. Eventually, the dendrite will break through the separator and cause a short circuit in the battery(1). In the zinc aqueous electrolyte, the Zn^{2+} anion tends to interact with water molecules and form a solvation structure of $[Zn(H_2O)_6]^{2+}$ during the Zn^{2+} deposition. The solvation sheath of $[Zn(H_2O)_6]^{2+}$ necessitates a high energy barrier to be overcome for Zn^{2+} desolvation, which results in a high overpotential for water decomposition on the zinc surface(2, 3). Therefore, the hydrogen evolution reaction (HER) happens spontaneously as follows:

$2H^+ + 2e^- \rightarrow H_2$ 0V vs SHE (1)

$Zn^{2+} + 2e^- \rightarrow Zn$ -0.76V vs SHE (2)

The producing hydrogen gas increases the pressure inside the battery and causes an electrolyte leakage. The local PH value has also changed due to the consumption of H^+ and results in an alkaline environment where by-products form as follows (4):

$2H_2O + 2e^- \rightarrow H_2 + 2OH^-$ (3)

$Zn^{2+} + 2OH^- \rightarrow Zn(OH)_2 + 2e^-$ (4)

$Zn(OH)_2 + 2OH^- \rightarrow Zn(OH)_4^{2-}$ (5)

$Zn(OH)_4^{2-} \rightarrow ZnO+H_2O + 2OH^-$ (6)

These by-products of $Zn(OH)_2$ and ZnO form unevenly on the surface, which causes further growth of Zn dendrite. Furthermore, the consumption of zinc metal leads to Zn corrosion, which results in the consumption of active material and self-discharge for the battery. Therefore, it is urgent and important to reduce the impact of the solvation effect and promote a smoother Zn^{2+}

deposition(4-6).

1.4 Electrolyte Engineering

The electrolyte is the medium for ion diffusion and mass transport between the cathode and anode. It is made up by salt and solvent. For zinc ion batteries, they can use either aqueous solvent or organic solvent for the electrolyte. It has an impact on ionic conductivity, transport kinetic and electrochemical performance for the battery(7, 8). To inhibit the hydrogen evolution reaction and promote uniform Zn^{2+} deposition, it is necessary to remove the active water molecule on the electrode-electrolyte interface and protect the Zn surface. Therefore, novel electrolyte engineering is considered a promising strategy for better Zn^{2+} deposition(9).

In general, the electrolyte engineering will be focusing on the development of additive, solvent and salt. Additive usually function as protective shield on the Zn surface. One of the common additive is SEI forming additive, which performs solid electrolyte interface (SEI) layer(10) on the zinc surface. In the first charge and discharge of lithium batteries, the electrolyte receives electrons and reacts with Li^{+} ions to form an interface that has similar properties as a solid electrolyte. Therefore, people name these kinds of film as solid electrolyte interfaces. These SEI layers act as a protective film on the lithium metal, which lithium ions can pass through the film while electrons cannot. Therefore, the SEI layer has the following advantages: 1. It suppresses further consumption of lithium ions and enhances the lifespan of batteries. 2. It is uniform and isolates the contact between electrodes and electrolyte, which restricts further interfacial reaction in the electrolyte. 3. It suppresses the formation of dendrites and provides more nucleation sites. In turns of aqueous zinc ion batteries, similar ideas can be applied by adding additive or organic solvents in the aqueous electrolyte(13).

The development of solvent is usually applied by using organic solvent in the system, which focus on modifying the solvation structure of $[Zn(H_2O)_6]^{2+}$ (11). The basic idea is to reduce the content of water molecules in the $[Zn(H_2O)_6]^{2+}$ solvation sheath. Therefore, there are fewer water

molecules, and restricted side reactions happen on the zinc surface(14). The water molecules are replaced by either the additive molecules/organic molecules or possible reduction ions in the electrolytes. The modified solvation structure has the following advantages: 1. High coulombic efficiency (CE) and excellent stability will be achieved in the electrochemical performance. 2. It suppresses the side reaction of HER and by-products. 3. It suppresses the growth of Zn dendrite and self-corrosion. The development of salt is usually applied by increasing the salt concentration(12) in the system. The highly concentrated electrolyte has similar ideas of rearranging the solvation structure. By increasing the salt concentration in the electrolyte, a large number of salt ions anions will be forced to enter the inner solvation sheath, and the water molecules will be replaced. Side reactions and the uneven Zn^{2+} deposition will be suppressed.

1.5 Literature review

In this review, electrolyte engineering will be summarized and introduced in the aspects of salt, solvent and additive. The use of highly concentrated electrolytes, organic solvents, and additives will be classified and analyzed by both theoretical simulations and electrochemical performance. The use of additives will be further divided into metal ion additive(15), SEI forming additive, and surfactant additive(9).

1.5.1 Highly concentrated electrolyte

Nowadays, various Zn-salt has been studied and analyzed in zinc-ion battery systems, including $ZnSO_4$, $Zn(CF_3SO_3)_2$ (16), $ZnCl_2$ (17), $Zn(NO_3)_2$, $Zn(TFSI)_2$ (18, 19), etc. Researchers found that the salt concentration of electrolytes is a critical factor that significantly affects the electrochemical performance of batteries(20, 21). By increasing the concentration of salts up to a rational value, the batteries present much better cycling stability and higher CE. Olbasa et al. (22) developed a highly concentrated electrolyte of 4.2M $ZnSO_4$ + 0.1M $MnSO_4$ compared to a low concentrated electrolyte of 2M $ZnSO_4$ + 0.1M $MnSO_4$. Raman spectroscopy in the range from 2700 cm^{-1} to 3400 cm^{-1} is shown in Fig. 1a. The peaks represent the water molecules within the solvation structure with Zn^{2+}. As the concentration of $ZnSO_4$ salt increases from 2M to 4.5M, the peaks slightly shift to a lower frequency. This result indicates fewer water molecules in the solvation structure, which proves that the solvation structure is modified. The water molecules could be replaced by SO_4^{2-} anions in the solution.

The X-ray absorption near-edge spectra are performed in Fig. 1b. The peaks for all the electrolytes with different concentrations are almost the same. The intensity of Zn^{2+} absorbing O_SO_4^{2-} slightly increases as the salt concentration increases. This proves that the Zn^{2+} is more favorable to interact with O_SO_4^{2-} anion in the electrolyte. Then the radial distribution function is simulated, and coordinated numbers are calculated to study the distribution of neighbor molecules and ions in the

Zn^{2+} solvation structure. As presented in Fig. 1c, the Zn-O_H_2O pair distributes at 1.9Å for both electrolytes. The coordination number of 4M electrolyte is 2.98, and the coordination number of 1M electrolyte is 3.91. This indicates that more water molecules are interacting with Zn^{2+} in low-concentrated electrolytes.

In Fig. 1d, the Zn-O_SO_4^{2-} pair displays at 1.5Å for both electrolytes. The coordination number of 4M electrolyte is 1.31, and the coordination number of 1M electrolyte is 0.47. This indicates that there are more SO_4^{2-} anions in the Zn^{2+} solvation structure in highly concentrated electrolytes. Furthermore, the O_SO_4^{2-} displays at a closer distance than the O_H_2O pair toward Zn^{2+}, which leads to a better interaction between Zn^{2+} and SO_4^{2-} anion in the solution. This theoretical simulation proves that the water molecules are replaced by SO_4^{2-} anions in the Zn^{2+} solvation structure, and the $[Zn(H_2O)_6]^{2+}$ solvation sheath is modified for easier Zn^{2+} desolvation. Schematics of Zn^{2+} plating on copper are shown in Fig. 1e and Fig. 1e. Since there are more SO_4^{2-} anions in the solvation structure, there are fewer water molecules that got decomposed on the surface. Hydrogen evolution reaction is suppressed, which also leads to fewer formation of by-products. Therefore, the surface is smooth, and the more uniform Zn^{2+} deposition is attributed.

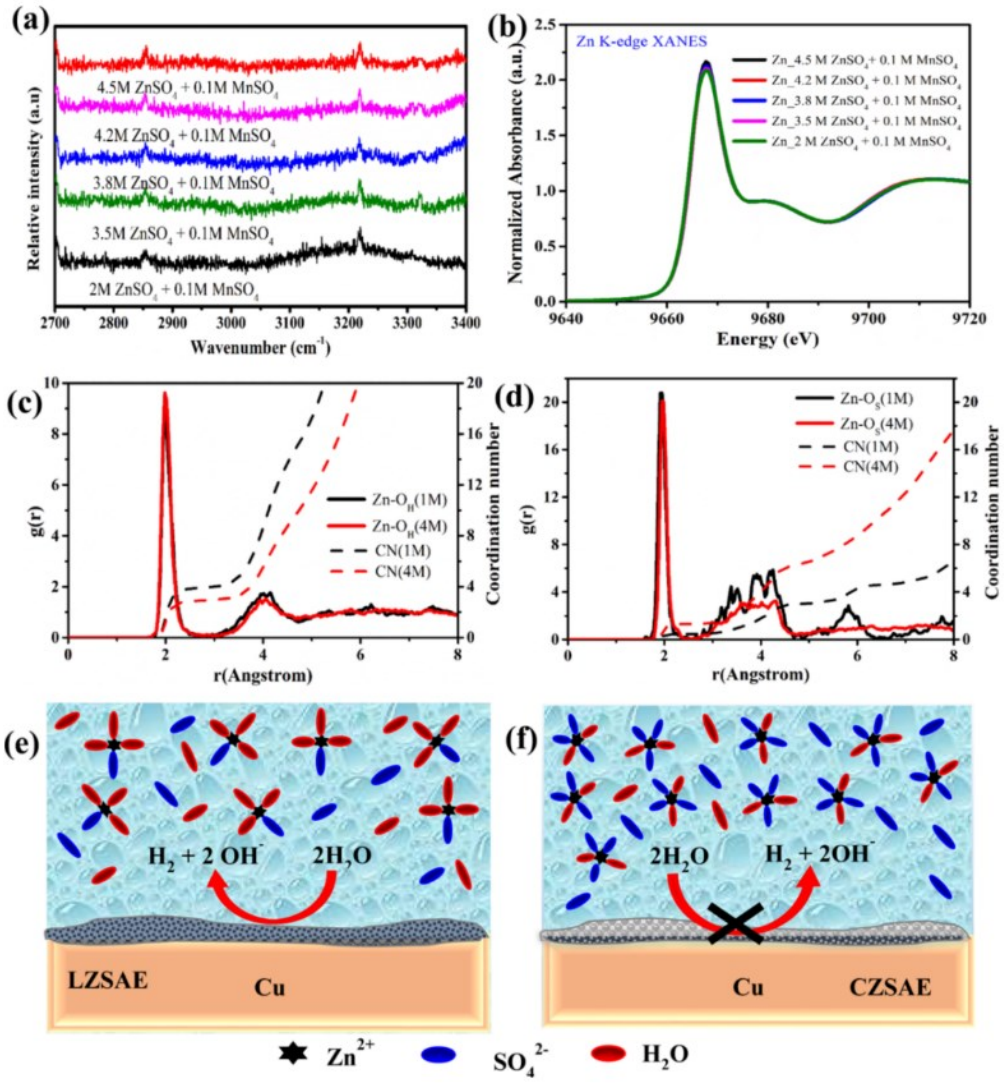

Figure 1. (a) Raman spectra for various concentrations of electrolyte with $ZnSO_4$ and $MnSO_4$. (b) The X-ray absorption near-edge spectra for various concentrations of electrolyte with $ZnSO_4$ and $MnSO_4$. (c) Radial distribution function and coordination numbers of Zn-O_H_2O with different concentrations of electrolyte. (d) Radial distribution function and coordination numbers of Zn-O_SO_4^{2-} with different concentrations of electrolyte. (e),(f) Schematic of Zn^{2+} deposition on copper. Copyright 2020, American Chemical Society

$Zn(TFSI)_2$ salt is also a popular choice due to its high electrochemical stability and ionic conductivity. Wang et al. (23) reported a highly concentrated electrolyte of 1m $Zn(TFSI)_2$ + 20m LiTFSI (m is mol/kg). As shown in Fig. 2a, molecular dynamic (MD) simulation is performed to

analyze the solvation structure in the electrolyte. For the 1m $Zn(TFSI)_2$ + 5m LiTFSI electrolyte, the Zn^{2+} fully interacts with six water molecules, and the solvation structure of $[Zn(H_2O)_6]^{2+}$ is displayed (Fig. 2b). For the 1m $Zn(TFSI)_2$ + 10m LiTFSI electrolyte, the Zn^{2+} bonds with only two water molecule and the rest of four water molecules are replaced by TFSI anions. For the 1m $Zn(TFSI)_2$ + 20m LiTFSI electrolyte, all six water molecules are replaced by TFSI anions, and there are no water molecules in the solvation structure anymore. Then the coordination numbers of Zn^{2+} interacting with water molecules and salt anions are calculated. In Fig. 2c, the coordination number of the Zn-O_TSFI pair is zero for the 1m $Zn(TFSI)_2$ + 5m LiTFSI electrolyte. As the concentration of LiTFSI increases, the coordination number increases. When the concentration of LiTFSI increases to 20m, the coordination number increases to six, which represents the occupation of six TFSI anions in the solvation structure. In comparison, the coordination number of the Zn-O_H_2O pair is six in 5m LiTFSI (Fig. 2d). As the concentration of LiTFSI increases, fewer and fewer water molecules display in the solvation structure. In Fig. 2e, ^{17}O NMR spectra present a peak shift toward lower frequency as the concentration of LiTFSI salt increases. This result indicates that water molecules are restricted in the Zn^{2+} solvation structure, which is possibly due to the Li^+ solvation structure. The full cell of the Zn anode coupled with $LiMn_2O_4$ cathode is investigated in Fig. 2f. The cell shows excellent stability for 4000 cycles at a 4C rate with capacity retention of 85% and a high CE of 99.9%.

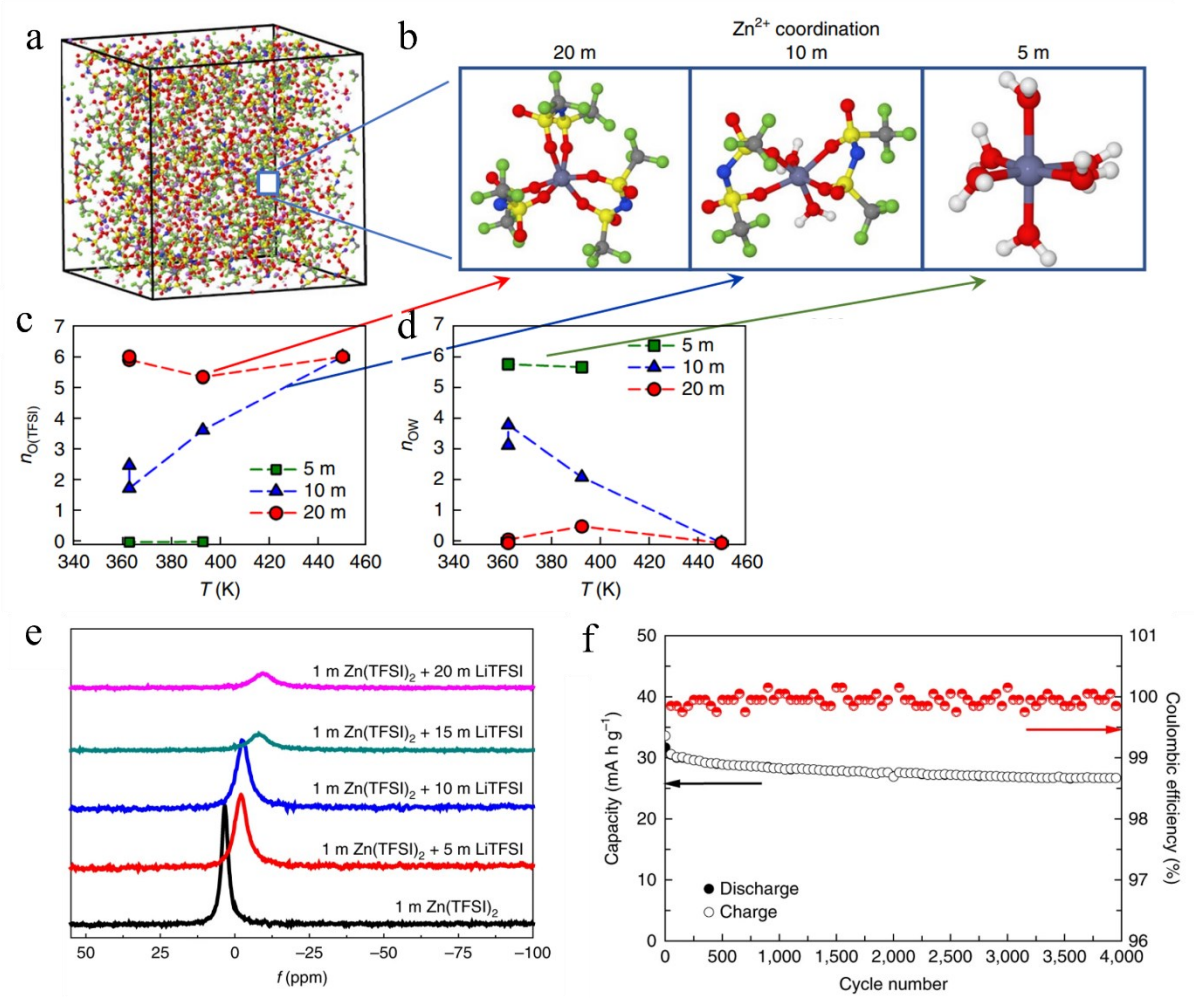

Figure 2. (a) Molecular dynamic (MD) simulation cell of electrolyte (1m $Zn(TFSI)_2$ + 20m LiTFSI). (b) Zn^{2+} solvation structure in 1m $Zn(TFSI)_2$ + 5m/10m/20m LiTFSI electrolytes. (c) The coordination number of Zn-O_TSFI pair in 1m $Zn(TFSI)_2$ + 5m/10m/20m LiTFSI electrolytes. (d) The coordination number of Zn-O_H_2O pair in 1m $Zn(TFSI)_2$ + 5m/10m/20m LiTFSI electrolytes. (e) ^{17}O (nuclear magnetic resonance) NMR spectra of electrolytes with different salt concentrations. (f) Long cycling performance of Zn//$LiMn_2O_4$ full cell at 4C rate. Copyright 2018, Nature

$ZnCl_2$ is a commonly used Zn-salt for highly concentrated electrolytes due to its excellent solubility. Every 100 mL of water can dissolve 432g of $ZnCl_2$ at room temperature. Zhang et al. (24) introduced a highly concentrated electrolyte of 30m $ZnCl_2$. In Fig. 3a, the Zn//Zn symmetric cell is assembled, and a long cycling performance with stable charge and discharge potential is

achieved at 0.2mA cm^{-2} for the 30m $ZnCl_2$ electrolyte. For the 5m $ZnCl_2$ electrolyte, the potential varies after 380 cycles, and the cell eventually short-circuited at 500 cycles, which results in an unstable cycling performance. Then the morphology of cycled Zn electrode is discovered from the SEM image. In Fig. 3b, the SEM image shows a large number of flakes on the surface of cycled electrode for the 5m $ZnCl_2$ electrolyte. In comparison, the SEM image shows a much more uniform and smoother Zn surface for the 30m $ZnCl_2$ electrolyte (Fig. 3c). The XRD also shows the same outcomes from SEM. In Fig. 3d, by-products of $Zn(OH)_2$ and ZnO are shown on the cycled Zn electrode in the 5m $ZnCl_2$ electrolyte, while there are no by-products on the Zn electrode in the 30m $ZnCl_2$ electrolyte. This result also indicates the suppression of hydrogen evolution reaction on the Zn surface. A poor CE of 73.2% is obtained for the 5m $ZnCl_2$ electrolyte (Fig. 3e) compared to a high CE of 95.4% for the 30m $ZnCl_2$ electrolyte (Fig.3f).

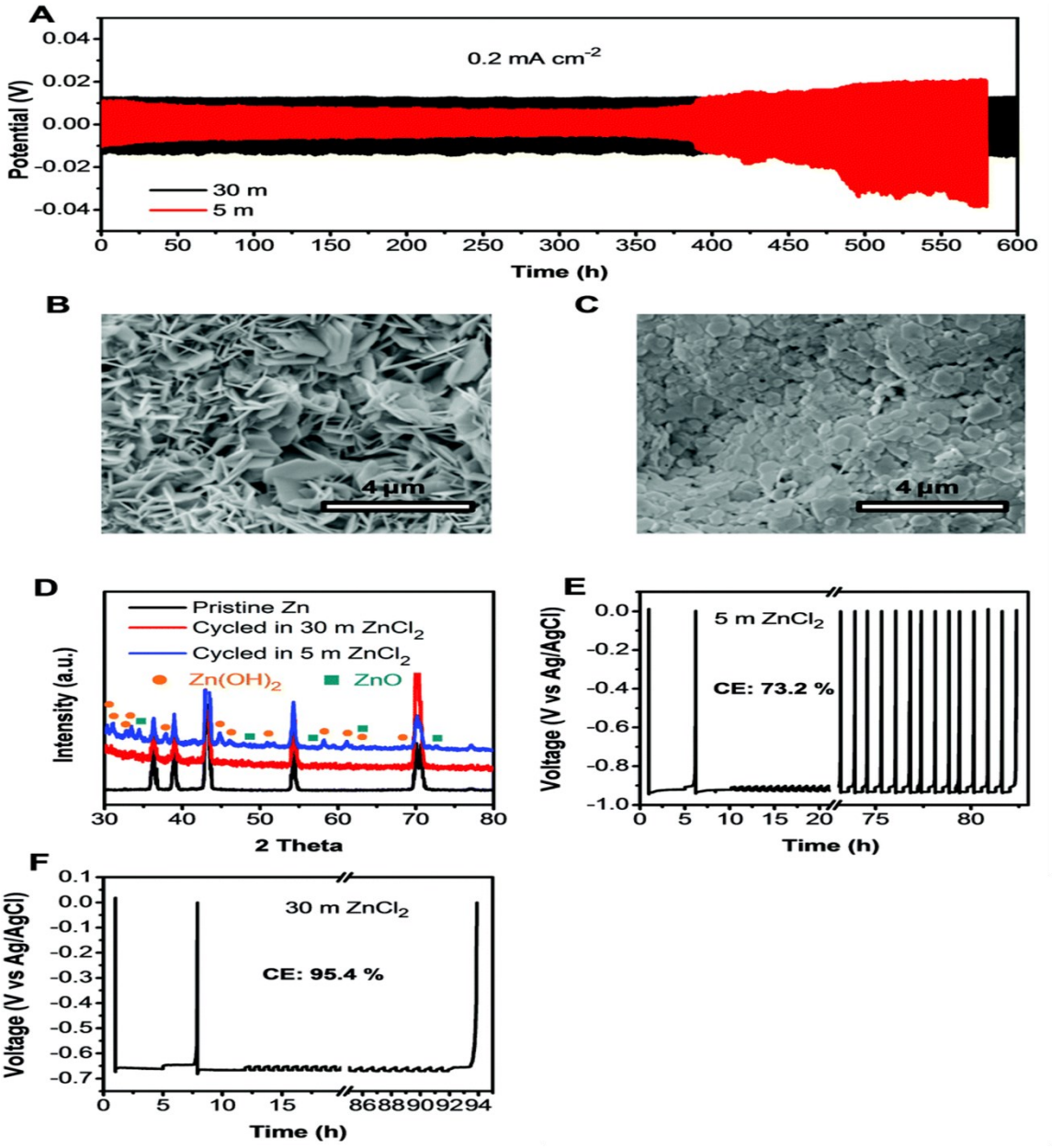

Figure 3. (a) Zn//Zn symmetric cell with 30m $ZnCl_2$/5m $ZnCl_2$ electrolyte at 0.2mA cm^{-2}. (b) SEM image of cycled Zn electrode in 5m $ZnCl_2$ electrolyte. (c) SEM image of cycled Zn electrode in 30m $ZnCl_2$ electrolyte. (d). XRD of cycled Zn electrode in 30m $ZnCl_2$/5M $ZnCl_2$ electrolyte. (e) CE of asymmetric cell with 5m $ZnCl_2$ electrolyte. (f) CE of asymmetric cell with 30m $ZnCl_2$ electrolyte. Copyright 2018, Royal society of chemistry

$Zn(CF_3SO_3)_2$ ($Zn(OTF)_2$) is another example of Zn-salt used in Zinc-ion batteries. Clarisza et al.

(25) demonstrated a highly concentrated electrolyte of 1m $Zn(OTF)_2$ + 20m LiTFSI. When the concentration of LiTFSI increases, the Linear sweep voltammetry (LSV) shows a wider electrochemical potential window of 2.856V compared to the water decomposition potential window of 1.23V (Fig. 4a). This result shows that the hydrogen evolution reaction is suppressed. The wider electrochemical potential window results in better stability of electrolytes in the battery system. Raman spectroscopy is performed to analyze the water molecules in the electrolyte. As the electrolyte concentration increases, the intensity of $Zn(OTF)_2$ peak at 1033 cm^{-1} is not affected (Fig. 4b). By considering the intensity ratio of LiTFSI and water molecules, since the intensity of LiTFSI increases significantly, the intensity of water molecules decreases in the 20m LiTFSI highly concentrated electrolyte. The decreased water molecules indicate the suppression of hydrogen evolution reaction and the reconstruction of solvation structure. In Fig. 4c, the coordination number of Zn-O_H_2O, the pair is six in the low-concentrated electrolyte, which shows a $[Zn(H_2O)_6]^{2+}$ solvation structure. In comparison, the coordination number of the Zn-O_H_2O pair is one (Fig. 4d) and the coordination number of the Zn-O_TFSI pair is five (Fig. 4e) in the highly concentrated electrolyte. This concludes a solvation structure of Zn^{2+} interacts with one water molecule and five TFSI anions. Furthermore, in the low-concentrated electrolyte, the Zn plating on the Cu surface is sharp and rough with plenty of flakes (Fig. 4f). The Cu surface after Zn stripping has lots of residue remaining (Fig. 4g). On the other hand, a smoother Cu surface is obtained after Zn plating (Fig. 4h) and a more uniform and cleaner Cu surface is obtained after Zn stripping (Fig. 4i) in the highly concentrated electrolyte.

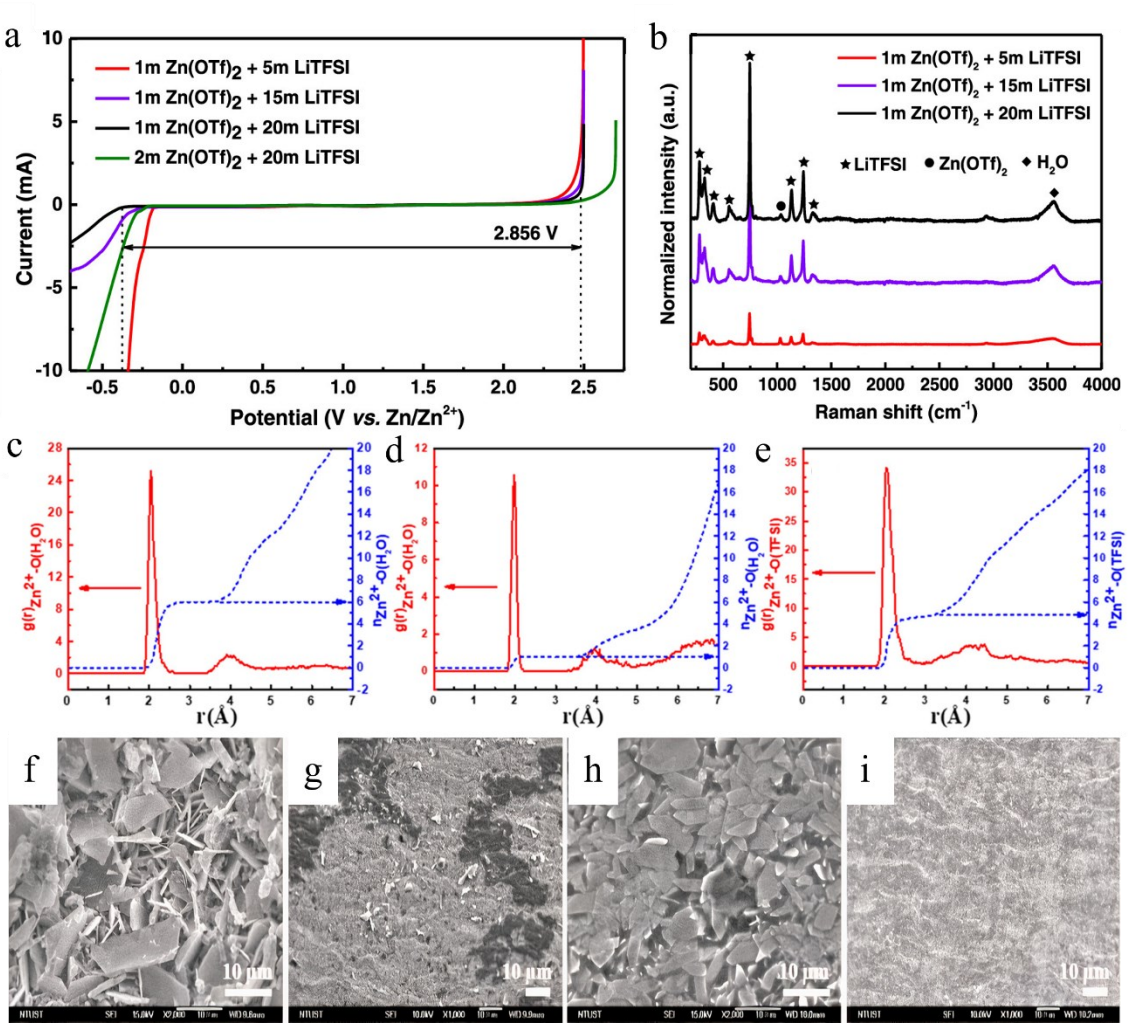

Figure 4. (a) Linear sweep voltammetry of Zn symmetric cell for different concentrations of electrolytes. (b) Raman spectroscopy of different concentrations of electrolytes. (c) The coordination number of Zn-O_H_2O pair in low concentrated electrolytes. (d) The coordination number of Zn-O_H_2O pair in highly concentrated electrolytes. (e) The coordination number of Zn-O_TFSI pair in the highly concentrated electrolytes. (f) SEM image of Zn plating in the low-concentrated electrolyte. (g) SEM image of Zn stripping in the low-concentrated electrolyte. (h) SEM image of Zn plating in the highly concentrated electrolyte. (i) SEM image of Zn stripping in the highly concentrated electrolyte. Copyright 2022, American Chemical Society

1.5.2 Organic solvent

All the examples from 1.3.1 conclude the advantage of highly concentrated electrolytes. However, the viscosity of highly concentrated electrolyte might be high and leads to relatively low ionic conductivity. The cost of large amounts of salts used in the electrolyte is also a nonnegligible factor. Therefore, a relatively low-cost organic solvent is a better choice for manipulating Zn^{2+} solvation structure, including dimethyl sulfoxide (DMSO), dimethyl carbonate (DMC), glycerol, 1,2-dimethoxyethane (DME), ethylene glycol (EG)(26, 27), TEP(28) and many more.

The Gutmann donor number (DN) is a parameter that reflects the inherent electron-donating capacity. It can be utilized to assess the solubility of intermediate products and changes in the hydrogen-bonding network within aqueous electrolytes. In the context of organic solvent, a high DN indicates a strong electron-donating capability, leading to the displacement of water molecules within the solvation structure. Moreover, water-miscible additives with strongly polar groups are advantageous as they tend to preferentially solvate Zn cations due to their high polarity. These organic solvents can disrupt the existing water clusters and act as proton acceptors, forming bonds with water molecules in the aqueous solution.

Cao et al. (29) introduced DMSO in the $ZnCl_2$ electrolyte, in which DMSO has a higher donor number (29.8) than H_2O (18). In Fig. 5a, X-ray absorption near-edge structure (XANES) is performed to show the bonding strength of Zn^{2+}-O. By introducing the DMSO into the electrolyte, the edge position shifts to a lower energy level. This shows that the bonding between Zn^{2+} and oxygen from water molecules is weakened due to restricted electron transfer. Fourier transformed extended X-ray absorption fine structure (ft-EXAFS) is further tested for analyzing solvation structure (Fig. 5b). Without the addition of DMSO, the distance between Zn^{2+} and O_H_2O decreases. This result indicates that the Zn^{2+}-O_H_2O bonding is stronger without DMSO, which leads to the formation of $[Zn(H_2O)_6]^{2+}$. Then the ^{67}Zn NMR spectra show an upshift toward higher frequency with the addition of DMSO in Fig. 5c. This shows that the DMSO molecule is capable to enter the Zn^{2+} solvation structure and replace the water molecules. Zn//Ti asymmetric cells are

assembled to test the CE. In Fig. 5d, without the addition of DMSO, a poor CE of 90.7% is obtained for less than 50 cycles. In comparison, with the addition of DMSO, the CE improve to 99.5% for 400 cycles. Stability is also tested by assembling Zn//Zn symmetric cells. In Fig. 5e, the cell shows excellent stability for 1000 hours with DMSO under conditions of 0.5 mA cm^{-2} and 0.5 mAh cm^{-2}. In contrast, the cell failed at 390 hours with bulk electrolyte.

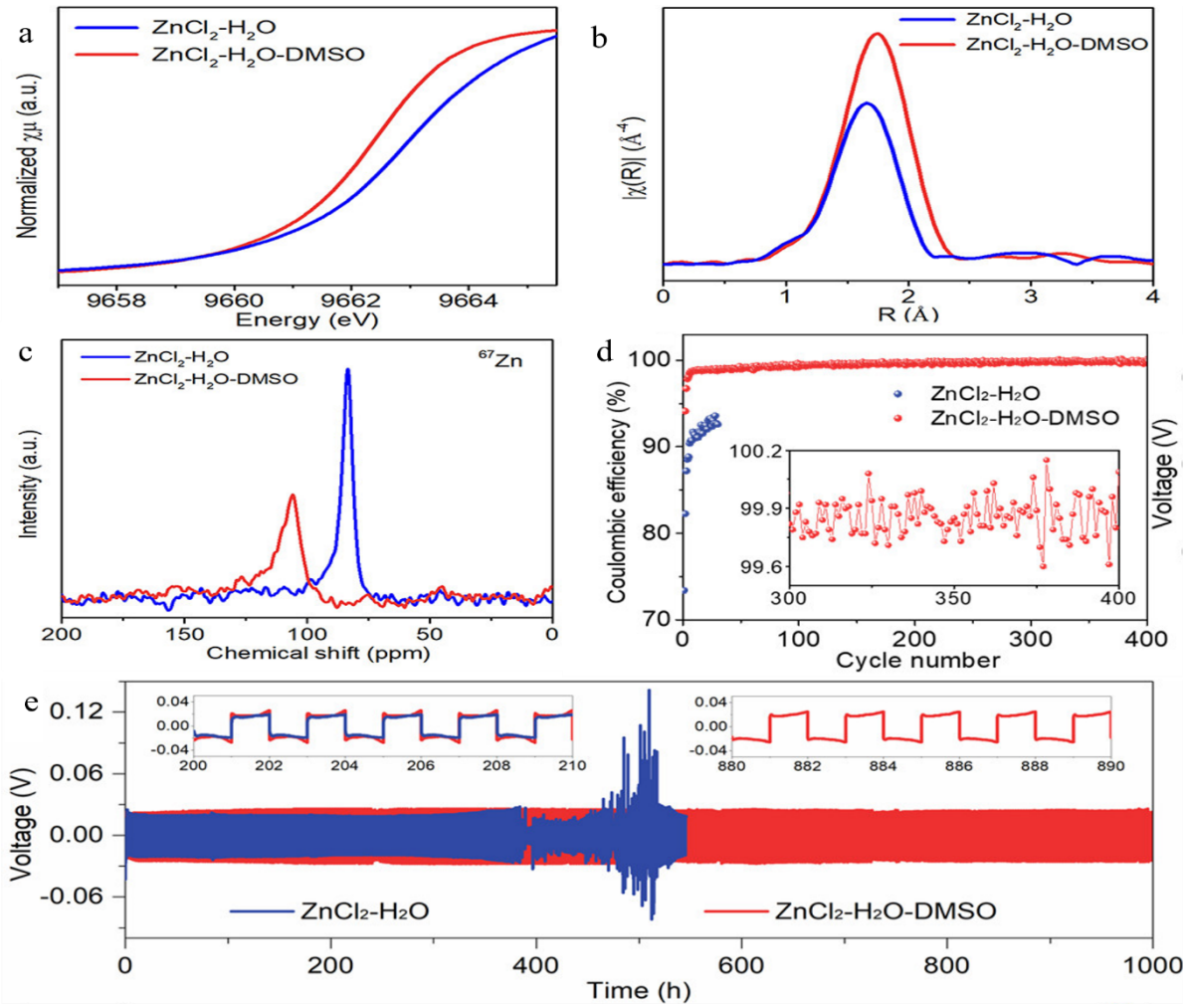

Figure 5. (a) X-ray absorption near-edge structure (XANES) for Zn^{2+}-O bonding. (b) Fourier transformed extended X-ray absorption fine structure (ft-EXAFS) for Zn^{2+}-O bonding. (c) ^{67}Zn (nuclear magnetic resonance) NMR spectra of electrolytes. (d) Coulombic efficiency of Zn//Ti asymmetric cell at 1 mA cm^{-2} and 0.5 mAh cm^{-2}. (e) Cycling performance of symmetric cells at 0.5 mA cm^{-2} and 0.5 mAh cm^{-2}. Copyright 2020, American Chemical Society

Dong et al. (30) reported a non-concentrated electrolyte of 2M $Zn(OTF)_2$ with DMC as the organic solvent. Solvation structure information is investigated by MD simulation in Fig. 6a. In the bulk $Zn(OTF)_2$ electrolyte, the Zn^{2+} is surrounded by only water molecules. In the electrolyte with water and DMC as a solvent in a volume ratio of 4:1 (W4D1), OTF^- anion and DMC molecule entered the solvation structure and replace the water molecule, due to the strong interaction with Zn^{2+}. The calculated coordination number of Zn^{2+}-O further agrees with the above results. In the W4D1 electrolyte, the coordination number of Zn-O_H_2O is 3.9, the coordination number of Zn-O_DMC is 0.7 and the coordination number of Zn-O_OTF^- is 1.4. This leads to a solvation structure of $Zn[H_2O]_{3.9}[OTF^-]_{0.7}[DMC]_{1.4}$. Furthermore, with the addition of DMC solvent, the fraction of water molecules in the electrolyte decreases to 100ns (Fig. 6c). More than 80% of water molecules remain in the bulk 2M $Zn(OTF)_2$ electrolyte while 65% of water molecule remain in the W2D1 electrolyte. The few water molecule in the electrolyte restricts the hydrogen evolution reaction significantly. ^{17}O NMR spectra show a downshift toward lower frequency, which indicates the decrease of water molecules in the solvation structure due to the breaking of H-O bonding (Fig. 6d). XRD of cycled Zn electrode shows the formation of by-product in bulk $Zn(OTF)_2$ electrolyte, which related to the decomposition of water molecules on the Zn surface (Fig. 6e). Excellent stability is obtained from Zn//Zn symmetric cell that runs at 5mA cm^{-2} for 800 hours with steady charge and discharge potential.

Zhang et al. (31) illustrated an electrolyte of 2M $ZnSO_4$ dissolved in water and glycerol solvent in a volume ratio of 1:1. Linear polarization curve is performed to analyze the corrosion of Zn metal in the electrolyte (Fig. 7a). With the addition of glycerol, the corrosion current decreases from 1.5mA to 0.14mA. This indicates a lower corrosion rate and restricted hydrogen evolution reaction in the electrolytes. The image of Zn foils soaked in the bulk $ZnSO_4$ electrolyte shows a color change, which proves the formation of by-products on the Zn surface (Fig. 7b). XRD further concludes the formation of $ZnSO_4(Zn(OH)_2)_3(H_2O)5$ by-product on the Zn surface in the bulk $ZnSO_4$ electrolyte (Fig. 7c). These results show that glycerol has the capability of protecting the Zn surface from reactions happened on the Zn surface. In Fig. 7d, DFT calculation shows that the

binding energy of Zn^{2+}-SO_4^{2-} (55.34eV) and Zn^{2+}-glycerol (5.578eV) are larger than Zn^{2+}-H_2O (0eV). This indicates that Zn^{2+} is more favorable to interact with glycerol molecules and SO_4^{2-} anions. Chronoamperograms (CA) show a stable 2D diffusion with the addition of glycerol (Fig. 7e). This indicates a smooth and uniform Zn deposition on the Zn surface. Better CE is obtained in glycerol electrolyte and the 1:1 ratio of glycerol/water electrolyte has the best CE of 99.5% for 500 cycles (Fig. 7f). In Fig. 7g, Zn//Zn symmetric cell shows excellent stability for 900 hours at 2mA cm^{-2} and 6mAh cm^{-2} with the addition of glycerol. Without glycerol, the cell fails at 80 hours with poor stability.

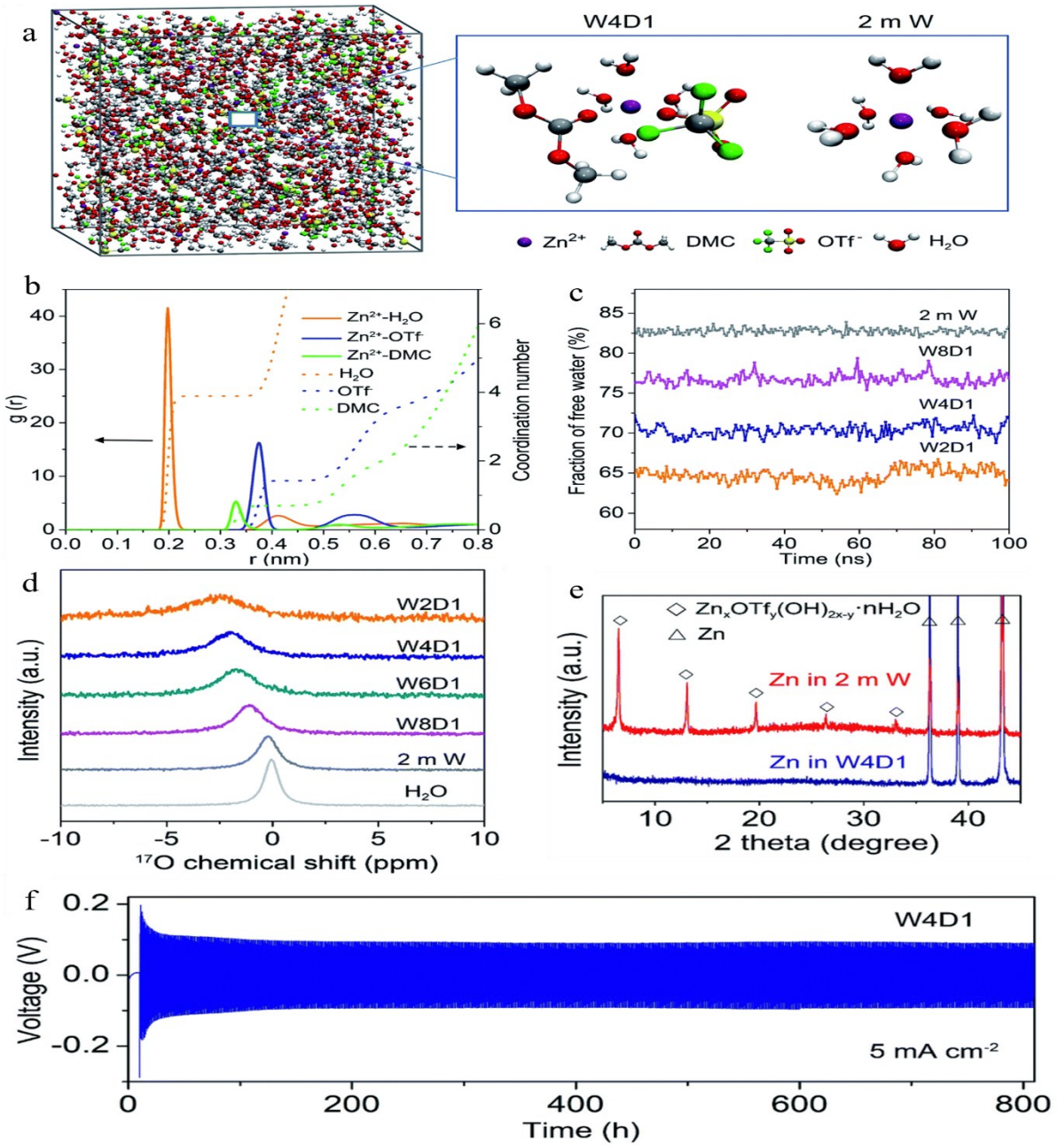

Figure 6. (a) MD simulation cell for $Zn(OTF)_2$ electrolyte with water solvent and water-DMC solvent in a volume ratio of 4:1 (W4D1). (b) Radial distribution function and coordination numbers of Zn-O_H_2O, Zn-O_DMC, and Zn-O_OTF^-. (c) Fraction of free water molecules in the electrolyte after simulation. (d) ^{17}O NMR spectra of electrolytes with different volume ratios of DMC and H_2O. (e) XRD of cycled Zn electrode. (f) Zn//Zn symmetric cell cycling performance at 5mA cm^{-2}. Copyright 2021, Royal Society Of Chemistry

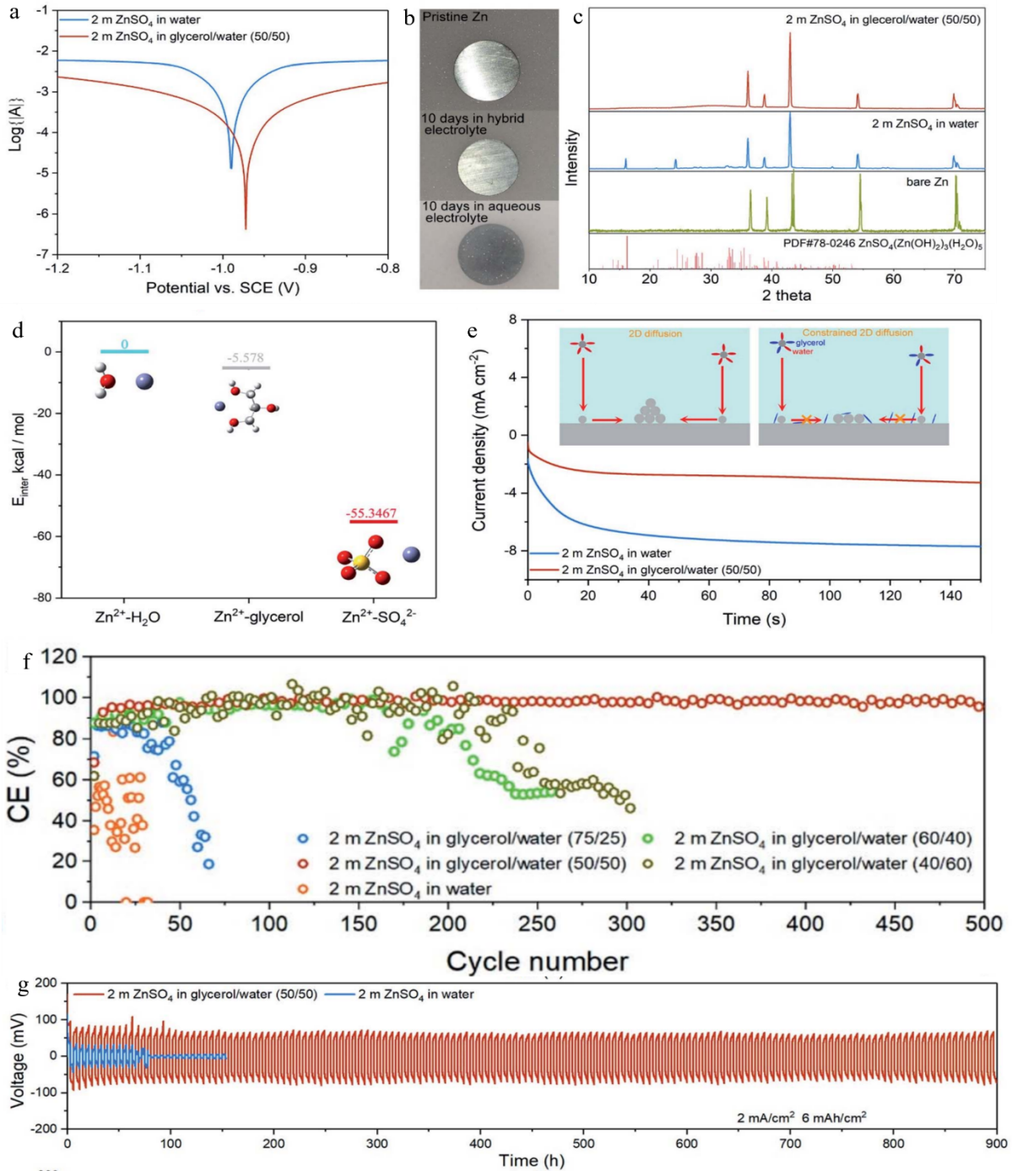

Figure 7. (a) Linear polarization curve of electrolyte with and without glycerol. (b) Zn foils soaked in electrolytes with and without glycerol. (c) XRD of Zn foils soaked in electrolytes. (d) Binding energy of Zn^{2+}-H_2O, Zn^{2+}-glycerol and Zn^{2+}-SO_4^{2-}. (e) Chronoamperograms (CA) of Zn^{2+} diffusion. (f) CE of different volume ratios of electrolytes. (g) Zn//Zn symmetric cell cycling

performance. Copyright 2021, Royal Society Of Chemistry

Ma et al. (32) demonstrated a $Zn(OTF)_2$ electrolyte with DME as an organic solvent. The solvation structure is simulated as shown in Fig. 8(a-c). With the addition of DME, one water molecule is replaced by an OTF^- anion, which leads to the reconstruction of the Zn^{2+} solvation structure. The coordination number of Zn-O_H_2O is 4.32, Zn-O_OTF^- is 1.38 and Zn-O_DME is 0.23 (Fig. 8d). This result further proves the participation of DME and OTF^- in the solvation sheath. The binding energy of Zn^{2+}-DME is much larger than DME-H_2O and Zn^{2+}-H_2O, which indicates better interaction between Zn^{2+} and DME molecules. The lowest unoccupied molecular orbital (LUMO) level shows that the Zn^{2+}-DME and Zn^{2+}-OTF^- have lower LUMO energy in Fig. 8f. This result indicates that DME molecule and OTF^- anion are much easier to accept electron and interphase layer is formed due to DME and OTF^- reduction. Absorption energy of DME on Zn (0 0 2) is higher than H_2O, which indicates that DME prefers to adsorb on the Zn surface (Fig. 2g). The charge density model in Fig. 3h shows that the Zn^{2+} interacts with DME through O bonding. The linear polarization curve in Fig. 8i shows a lower corrosion current with the addition of DME, which results in a suppression of side reaction on the Zn surface. Chronoamperograms (CA) curve shows a more stable 3D diffusion of Zn^{2+} with the addition of DME (Fig. 8j). The cycled Zn electrode in Fig. 8k shows the formation of Zn dendrite in bulk electrolyte while a smooth and uniform Zn deposition is obtained with DME in the electrolyte.

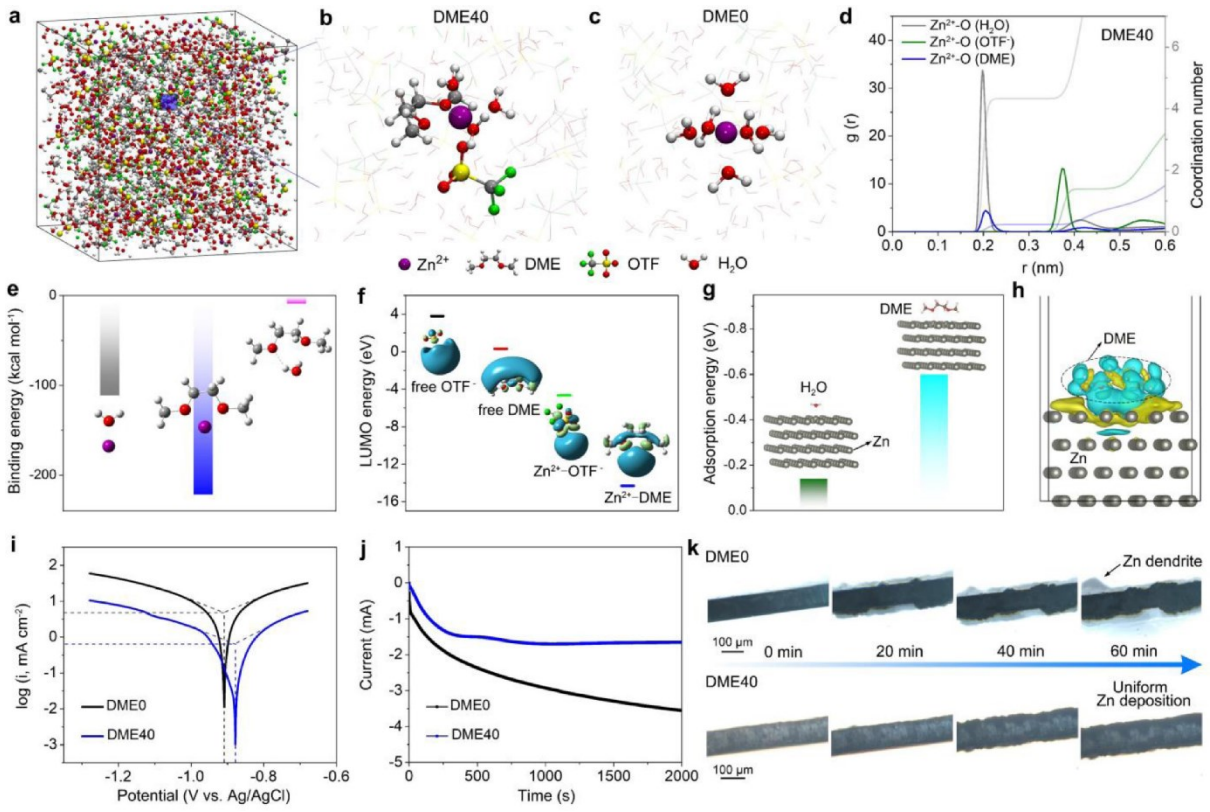

Figure 8. (a) Image of MD simulation cell in (b) DME electrolyte (c) bulk electrolyte. (d) Radial distribution function and coordination number of Zn-O_H_2O, Zn-O_OTF^- and Zn-O_DME. (e) Binding energy of Zn^{2+}-H_2O, Zn^{2+}-DME and Zn^{2+}-OTF^-. (f) LUMO level of free OTF^-, DME, Zn^{2+}-OTF^- and Zn^{2+}-DME. (g) Absorption energy of H_2O and DME on Zn (0 0 2) surface. (h) Charge density on Zn (0 0 2) surface. (i) Linear polarization curve of electrolyte with and without DME. (j) Chronoamperograms (CA) of Zn^{2+} diffusion. (k) Image of Zn electrode after platting. Copyright 2022, Elsevier

1.5.3 Additive

1.5.3.1 Metal ion additive

The low-cost and simple prepared metal ions additives (Na^{+}, Mg^{2+} (33), Mn^{2+}, Al^{3+}, Ni^{2+}, Co^{2+}, Pb^{2+}, etc.) have been considered promising additives due to their excellent performance on both anode and cathode(34-36). Metal ion additives can increase the ion conductivity in the electrolyte for fast ion transport kinetics. They can suppress the formation of Zn dendrite and side reaction on the anode. They can also protect the cathode from dissolution and intercalate in the cathode to improve capacity. Chang et al. (37) reported the function of Pb^{2+} ion and Ni^{2+} ion in protecting the Zn anode from dendrite growth. Pb^{2+} ions have a reduction potential of -0.359V at 298K and Ni^{2+} ions have a reduction potential of -0.257V at 298K. Zn^{2+} has a more negative reduction potential of -0.76V compared to Pb^{2+} and Ni^{2+} ions, which shows that Pb^{2+} and Ni^{2+} ions will be reduced first before Zn deposition. Therefore, the reductive Pb and Ni metal on the Zn surface provides nucleation sites for co-deposition with Zn^{2+}. The elemental mapping images of deposited Zn in bulk, $PbSO_4$, and $NiSO_4$ electrolytes are shown in Fig. 9a-c. Sharp and vertical Zn dendrites form on the Zn surface in the bulk electrolyte. With the addition of $PbSO_4$, the Zn dendrite is significantly reduced and both Zn and Pb are uniformly contributed, which indicates the co-deposition of Pb-Zn alloy on the surface. With the addition of $NiSO_4$, a relatively uniform Zn surface with little protrusion is obtained. This also indicates the co-deposition of Zn-Ni. The X-ray images of Zn plating in 400s further show the suppression of Zn dendrite in $PbSO_4$ and $NiSO_4$ electrolytes (Fig. 9d-f).

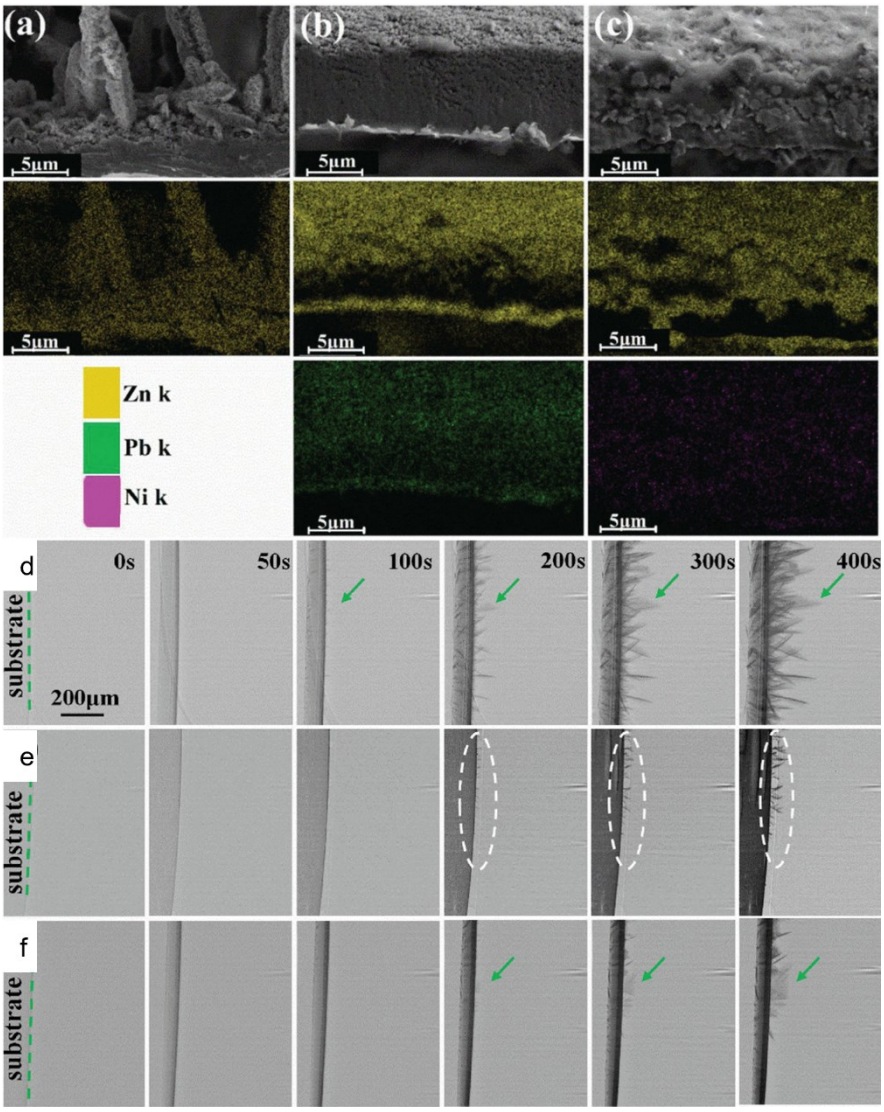

Figure 9. Elemental mapping images of Zn^{2+} deposition in (a) bulk electrolyte, (b) $PbSO_4$ electrolyte, and (c) $NiSO_4$ electrolyte. X-ray image of Zn^{2+} deposition in (d) bulk electrolyte, (e) $PbSO_4$ electrolyte, and (f) $NiSO_4$ electrolyte. Copyright 2019, Wiley

Unlike Pb^{2+} and Ni^{2+} ions which have larger reduction potential, Xu et al. (38) introduced Na_2SO_4 additive with low reduction potential of Na^+ in $ZnSO_4$ electrolyte. During the Zn deposition process, the Zn protrusions on the surface exhibit a strong electric field on their tips and force more deposition of Zn^{2+} ions on the protrusions. By introducing Na_2SO_4 in the electrolyte, since the Na^+ ion has a more negative reduction potential of -2.710V than Zn^{2+}, Zn^{2+} ions will be reduced first and form protrusions on the surface. Then the Na^+ ions will deposit on

the Zn protrusions and aggregate as an electrostatic shield. These Na^+ ions repel Zn^{2+} and force them to deposit at a non-protrusion area during subsequent Zn deposition. Therefore, the formation of Zn dendrite is restricted on the surface (Fig. 10a-c). The SEM image in Fig. 10d-f also shows uneven Zn dendrite in bulk electrolyte and uniform Zn surface in Na_2SO_4 electrolyte. The symmetric cell at 0.2 mA cm^{-2} also shows excellent cycling stability for 300 h with a low overpotential of 48 mV in the additive electrolyte (Fig. 10g).

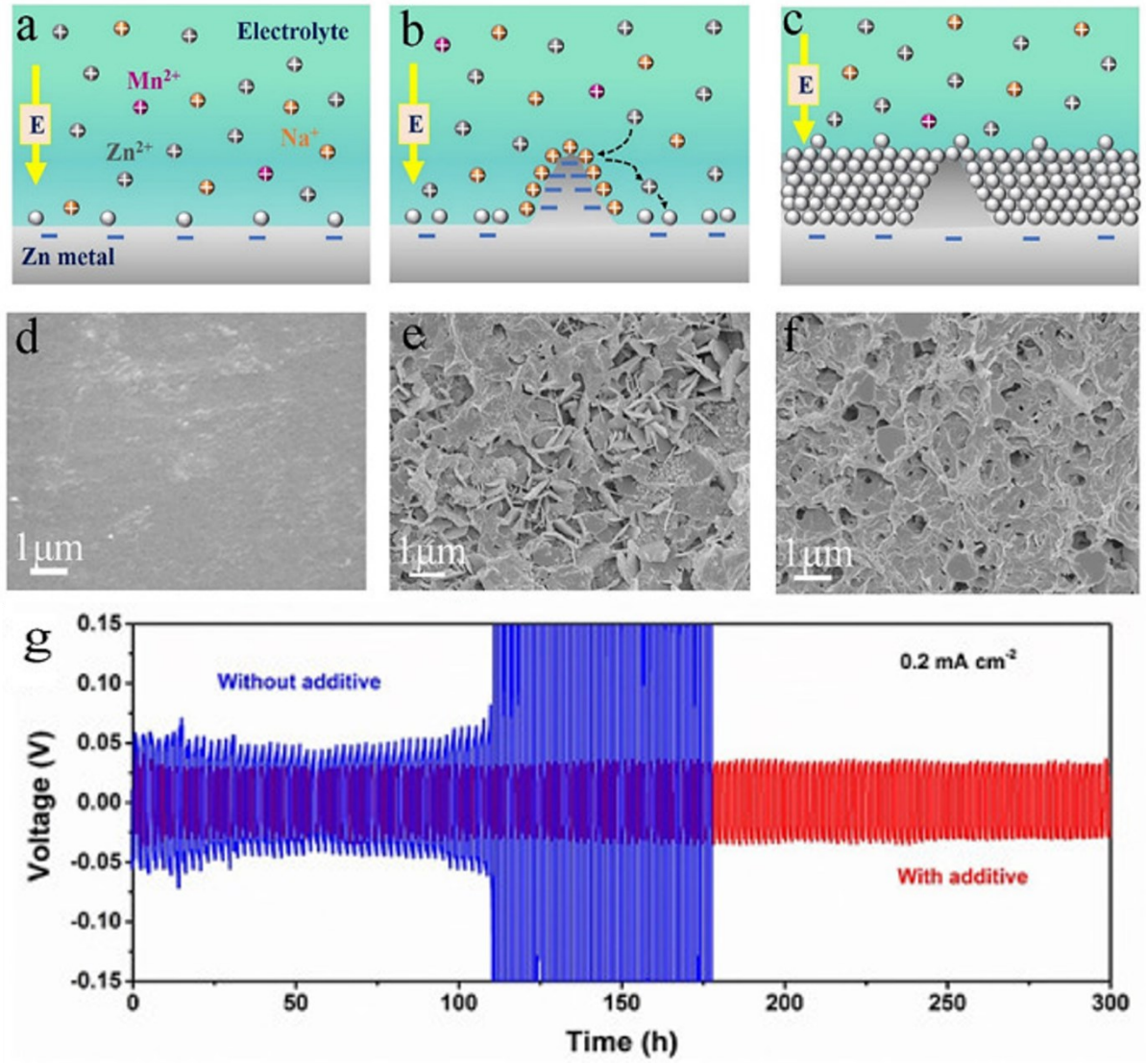

Figure 10. (a-c) Schematic of Na^+ helping uniform Zn^{2+} deposition. (d) SEM image of pure Zn surface. (e) SEM image of cycled Zn electrode without Na_2SO_4 additive. (f) SEM image of cycled Zn electrode with Na_2SO_4 additive. (g) Cycling performance of symmetric cell at 0.2mA cm^{-2} with

and without Na_2SO_4 additive. Copyright 2021, Elsevier

1.5.3.2 SEI layer additive

The SEI layer at the interface between the electrolyte and electrode acts as a protective film and protects the Zn surface from the Zn dendrite and side reaction. The properties and components of the SEI layer are highly relative to the salt and ions in the electrolyte. Therefore, by introducing either organic or inorganic additives, organic SEI layers such as CF_3 and CH and inorganic SEI layers such as ZnF_2 and $ZnCO_3$ might form on the surface. There are two types of SEI layers: in situ SEI layer and Artificial SEI layer. The in-situ SEI layer is formed due to the decomposition of solvent and additives in the electrolyte. The artificial SEI layer is protective 2D material that is absorbed on the anode surface. As discussed in 1.4, Ma et al. (32) introduced DME organic solvent in the electrolyte to modify the solvation structure. The DME can further form the SEI layer on the Zn surface. The XPS spectra of C 1s shows the formation of organic components (C-C, CF_3, and C-O) and inorganic component ($ZnCO_3$) due to the reduction of Zn^{2+}- DME components (Fig. 11a). The F 1s spectra show the formation of organic CF_3 and inorganic ZnF_2 caused by the reduction of OTF^- anion in the $Zn(OTF)_2$ salt. The S 2p spectra show organic SO_3 and inorganic ZnS and $ZnSO_3$ which comes from the reduction of OTF^- anion and DME. After 60s sputtering, the organic content reduces and the inorganic components of ZnF_2, $ZnCO_3$, and $ZnSO_3$ increase and remain. This result shows that the DME and OTF^- anion can perform inorganic $ZnCO_3$-ZnF_2-$ZnSO_3$ layer on the Zn surface, which protects the Zn surface from side reactions. SEM image of cycled Zn electrode further shows that the SEI layer promotes uniform Zn deposition and suppresses the formation of the dendrite (Fig. 11b-c). The symmetric cell also shows better cycling stability for 5000 h at 2 mA cm^{-2} in the DME40 electrolyte (Fig. 11d). A high CE of 99.7% for 800 cycles is obtained in the DME40 electrolyte (Fig. 11e).

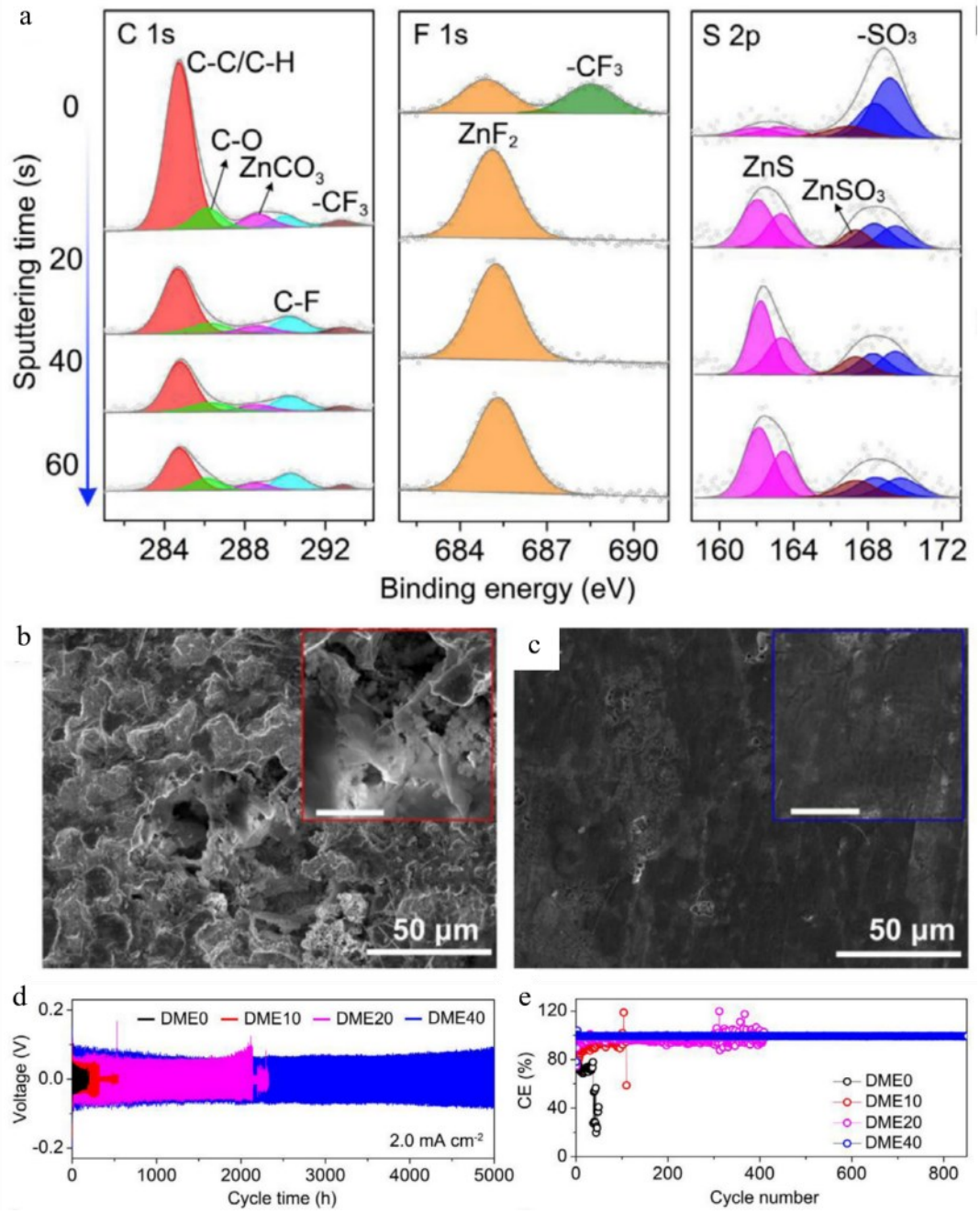

Figure 11. (a) XPS spectra of C 1s, F 1s, and S 2p. (b) SEM image of Zn electrode cycled for 100 cycles in the bulk electrolyte. (c) SEM image of Zn electrode cycled for 100 cycles in DME electrolyte. (d) Cycling performance of Zn symmetric cell at 2 mA cm^{-2}. (e) CE of asymmetric cells with different volumes of DME in the electrolyte. Copyright 2022, Elsevier

Similarly, Di et al (38) also found the formation of an organic-inorganic SEI layer in $Zn(OTF)_2$ electrolyte with triethyl phosphate (TEP) additive. The XPS spectra of C 1s show the organic component of C-C, C-O, CF_3, and C=O which are derived from the decomposition of TEP organic solvent (Fig. 12a). P 2p spectra shows organic RPO_3^- and inorganic $Zn_3(PO_4)_2$. The RPO_3^- comes from the reduction of TEP and the $Zn_3(PO_4)_2$ is derived from the reduction of the Zn^{2+}-PO_3^- complex. F 1s spectra show organic CF_3 and inorganic ZnF_2 which are caused by the reduction of OTF^- and Zn^{2+}. S 2p spectra show organic SO_3 and S-C and inorganic ZnS which also derived from the reduction of OTF^- and Zn^{2+}. The XPS spectra prove the formation of an organic-inorganic hybrid SEI layer on the surface. The Zn^{2+} will perform desolvation on the SEI film which water molecules are stopped outside the SEI layer and only Zn^{2+} continuous diffuse through the SEI layer. The XRD shows the formation of by-products on the Zn surface in the non-TEP electrolyte, and the SEM image further concludes the formation of a large number of flakes on the Zn surface (Fig. 12b). High and stable CE of 99.5% for 200 cycles is obtained with the addition of TEP while a low and fluctuant CE is achieved in the bulk electrolyte. Furthermore, the symmetric cell shows long and stable cycling performance at 1 mA cm^{-2} for 2500 hours in the TEP electrolyte and shows a short circuit at 300 hours in the bulk electrolyte.

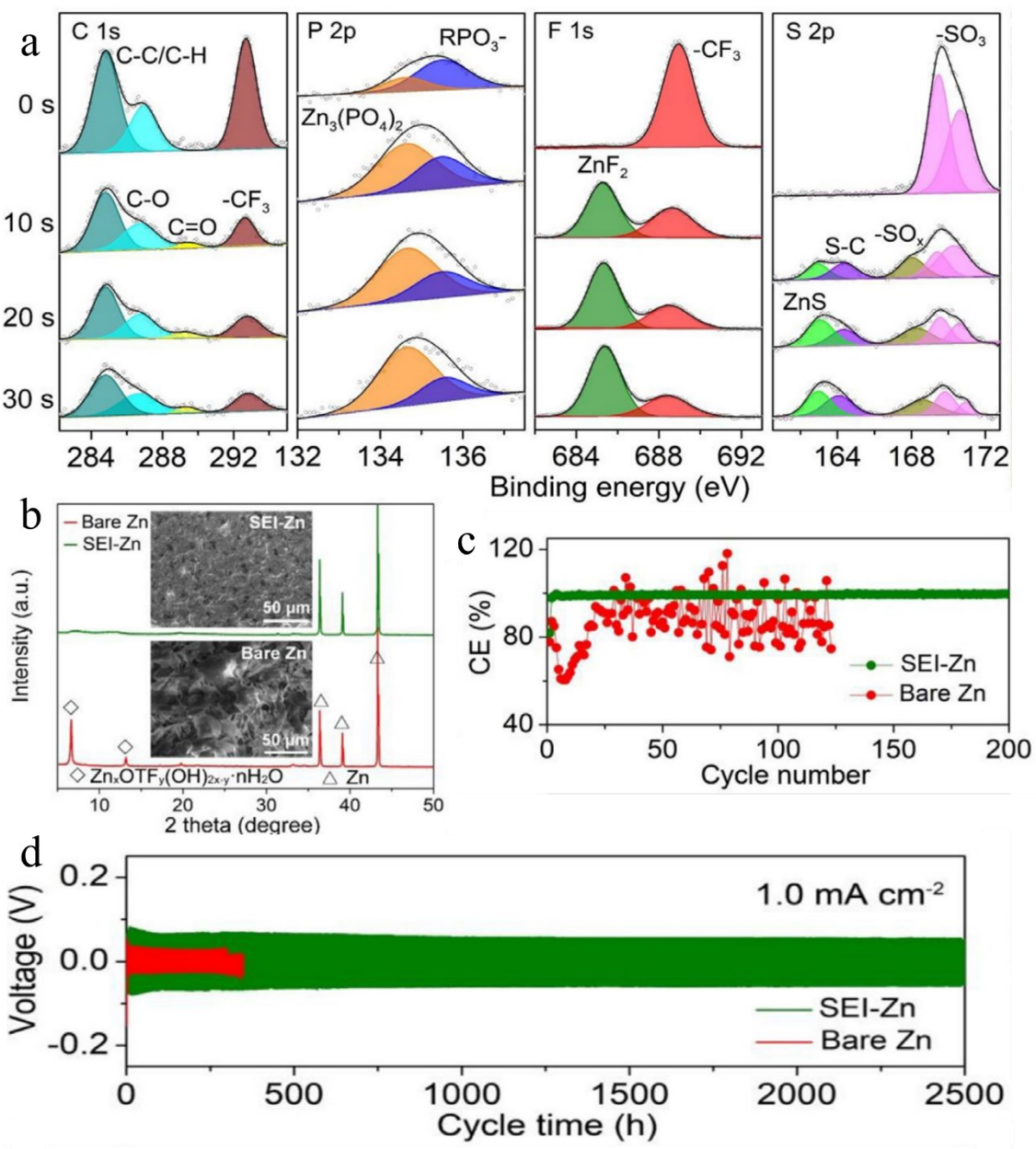

Figure 12. (a) XPS spectra of C 1s, P 2p, F 1s, and S 2p. (b) XRD and SEM of Zn foils soaked in TEP electrolyte and bulk electrolyte. (c) CE of asymmetric cell in TEP electrolyte and bulk electrolyte. (d) Cycling performance of Zn symmetric cell at 1 mA cm^{-2}. Copyright 2021, Elsevier

2D materials such as graphene oxide (GO) can be treated as protective SEI layer for smoother Zn^{2+} deposition. Abdulla et al. (39) introduced the use of GO as an electrolyte additive in a $ZnSO_4$ electrolyte. The SEM image shows that the Zn^{2+} deposition is uniform with the addition

of the GO additive (Fig. 13d-f). Without GO additive, the deposited Zn aggregate through 2D diffusion and form Zn dendrite (Fig. 13a-c). The mechanism of GO is shown in Fig. 13g. The GO molecules will deposit on the Zn surface with Zn^{2+} and absorb on the surface to provide more nucleation sites for Zn^{2+} deposition. Therefore, the Zn^{2+} will deposit on the GO molecules instead of the Zn protrusion, which leads to a uniform deposition. The asymmetric cell also shows a high CE of 99% for 100 cycles at 1mA cm^{-2} and 1mAh cm^{-2} in GO electrolyte.

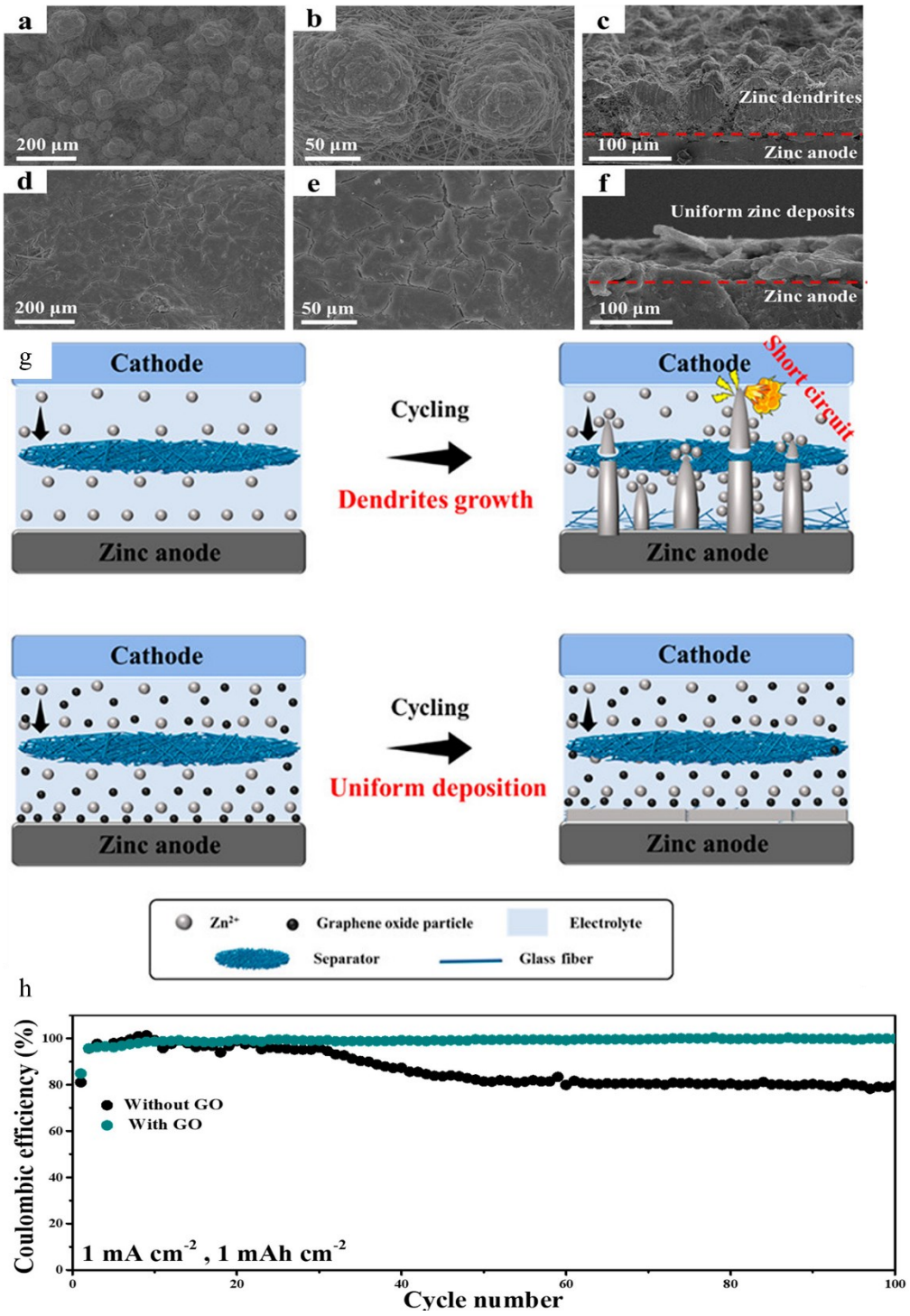

Figure 13. (a-c) SEM image of cycled Zn electrode without GO additive. (d-f) SEM image of cycled Zn electrode without GO additive. (g) Schematic of Zn^{2+} deposition with and without GO. (h) CE of the asymmetric cell at 1mA cm^{-2} and 1mAh cm^{-2} with and without GO. Copyright 2021, American Chemical Society

1.5.3.3 Surfactant additive

Surfactant has the properties of reducing the surface tension between the electrolyte and Zn surface. Therefore, surfactants can be absorbed on the Zn surface and isolate the direct contact between the Zn surface and water molecules. The surfactant congregates on the surface following the Zn deposition and these surfactant aggregates will protect the Zn surface from uneven dendrite growth. Hydrogen evolution reaction is also suppressed in this environment. There are four types of surfactants: cationic surfactant, anionic surfactant, amphoteric surfactant, and non-ionic surfactant. Cationic surfactants have a positive charge on their hydrophilic functional group, and they have been considered as a promising additive for protecting Zn surface, such as triethyl methylammonium (TMA) and tetrabutylammonium sulfate (TBA_2SO_4)(40). Bayaguud at el. (40) reported the use of TBA_2SO_4 surfactant additive in $ZnSO_4$ electrolyte for Zn surface protection. As shown in Fig. 14a, to minimize surface energy and exposed surface area during nucleation, Zn^{2+} ions adsorbed on the electrode surface tend to diffuse in a 2D direction and congregate into large nuclei. During subsequent electroplating, the continuous lateral diffusion and uneven distribution generated by these nuclei lead to more adsorption and reduction of Zn^{2+} ions at the previous nucleation sites. A large amount of Zn dendrites forms on the Zn surface. In Fig. 14b, when a moderate amount of TBA_2SO_4 is present in the electrolyte the TBA^+ cations are better adsorbed near the nucleus in the electroplating process, forming the TBA^+ cationic layer. Zn^{2+} is repelled by the absorbed TBA^+ aggregate and forced to deposit on the unabsorbed surface. SEM image in Fig. 14c-f clearly shows the morphology of the Zn deposited surface. Without the addition of TBA_2SO_4, multiple Zn aggregates lead to Zn dendrites on the surface. With the addition of TBA_2SO_4, a smooth and uniform surface is obtained.

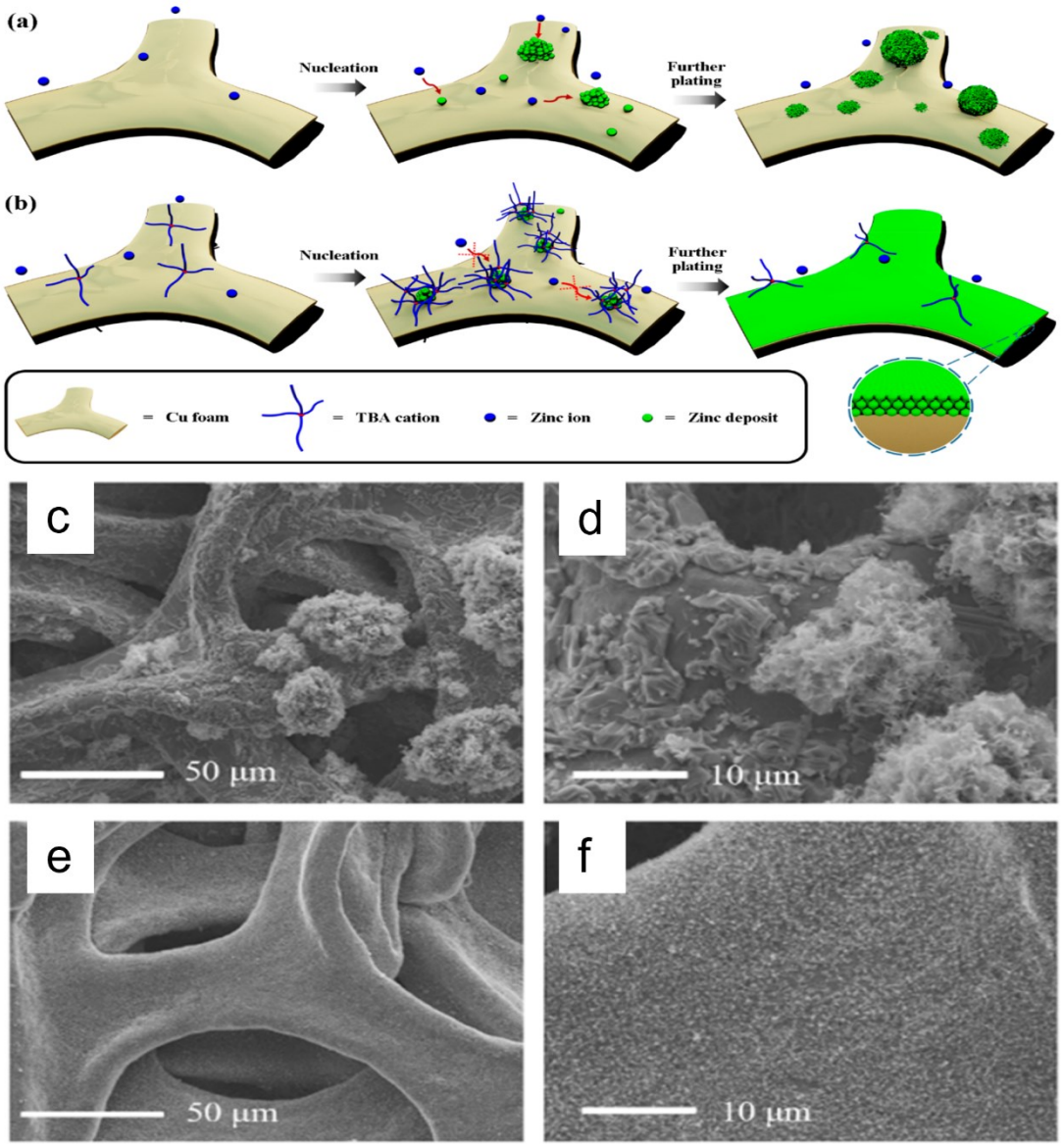

Figure 14. (a-b) Schematic of Zn^{2+} deposition without and with TBA_2SO_4. (c-d) SEM image of cycled Zn electrode in the bulk electrolyte. (e-f) SEM image of cycled Zn electrode in TBA_2SO_4 electrolyte. Copyright 2020, American Chemical Society

Similar to TBA_2SO_4, Yao et al. (41) discovered the function of TMA in the aspects of Zn anode protection. As shown in Fig. 15a-b, the TMA cation participated in the Zn solvation structure and replace the water molecules during diffusion. After Zn nucleation, TMA cations are further absorbed on the already formed Zn and aggregate as a protective layer to stop further Zn^{2+}

deposition on the same nucleation site. Hydrogen evolution reaction as well as by-product formation is restricted due to the absence of water molecules on the surface. Cycling performance also shows excellent stability at both high current density and low current density conditions (Fig. 15c-d).

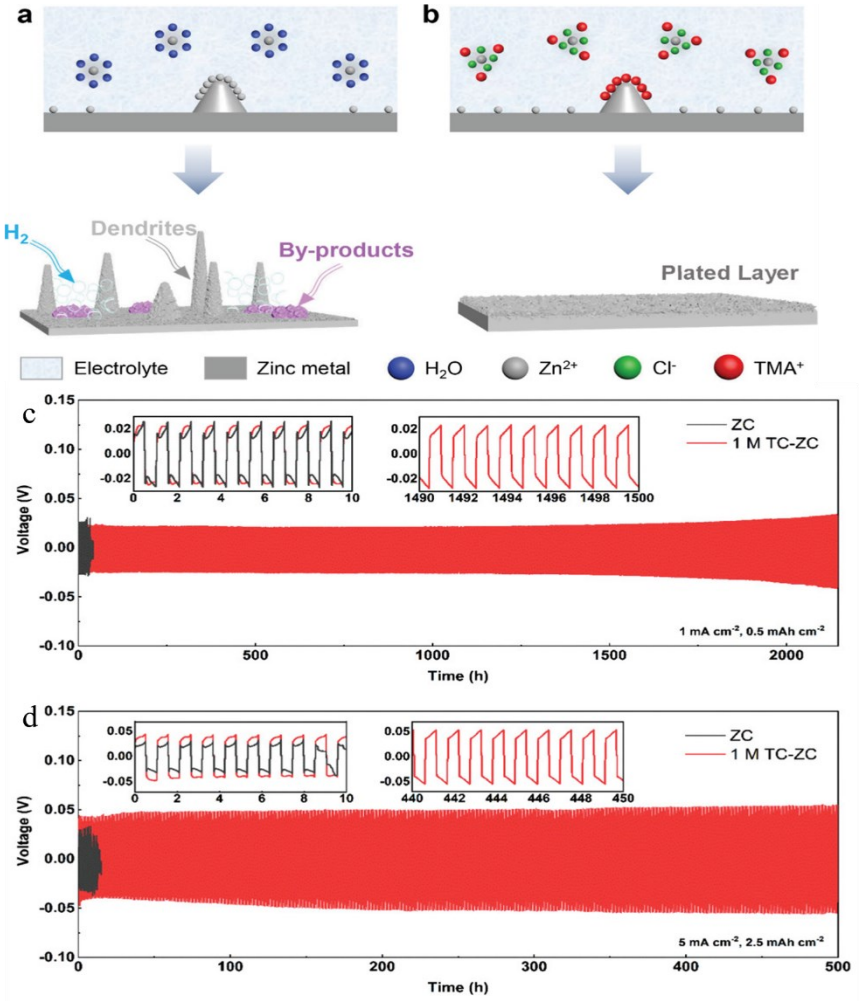

Figure 15. (a-b) Schematic of Zn^{2+} deposition without and with TMA. (c) Cycling performance of symmetric cell at 1 mA cm^{-2} and 0.5 mAh cm^{-2} with and without TMA. (d) Cycling performance of symmetric cell at 5 mA cm^{-2} and 2.5 mAh cm^{-2} with and without TMA. Copyright 2021, Wiley

Opposite to cationic surfactants, anionic surfactants have a negative charge on their hydrophilic functional group. Lin et al. (42) discovered sodium 3,3′-dithiodipropane sulfonate (SPS) as an anionic surfactant for better Zn deposition. As shown in Fig. 16a, Zn^{2+} is more likely to deposit on

Zn (1 0 1) plane in bulk electrolyte and the intensity of Zn^{2+} deposition on Zn (0 0 2) and Zn (1 0 0) are relatively weak. In comparison, Zn^{2+} prefers to deposit on Zn (0 0 2) plane in the SPS electrolyte, and the intensity of Zn^{2+} deposition on Zn (1 0 0) and Zn (1 0 1) are significantly reduced. By looking at the structure of Zn in Fig. 16b, Zn^{2+} deposition on the (0 0 2) plane is more favorable for uniform deposition. Furthermore, the absorption energy of the SPS anion on the (0 0 2) plane (6.43 eV) is smaller than the absorption energy on the (1 0 0) plane (7.35 eV) and (1 0 1) plane (7.16 eV) (Fig. 16c). Therefore, these results indicate the mechanism of promoting uniform Zn deposition for SPS. In the pure electrolyte, Zn^{2+} ions tend to adsorb on the (1 0 1) surface of the anode. This leads to the growth of larger protrusions and the formation of uneven Zn dendrites during further deposition. However, when SPS is introduced into the electrolyte, the deposition of Zn^{2+} ions on the (100) and (101) planes is restricted due to the higher amount of SPS adsorbed on these surfaces. As a result, Zn^{2+} ions have a higher tendency to deposit on the (002) plane. The deposited Zn leads to a horizontal and uniform growth pattern on the anode surface (Fig. 16d).

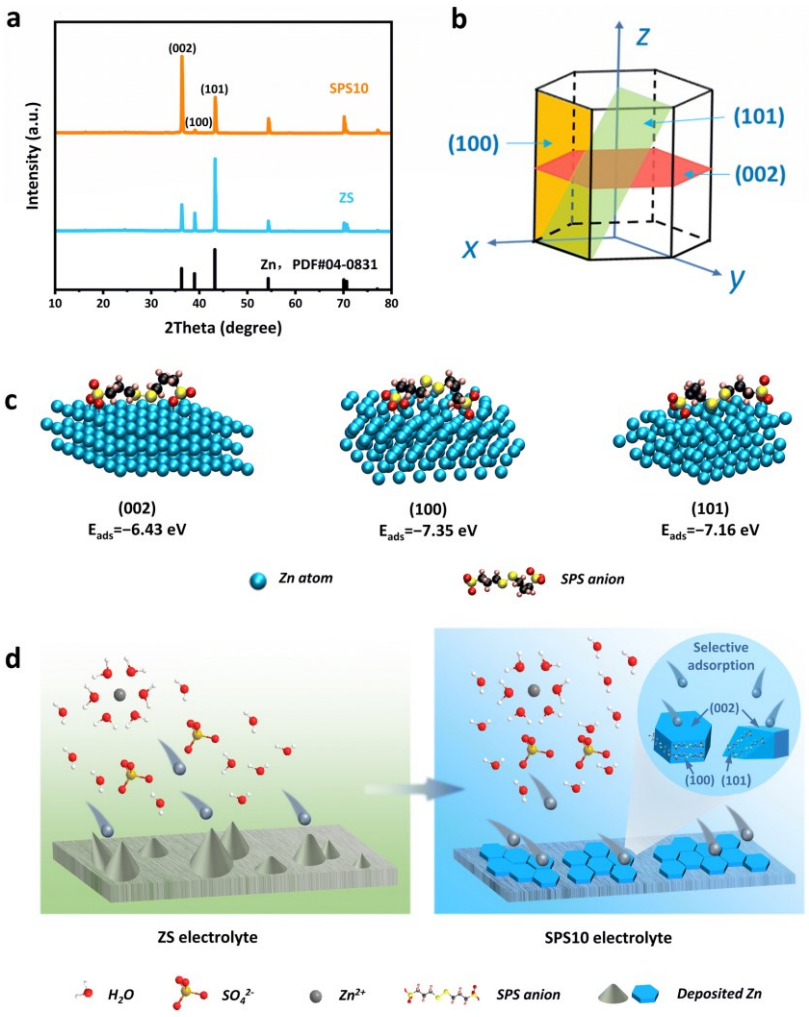

Figure 16. (a) XRD of Zn^{2+} deposition in the orientation of (0 0 2), (1 0 1), and (1 0 0) with and without SPS. (b) Crystal structure of Zn (c) Absorption energy of SPS anion on Zn surface in the orientation of (0 0 2), (1 0 1), and (1 0 0). (d) Schematic of Zn^{2+} deposition with and without SPS. Copyright 2023, Royal Society of Chemistry

Additionally, Zhou et al. (43) illustrate the impact of sodium lignosulfonate (SL) on promoting uniform Zn^{2+} deposition. SL has negatively charged sulfonic groups that can interact with Zn^{2+} and reduce the Zn nucleation overpotential. It also has phenolic hydroxyl groups that can interact with water molecules and form hydrogen bonding. This affects the Zn^{2+} solvation structure and leads to a better Zn^{2+} desolvation process. Furthermore, SL tends to be absorbed on the protrusion of deposited Zn and form a protective shield to isolate the contact between water

molecules and Zn surface, which results in more uniform Zn deposition and suppression of side reaction (Fig. 17d). The cycling rate performance in Fig. 17a shows excellent tolerance and stability in Zn//Zn symmetric cell with SL as surfactant. Without the addition of SL, the symmetric cell failed when the current density increases to 4 mA cm^{-2}. Long cycling performance in Fig. 17b-c shows excellent stability at 0.5 mA cm^{-2}, 0.5 mAh cm^{-2} for 600 cycles, and 4 mA cm^{-2}, 4 mAh cm^{-2} for 1200 cycles with the addition of SL in the electrolyte.

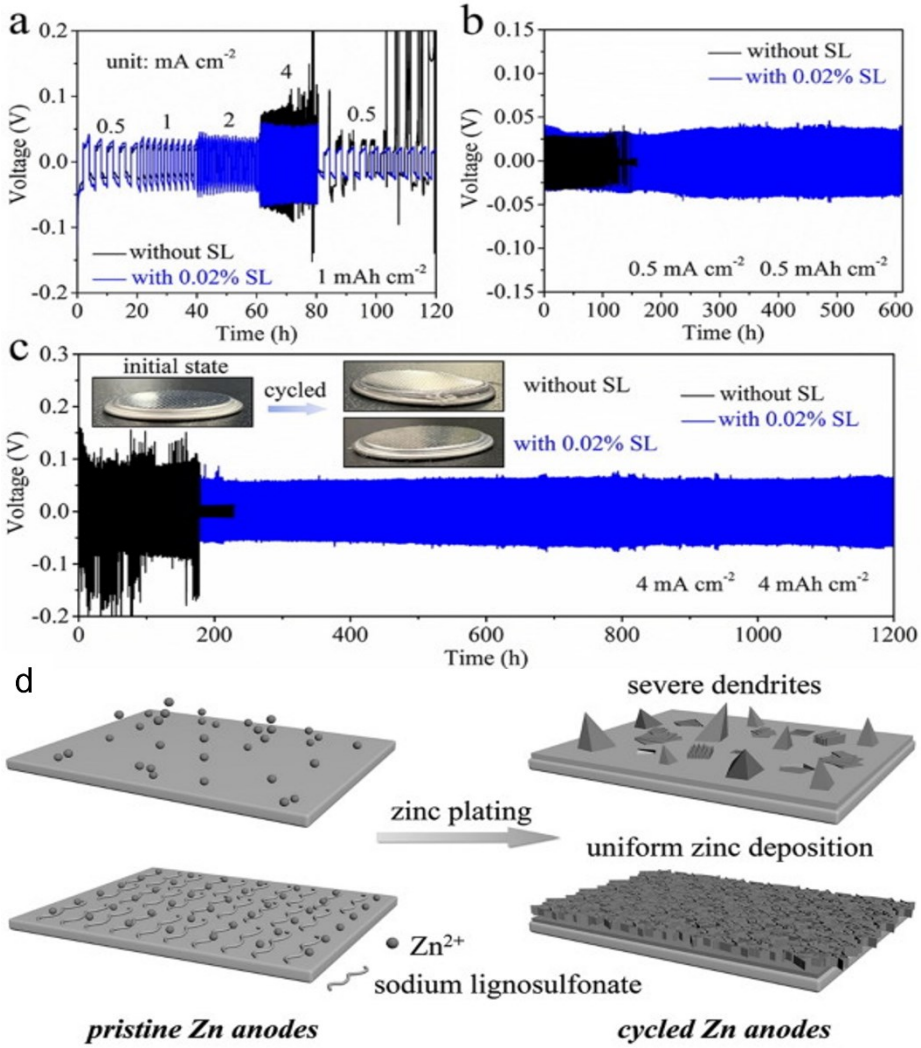

Figure 17. (a)Rate performance of symmetric cell at 0.5, 1, 2, 4 mA cm^{-2} with and without SL. (b) Cycling performance of symmetric cell at 0.5 mA cm^{-2} and 0.5 mAh cm^{-2} with and without SL. (c) Cycling performance of symmetric cell at 4 mA cm^{-2} and 4 mAh cm^{-2} with and without SL. (d) Schematic of Zn^{2+} deposition with and without SL. Copyright 2021, Elsevier

Amphoteric surfactants have both anion and cation in their hydrophilic groups. Lu et al. (44) introduced arginine in the electrolyte and analyzed the absorption of arginine on the Zn surface. By introducing the arginine additive, the positively charged arginine adsorbs on the Zn surface and hinders the adsorption of H2O molecules, which limits the growth of dendrites and results in the formation of a stable zinc-electrolyte interface (Fig. 18a). At the condition of 5mA cm^{-2} and 4mAh cm^{-2}, the symmetric cell has cycled for 2200 hours with excellent stability in arginine electrolyte (Fig.18b). Without arginine additive, the symmetric cell only cycled for 80h and get short circuit. By performing the DFT calculation, arginine has the largest absorption energy, especially for the positively charged arginine (Fig. 18c). This result further proves the great absorption of arginine on the Zn surface and regulation of Zn^{2+} flux during plating. A high and long-cycled CE of 98.26% is also obtained with the addition of arginine (Fig. 18d).

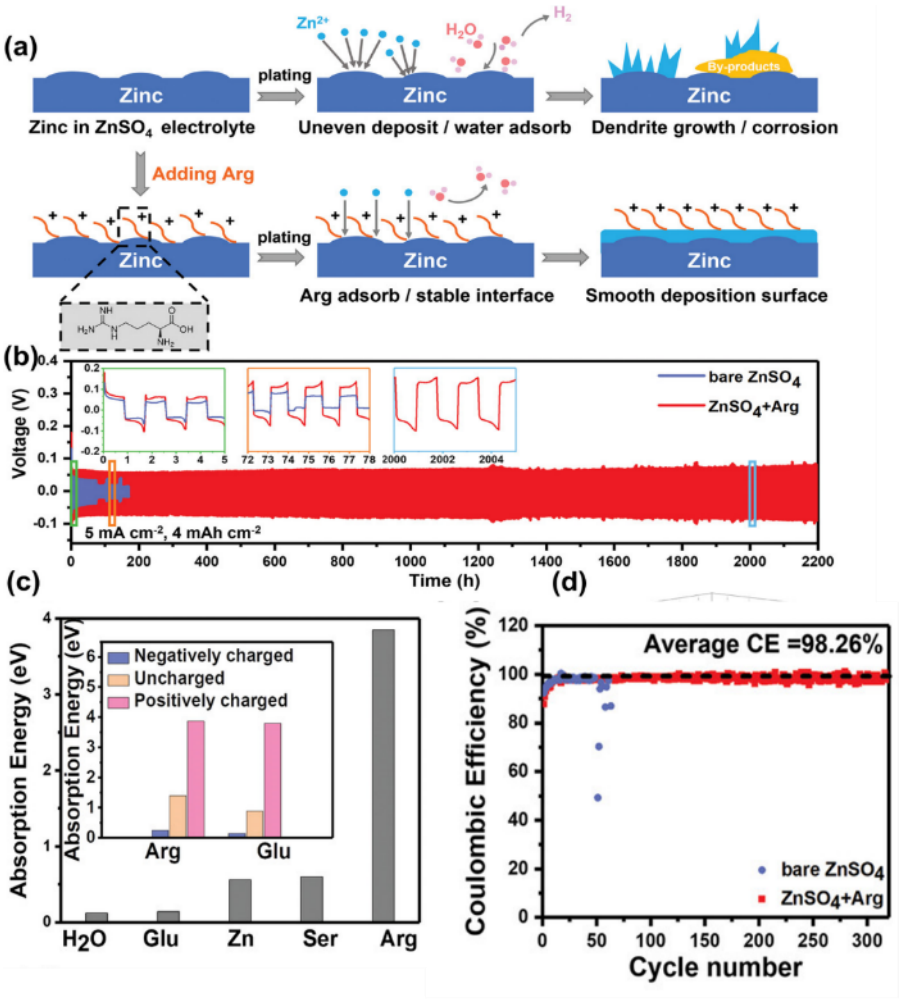

Figure 18. Schematic of Zn^{2+} deposition with and without arginine. (b) Cycling performance of symmetric cell at 5mA cm^{-2} and 4mAh cm^{-2}. (c) Absorption energy of H_2O, Glu, Zn, Ser, and Arg on Zn surface. Inset is the absorption energy of Arg and Glu with negatively charged, uncharged, and positively charged. (d) CE of asymmetric cell with and without arginine. Copyright 2021, Wiley

Non-ionic surfactants have a non-electrically charged group. Similar to all other surfactants, the non-ionic surfactant is usually absorbed on the Zn surface and protects the Zn surface from the formation of uneven Zn dendrite. Lu et al. (45) reported a non-ionic surfactant of polyethylene oxide (PEO) in $ZnSO_4$ electrolyte and shows tremendous cycling performance. The long chain PEO tends to absorb on the Zn surface and isolate the water molecules from the Zn surface to

restrict hydrogen evolution reaction. Furthermore, the viscosity of the electrolyte is modified, resulting in a suppressed Zn^{2+} diffusion kinetic, which ensures a slow and uniform Zn deposition (Fig. 19a). SEM in Fig. 19c-d shows sharp Zn dendrites that grow vertically in the non-PEO electrolyte. These dendrites will eventually cross through the separator and cause a short circuit. In the PEO electrolyte, Zn^{2+} deposits horizontally on the surface, and a more uniform surface is obtained (Fig. 19e-f). Furthermore, a high CE that is greater than 99% is achieved for 1500 cycles in PEO electrolyte. Without PEO, the CE is relatively low and decreases after 120 cycles (Fig. 19g).

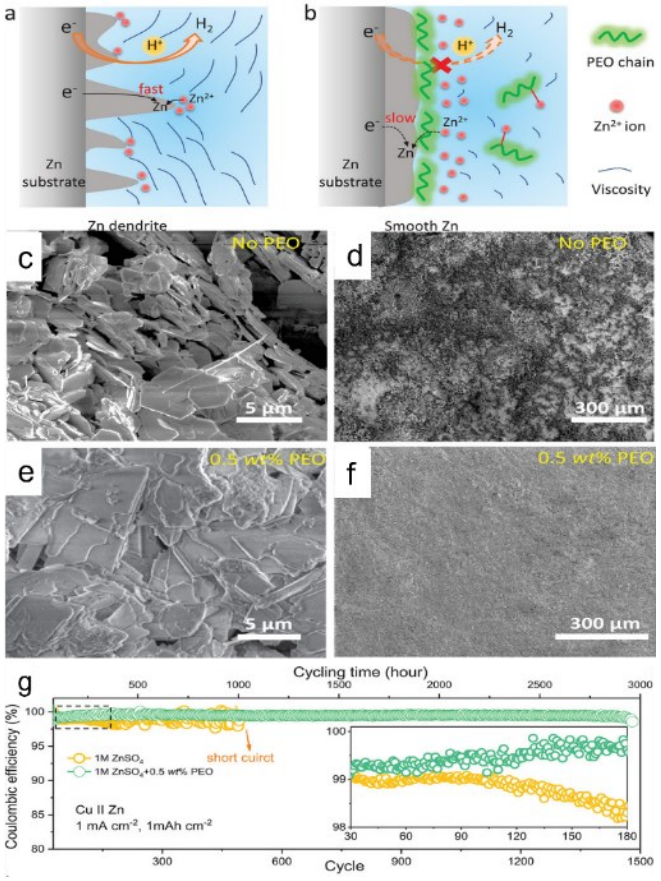

Figure 19. (a) Schematic of Zn^{2+} deposition in the bulk electrolyte. (b) Schematic of Zn^{2+} deposition in PEO electrolyte. (c-d) SEM image of cycled Zn electrode in the bulk electrolyte. (e-f) SEM image of cycled Zn electrode in PEO electrolyte. (g) CE of asymmetric cells with and without PEO. Copyright 2020, Wiley

1.6 Objectives and Design

The objective of this work is to develop a zinc ion battery using organic solvent as co-solvent with water. After in-depth learning of electrolytes from the literature review in Chapter 1, the research gaps are identified in the following aspects:

- Many studies have discussed the function of organic solvent in solvation structure manipulation. Most of them only analyze the relation between organic molecules and water molecules, however, only few of them analyze the relation between salt anions, organic molecules and water molecules.
- There are very few simulations and characterization, including MD and CV, in a low temperature condition.

According to these research gaps, the following objectives will be obtained:

- Create a MD simulation cell contains both salt anions, water molecules and organic molecules. Then calculate the coordination number of Zn^{2+} ions interacting with salt anions, water molecules and organic molecules.
- Create a MD simulation cell in the condition of -18°C and calculate the corresponding coordination number for each pair.
- Performance characterization such as CV and linear polarization curve in the condition of -18°C.

To achieve these objectives, the design procedures are determined. The selection of organic solvent is considered in the following aspects:

- The interaction of Zn^{2+} and organic molecule is stronger than Zn^{2+}-H_2O.
- The freezing point of organic solvent is low.
- The organic solvent is miscible in water.

In addition, theoretical simulation and electrochemical performance are required for analysis:

- DFT calculation of binding energy, HOMO LUMO level, absorption energy, etc.
- MD simulation for analyzing Zn^{2+} solvation structure.

- XPS spectra for analyzing the component of the SEI layer.
- SEM image of Zn^{2+} deposition for analyzing zinc dendrite growth.
- Electrochemical performance of asymmetric cells, symmetric cells, and full cells.

Table 1. List of highly concentrated electrolytes with corresponding symmetric cell cycling performance and asymmetric cell CE performance.

Electrolyte	(mA cm^{-2} mAh cm^{-2}) lifespan	CE	Reference
4.2M $ZnSO_4$ + 0.1M $MnSO_4$	0.5, 1, 1000h	99%	(22)
1m $Zn(TFSI)_2$ + 20m LiTFSI	0.2, 0.033, 170h	99.7%	(23)
30m $ZnCl_2$	0.2, 0.035, 600h	95.4%	(24)
1m $Zn(OTF)_2$ + 20m LiTFSI	-	98.9%	(25)
3M $ZnSO_4$	20, 1, 800h	100%	(46)
3M $ZnSO_4$ + 2M LiCl	0.2, 2, 170h	-	(47)
3M $Zn(OTF)_2$	0.1, 0.1, 800h	100%	(48)
30m $ZnCl_2$ + 5m LiCl	2, 4, 4000h	99.7%	(49)
2.4 m Zn(ClO4)2	1, 1, 3000h	99%	(50)
8 M $NaClO_4$ + 0.4 M $Zn(OTF)_2$	1, 1, 200h	-	(51)
8 M $NaClO_4$ + 0.4 M $Zn(CF_3SO_3)_2$	1, 1, 200h	-	(52)
1 M $Zn(OAc)_2$ + 31 M KOAc	-	99.2%	(53)
0.5 m $Zn(ClO_4)_2$ with 18 m $NaClO_4$	0.2, 0.04, 1200h	-	(52)

Table 2. List of organic solvents with corresponding symmetric cell cycling performance and asymmetric cell CE performance.

Organic solvent	(mA cm^{-2} mAh cm^{-2}) lifespan	CE	Reference
Diethyl ether (Et_2O)	0.2, 0.2, 250h	-	(54)
Ethylene glycol (EG) (40%)	2, 1, 140h	-	(26)
Triethyl phosphate (TEP)	0.5, 1, 3000h 0.25, 1, 3000h 0.1, 1, 3000h	99.6%	(28)
Gamma butyrolactone (GBL)	1, 1, 4000h 10, 10, 1170h 20, 20, 140h	99.9%	(55)
Tripropylene glycol (TG)	1, 0.5, 1100h 2, 0.67, 1000h	99.7%	(56)
Hexaoxacyclooctadecane	1, 1, 2400h	99.6%	(57)
Trimethyl phosphate (TMP)	1, 0.5, 5000h 5, 2.5, 4000h	99.5%	(58)
EDTA	1, 0.5, 1800h 5, 2.5, 500h	99.2%	(59)
EG (60%)	0.5, 0.5, 2668h	-	(60)
Polyethylene glycol (PEG)	1, 1, 650	99.6%	(61)
Methanol (50%)	-	99.7%	(62)
Anhydrous Acetonitrile (ACN)	1, 1, 1300h	99.3%	(63)
EG (50%)	1, 1, 1200h	-	(64)
Acetonitrile (AN)	1, 2, 530h	99.6%	(65)
Acetonitrile	1, 0.5, 400h	99.8%	(66)
Acetonitrile	1, 1, 2500h	-	(67)
1,2- dimethoxy ethane (DME)	0.5, 0.125, 480h	99.4%	(68)
Dimethyl carbonate (DMC)	1, 0.5, 1000h	99%	(30)
Triethyl phosphate (TEP)	1, 1, 1500h	99.5	(69)
Trimethyl phosphate (TMP)	1, 1, 2000h	99.5%	(70)
1,2- dimethoxy ethane (DME)	2, 2, 380h	-	(71)
1,4-dioxane (DX)	5, 2.5, 600h	99.8%	(72)
Dimethyl sulfoxide (DMSO)	0.5, 0.5, 1000h	99.5%	(29)

Dimethyl sulfoxide (DMSO)	1, 1, 2100h	99.7%	(73)
Polyacrylamide (PAM)	1, 1, 180h	100%	(74)
1,3-dioxolane (DOL)	1, 1, 1000h	98.6%	(75)
Diethyl ether (Et_2O) and ethylene glycol (EG)	0.5, 0.5, 700h	98%	(76)
Polyethylene glycol (PEG)	1, 1, 9000h 0.5, 1, 8000h 2, 1, 8000h	-	(77)
1,2-dimethoxyethane (DME)	2, 1, 5000h 5, 1, 5000h 10, 1, 800h	99.7%	(32)
N, N-dimethyl acetamide (DMA)	3, 3, 1000h 1, 0.5, 4500h	99.6%	(78)
2- Bis(2-hydroxyethyl) amino-2-(hydroxymethyl)-1,3-propanediol (BIS-TRIS)	1, 1, 1200h 5, 5, 600h	98.5%	(79)
Glycerol	1, 1, 1500h 0.5, 0.5, 1500h 0.2, 0.2, 1500h 2, 6, 900h 1, 3, 450h	98.3%	(31)

Table 3. List of Metal-ion additives with corresponding symmetric cell cycling performance and asymmetric cell CE performance.

Metal-ion additive	(mA cm^{-2} mAh cm^{-2}) lifespan	CE	Reference
$Mn(CF_3SO_3)_2$	0.1, 0.1, 280h	-	(16)
$PbSO_4$	-	-	(37)
$NiSO_4$	-	-	(37)
$CuSO_4$	-	-	(37)
Na_2SO_4	0.2, -, 300h	-	(38)
$CoSO_4$	-	-	(80)
$CeCl_3$	2, 1, 2600h 40, 10, 160h	99.7%	(36)
LiCl	0.2, -, 160h	-	(81)

Table 4. List of SEI forming additive with corresponding symmetric cell cycling performance and asymmetric cell CE performance.

SEI forming additive	(mA cm^{-2} mAh cm^{-2}) lifespan	CE	Reference
$Zn(H_2PO_4)_2$	1, 1, 1200h 1, 5, 800h 5, 1, 200h	99.4%	(82)
2-methyl imidazole (Hmim)	2, 2, 2000h 4, 4, 400h 8, 8, 250h	98.93%	(83)
Trimethyl phosphate (TMP)	1, 0.5, 5000h 5, 2.5, 4000h	99.5%	(58)
Triethyl phosphate (TEP)	1, 1, 1500h	99.5	(69)
Polyethylene glycol (PEG)	1, 1, 9000h 0.5, 1, 8000h 2, 1, 8000h	-	(77)
1,2-dimethoxyethane (DME)	2, 1, 5000h 5, 1, 5000h 10, 1, 800h	99.7%	(32)
ZnS artificial layer	2, 2, 1000h	99.2%	(84)
ZnS artificial layer	1, 0.5, 700h	-	(85)
poly(ethylene glycol)-200	1, 1, 1600h 0.25, 0.5, 1100h	99.23%	(86)
DX	0.5, 2.0, 5000h	99%	(87)
20 mM Zn(NO3)2	0.5, 0.5, 1200h	99.8%	(88)
Graphene Oxide (GO)	1, 0.5, 600h 5, 2.5, 400h 10, 5, 140h	99.1%	(39)
Dopamine	1, 1, 1000h 10, 10, 200h 30, 30, 75h	99.5%	(89)
Trimethylethyl ammonium trifluoromethane sulfonate ($Me_3EtNOTF$)	0.5, 0.25, 6000h	99.6%	(90)

Table 5. List of Surfactant additives with corresponding symmetric cell cycling performance and asymmetric cell CE performance.

Surfactant additive	(mA cm^{-2} mAh cm^{-2}) lifespan	CE	Reference
Tetrabutylammonium sulfate (TBA_2SO_4)	2, 2, 300h 5, 2, 450h 10, 2, 400h 5, 5, 160h	-	(40)
Triethylmethyl ammonium (TMA)	1, 0.5, 2145h 5, 2.5, 500h	-	(41)
Benzyltrimethylammonium chloride	1, 2, 1000h 2, 2, 900h 5, 5, 500h 10, 5, 400h	-	(91)
3,30 -dithiodipropane sulfonate (SPS)	1, 1, 4400h 5, 5, 870h	99.7%	(42)
Sodium lignosulfonate (SL)	0.5, 0.5, 600h 4, 4, 1200h	99.92%	(43)
Arginine (Arg)	5, 4, 2200h 10, 4, 900h	98.26%	(44)
Polyethylene oxide (PEO)	-	98.9%	(45)
Tetraethyl ammonium bromide (TEAB)	1, 1, 3000h	99.73%	(92)
Tetramethylammonium sulfate (TS)	0.25, 0.125, 4500h 10, 2, 1000h	99.7%	(93)
Sodium dodecyl benzene sulfonate (SDBS)	0.5, 0.5, 1500h	-	(94)
Cysteine (Cys)	0.5, 0.5, 2300h 3, 3, 900h 5, 5, 600h	99.4%	(95)
Threonine (TH)	1, 1, 580h 5, 1, 700h	99.5%	(96)
polyacrylamide (PAM)	2, 2, 1300H	99.6%	(97)
Acrylamide-*co*-methyl acrylate	1, 1, 8800h 5, 5, 2500h 10, 10, 765h	99.3%	(98)

1.7 Conclusion

In conclusion, as an effective and practical strategy, electrolyte engineering plays a great role in protecting the zinc anode surface and anode-electrolyte interface. In this paper, various strategies for the manipulation of solvated structures, the inhibition of zinc dendrites, and the suppression of side reactions in electrolyte engineering are introduced in detail and their recent progress is highly summarized. These strategies include increasing the concentration of electrolyte salts and adding organic solvents, metal ion additives, SEI layer-forming additives, and surfactants to the aqueous electrolyte. Highly concentrated electrolytes can promote salt anions into the solvation layer and replace water molecules, reduce the activity of water, and widen the electrochemical potential window. The addition of organic solvents can change the solvation structure, reduce the desolvation energy of Zn^{2+}, generate the SEI layer to protect the anode and expand the adaptability of zinc-ion batteries at low-temperature conditions. Metal-ion additives with higher reduction potential can be reduced to the zinc surface before Zn^{2+} deposition, thus providing more depositional active sites for uniform deposition of zinc. Metal-ion additives with low reduction potential are adsorbed on the tip of zinc as an electrostatic shield, which repels further deposition of zinc ions on the tip and inhibits 2D diffusion of Zn^{2+}. SEI layer-forming additives participate in the decomposition of the electrolyte, forming SEI protective films that isolate the water molecules and inhibit further decomposition of the electrolyte. The surfactant can be adsorbed on the electrode to isolate the contact between water molecules and the zinc anode and promote the Zn^{2+} diffusion kinetic.

Although electrolyte engineering has made progress in inhibiting zinc dendrite and hydrogen evolution reactions, these strategies still have the following defects and problems that need to be considered: 1. For high-concentration electrolytes, increasing salt concentration will lead to higher viscosity and thus lower ionic conductivity in the electrolyte. In addition, high-concentration electrolytes are highly polarized and may enhance the self-discharge of the battery. For positive electrode materials, the environment of high-concentration electrolytes will promote the

dissolution of positive electrode materials and the collapse of the structure, thus leading to the attenuation of battery capacity. 2. For organic solvents, some organic solvents may promote the decomposition of the electrolyte. Some organic solvents may influence the corrosion and dissolution of the electrode material. Therefore, it is important to select suitable organic solvents and electrolytes. At the same time, the organic solvent will increase the viscosity of the electrolyte, resulting in low ionic conductivity. 3. For additives, some metal ion additives such as $CuSO_4$ will produce bubbles on the surface of zinc, which will not only promote hydrogen evolution reaction but also affect the uniform deposition of Zn^{2+}. The thickness of the SEI layer also has a great impact on the performance of the battery. If the thickness of the SEI layer is too thin, the zinc dendrites may puncture the SEI layer, resulting in corrosion and uneven deposition of the zinc surface. If the thickness of the SEI layer is too thick, the transport and deposition of Zn^{2+} will be greatly limited.

Learning and understanding the mechanism behind each electrolyte is necessary and important. Therefore, theoretical simulation and calculation including DFT calculation and MD simulation have become a critical analysis for further understanding the solvation structure and interaction and bonding energy between ions. Combining theoretical and experimental analysis and promoting electrolyte engineering in aqueous zinc-ion batteries will eventually result in practical application that benefits every human being in the future.

Chapter 2. Methodology

2.1 X-ray diffraction (XRD)

XRD is an accurate and efficient testing technique for materials. Since X-rays have great energy, the atoms in the crystal will emit secondary waves when X-rays enter the crystal. This process is called X-ray scattering. The XRD diffractometer has three main parts: X-ray source, sample, and detector. When the X-ray is generated from the X-ray source and passes through the sample material, the incident X-ray is reflected at a certain angle and collected by the detector. By adjusting the incident angle, the corresponding wavelength information will be collected by the detector. Eventually, a diagram of intensity versus angle is obtained. Phase analysis is the most common application of XRD testing. The diffraction pattern of each phase is unique, we can get the phase composition of the measured sample if we compare the measured XRD pattern with the standard card in the database. The fundamental of XRD theory is the Bragg equation, which shows the intrinsic relationship between diffraction and crystal structure. The equation is shown as the following:

$$n\lambda = 2\mathrm{d}\sin\theta$$

Where λ represents the wavelength of the X-ray, d represents the distance between the crystal planes and θ represents the angle between the incident X-ray and the corresponding crystal plane.

2.2 X-Ray Photoelectron Spectroscopy (XPS)

XPS technology is used for qualitative and quantitative analysis of the composition and content of elements on the surface of materials. When an X-ray with a certain energy is emitted to the surface of the sample, it interacts with the surface atoms of the sample to be measured and electrons gain energy. When the electron energy is greater than the binding energy of the nucleus, the electrons in the atoms can be excited to break away from the atoms and become free electrons. The free

electron is detected by the detector and binding energy information is shown in a diagram based on the following equation:

$$E_b = hv - E_k$$

Where E_b represents the binding energy of electrons for a specific element, E_k represents the maximum kinetic energy of emitted electron and hν represents the energy of incident X-ray. In this equation, hν is known and E_k can be measured, therefore the binding energy E_b can be determined. Since the binding energy of electrons in the same electron shell of different atoms is different, the binding energy can be used for element identification. In this research, the composition on the surface of cycled Zn electrode is obtained according to the position and shape of the XPS spectrum.

2.3 Scanning Electron Microscope (SEM)

The scanning electron microscope (SEM) is a commonly used microscopy and analysis instrument that utilizes various physical signals, which are excited by an electron beam scanning the surface of a sample, to modulate images. The scanning electron microscope mainly consists of the following parts: an electron gun, electromagnetic lens, scanning coils, electron detector, and TV scanner. The electron beam generated by the electron gun passes through the electromagnetic lens, then the scanning coil controls the electron beam to scan the sample. These interactions generate various physical signals, and the detector converts the physical signals into image information. Three types of electrons generate image signals in the SEM: secondary electron, backscattered electron, and dispersive x-ray. Secondary electrons are the nuclear electrons that leave the atom of the sample due to an incident electron beam. They have very low kinetic energy, which means that they are used for displaying surface topography. Backscattered electrons are the incident electrons that are reflected by atoms of the sample. They have higher kinetic energy than secondary electrons and they increase as the atomic number increases. Therefore, backscattered electrons can be used to identify the different chemical compositions on the surface of the sample. Dispersive X-ray is produced due to the large energy barrier when the inner shell electrons leave the atom and outer

shell electrons transit to the inner shell. Therefore, the dispersive X-ray can be used for element mapping since each element has a different energy level.

2.4 Raman spectroscopy

Raman spectroscopy is a branch of light scattering. When a light beam is shot on the material, the photon interacts with a molecule, the molecule absorbs the energy of the photon and transit to a higher energy level. However, the molecule is unstable at a high energy level and must return to a lower energy level. During the transition of the molecule from a high energy level to a lower energy level, energy will be released in the form of a photon. If the molecule transit back to its original energy level, the released photon frequency will remain unchanged. This scattering model is called Rayleigh scattering. If the molecule transit to a lower or higher original energy level, the released photon frequency will be shifted. This scattering model is called Raman scattering. The shifted photon frequency is called the Raman shift. Raman shift is independent of the frequency of the incident light. It is related to the vibrational energy levels of the material. Raman spectroscopy has multiple Raman peaks, and each peak represents a specific molecular bond vibration. Each substance has its own characteristic Raman spectrum, and the frequency of each Raman peak is very sensitive to small changes in the structure of the substance. Therefore, Raman spectroscopy is used to analyze the change in structure and the chemical composition of material by comparing it with the standard Raman spectroscopy in the database.

2.5 Nuclear Magnetic Resonance (NMR) spectroscopy

Nuclear magnetic resonance (NMR) is a tremendous technique that is used in many fields of science. It can provide the chemical structure information and help researched further understanding any structure manipulation of a matter. The concept of NMR could be explained in three aspects: nuclei, magnetism and resonance. Each matter is made up of atoms and atoms

contain nuclei and electrons. For those magnetic nuclei, they will have a motion of self-rotating which just like earth's rotation, which is also called spin. Spin is the intrinsic property of a matter, which is quantified as spin quantum number I. The spin quantum number is either an integer (1, 2, 3, etc.), a fraction (1/2, 3/2, 5/2, etc.) or zero for each particular nucleus. The spinning charges create magnetic field and the atomic nuclei will act as magnetic diploes. When an external magnetic field B is applied on the nuclei, the spinning of nuclei will be affected and leads to 2I + 1 spinning orientations. The 2I +1 spinning orientation causes 2I +1 energy states. If there is an energy applied to the nuclei, each nucleus will perform an energy level transition and create a resonance signal. The energy is offered by a radio frequency transmitter. Due to the interaction of nuclei with electron clouds, each nucleus will eventually be sensitive to a certain radio frequency and lead to a change in resonance lines. The change of resonance peak to a higher or lower frequency is called chemical shift, which is used to analyze the chemical structure of a matter.

2.6 Cyclic Voltammetry (CV)

Cyclic Voltammetry (CV) is a technique used to study the behavior of electrochemical reactions at the electrode - electrolyte interface. In general, it is used to study the electrode reaction mechanism, reaction kinetic, etc. The basic principle of cyclic voltammetry test is to apply a triangular waveform pulse voltage to the electrodes, the working electrode will undergo oxidation reaction or reduction reaction by changing the potential at the working electrode. For example, when a more positive potential is applied and the potential continuously decrease to the standard electrode potential for the electrode material, the electrode will gain electrons, perform reduction reaction and produce current. As the potential keep decreasing, the concentration of reactants decreases in the system and eventually reaches zero. The current will firstly increase, then decrease as the concentration of reactants decrease and reach zero eventually. Therefore, the CV will obtain a reduction peak in the current-potential plot. In reverse, oxidation reaction will happen and an oxidation peak will be obtained when the CV scan from a lower potential to a higher potential. These oxidation/reduction peak represent any electrochemical reactions happened at the potential.

Therefore, CV plot can provide information of reversibility and electrochemical reaction from the peaks and information of diffusion kinetic from the reaction current density.

2.7 Coulombic Efficiency (CE)

Coulombic Efficiency (CE) represent the capacity retention during each charge/discharge cycle. The less the capacity loss during cycling, the higher the CE and the longer the cycling life of batteries. CE is calculated by on the charge capacity and discharge capacity:

$$CE = \frac{Discharge\ capacity}{Charge\ capacity}$$

In zinc ion batteries, it could be written as:

$$CE = \frac{Number\ of\ Zn^{2+}\ intercalated\ in\ cathode}{Number\ of\ Zn^{2+}\ departed\ from\ cathode}$$

A poor CE is caused by the side reaction happened in the electrolyte. The Zn^{2+} ions engage with OH^- anions and form irreversible by-products. Therefore CE is a parameter for analyzing the reversibility in zinc ion batteries.

2.8 HOMO LUMO

HOMO and LUMO are molecular orbitals that is used to define the chemical reaction between molecules. HOMO stands for highest occupied molecular orbital and LUMO stands for lowest unoccupied molecular orbital. According to frontier molecular orbital theory, in a molecule, HOMO has the highest energy and least restriction. The higher the HOMO level, the easier the molecule lose electrons. LUMO has the lowest energy, therefore, the lower the LUMO level, the easier the molecule gain electrons. The energy difference between HOMO and LUMO is called HOMO LUMO. A small HOMO LUMO gap results in a high HOMO level and low LUMO level, which means the molecule is unstable and chemical reaction is easier to happen.

2.9 Molecular Dynamic

Molecular Dynamics (MD) is a technique that combines mathematics, physics, chemistry, and biology. This method is widely used in molecular simulation. Molecular dynamics simulation relies on computer to build molecular models to simulate the microstructure mechanism and dynamic trajectory behavior of molecules, to obtain the physical and chemical data of molecular systems. In the simulation of molecular dynamics, each atom in the system is regarded as a particle obeying Newton's second law. According to the potential energy function of the molecule, the force acting on each atom is obtained. Given the initial velocity and the step size of evolution, the motion trajectory of the atom on the potential energy surface is obtained by solving the motion equation using Newton's law of motion. In a certain time, by simulating the motion state of molecules and atoms in the system, the evolution behavior of the system with time can be observed in a dynamic way. Atoms are composed of nuclei and electrons, and the mass of electrons is extremely small compared to the nucleus, so when the atom moves, the movement of electrons can be ignored, and only the nucleus moves in the selected conservative force field. In MD calculation simulation, according to different systems, appropriate algorithms are selected, parameters are set, and time steps of nanoseconds and milliseconds are adopted to solve these equations, so that the system can undergo motion evolution in a period of time. At the same time, the system is heated and pressurized, maintained at the set parameter values, and atomic coordinates are written to the output file within a certain time interval. In the set simulation time, the constantly changing coordinates form a movement trajectory of the system. In the early stage of the simulation, the initial system will constantly change, and after a period of time, it will stabilize within a certain range. At this time, the system basically reaches a state of equilibrium. After the equilibrium trajectory of the system is obtained, the average value is calculated and written into the output file, and the macro properties of the simulated system are extracted and analyzed from the file.

Chapter 3. Rational design of electrolyte for stable and low-temperature Zinc-ion battery

3.1 Abstract

Aqueous zinc-ion battery suffers from poor cycling stability due to uneven Zn^{2+} deposition and serious dendrite growth. To effectively protect the Zn metal anode, focusing on de-solvation of $[Zn(H_2O)_6]^{2+}$, diglyme (G2) is added as the co-solvent with $Zn(OTF)_2$. The addition of G2 solvent can efficiently reconstruct the Zn^{2+} solvation structure and reduce the water molecule content of $[Zn(H_2O)_6]^{2+}$ sheath. More importantly, an organic and inorganic SEI layer (ZnF_2-$ZnCO_3$-$ZnSO_3$) is formed on the Zn anode surface, which isolates the Zn anode from the bulk electrolyte and allows uniform and suppressed Zn^{2+} diffusion. Zn corrosion and side reactions are suppressed as well in the system. High Coulombic efficiency of 99.7% is obtained in a co-solvent electrolyte system (i.e., 2M $Zn(OTF)_2$ and G2). Long cycling life of 1000 cycles with capacity retention of 80% is demonstrated by Zn//I_2- AC full cell at room temperature. Even under a low-temperature condition (-18°C), Zn//I_2- AC full cell can have a lifespan of 1000 cycles with capacity retention of 65%. Theoretical calculations (e.g., DFT, MD) also prove that the OTF^- ion has greater interaction with Zn, and the water molecules from the $[Zn(H_2O)_6]^{2+}$ solvation structure are replaced by OTF^- ions. This work demonstrates a direction and unparalleled insight into electrolyte engineering with solvation structure regeneration and SEI player formation for aqueous zinc-ion batteries.

3.2 Introduction

Compared with lithium-ion batteries, the rechargeable aqueous zinc-ion battery (AZIB) has been considered a promising and reliable energy storage technology because of its low cost, environmental benignity, and high safety(99-101). Zinc metal has the advantages of low redox potential (- 0.76 V *vs* the standard hydrogen electrode (SHE)), and high theoretical capacity (820 mAh g^{-1})(55, 102, 103). However, there are some critical problems and challenges regarding the use of Zn anode, including the growth of dendrite(54, 104) from uneven Zn^{2+} deposition, compete reaction of hydrogen evolution reaction (HER)(105), and Zn surface corrosion(84). These issues cause a low Coulombic efficiency (CE), short cycling life, and irreversible consumption of the battery(77).

In the zinc aqueous electrolyte, water molecules usually tend to solvate Zn^{2+} ions and form a solvation sheath of $[Zn(H_2O)_6]^{2+}$ (106). This $[Zn(H_2O)_6]^{2+}$ solvation sheath requires a large energy barrier to overcome for the zinc ion desolvation and causes many water molecules on the Zn anode. Water molecule is thermodynamically unstable due to the higher potential of H2O/H^{2+} (0 V vs SHE) compared to Zn/Zn^{2+} (-0.76V vs SHE)(107). Therefore, the hydrogen evolution reaction happens spontaneously. The continuous evolution of H_2 causes the change of local pH of electrolytes and easily results in the formation of inactive by-products such as $Zn(OH)_2$(56, 57). These by-products are ionically insulating and unevenly growing, which results in poor ion diffusion, zinc anode corrosion, and dendrite growth. Therefore, it is urgently necessary to optimize the solvation structure to inhibit hydrogen evolution reaction and uneven Zn deposition(108).

Several strategies have been investigated for optimizing the solvation structure. One solution is to use highly concentrated electrolytes(2, 52, 60). Increasing the concentration of zinc salts can reduce the activity of water molecules and increase the number of anions from the salts that pair the Zn^{2+} ions. The solvation structure is optimized, and a better Zn deposition is realized. However, the increased concentration of zinc salts also results in high viscosity, low ionic conductivity, and

high cost. Another way is to use organic solvent additives to modify solvation structure(79, 109, 110). Organic solvents such as 1, 2-dimethoxyethane (DME)(32), N, N-dimethyl acetamide (DMA)(78), dimethyl carbonate (DMC)(30), and dimethyl sulfoxide (DMSO)(29) have been reported as great additives to alter the solvation structure. These organic solvents have high donor numbers and tend to inhibit free water molecules in the electrolyte. Water molecules in $[Zn(H_2O)_6]^{2+}$ solvation sheaths are replaced by these organic additives which restrain the hydrogen evolution reaction and dendrite growth. Furthermore, building a protective solid electrolyte interface (SEI) layer on the Zn surface has been reported as well(13, 58, 82, 83, 85, 86). Zhang's group reported that using triethyl phosphate (TEP) as a solvent in the electrolyte of $Zn((CF_3SO_3))_2$ could form an organic-rich outer layer and an inorganic $Zn(PO_4)_2$-ZnF_2-ZnS rich inner layer on the Zn surface. The hybrid SEI layer isolates active Zn from electrolytes and suppresses the hydrogen evolution reaction and dendrite growth.

Herein, a novel electrolyte system consisting of 2.0 M $Zn((CF_3SO_3))_2$ ($Zn(OTF)_2$) in water with diglyme (G2)(111, 112) solvent is developed in this context. In a comprehensive analysis of theoretical calculations including molecular dynamics (MD) simulations(113) and density functional theory (DFT) calculations, G2 solvent is capable to reconstruct the solvation structure of $[Zn(H_2O)_6]^{2+}$ by reducing the numbers of water molecules and increasing the number of OTF^- anion, which suppresses the dendrite growth and inhibits the side reaction. Meanwhile, a polymer inorganic SEI layer composed of ZnF_2, $ZnCO_3$, and $ZnSO_3$ derived from the reductive decomposition of G2 solvent and OTF^- anion. The SEI layer restrains the corrosion on the Zn surface and allows a more even Zn deposition. With the addition of G2 solvent, a Zn//Zn symmetric cell using thin Zn shows cyclability of 160 h under the current density of 1 mA cm^{-2} and areal capacity of 1 mAh cm^{-2}. When coupled with iodine-activated carbon, the full cell shows a long cycling performance over 1000 cycles at 0.5 A g^{-1} with a capacity of 100 mAh g^{-1}. In addition, G2 has a very low melting point of -64 °C. With the addition of G2 solvent, the full cell coupled with iodine-activated carbon shows a long cycling performance over 1000 cycles at 0.5 A g^{-1} under a low-temperature condition of -18°C. As a result, the G2 organic solvent enables a stable Zn plating

/stripping and suppresses the dendrite growth and corrosion on the Zn surface, which illustrate a practical application and unprecedented strategy for the future of an aqueous zinc-ion battery.

3.3 Experimental section

3.3.1 Preparation of Iodine - Activated Carbon (I_2- AC) cathodes

Iodine was melted into activated carbon at 150 °C for 12h in a ratio of 30% iodine and 70% of activated carbon. Then the I_2- AC composite was mixed under magnetic stirring with Super P and sodium alginate in a weight ratio of 8:1:1. The slurry was drop coated onto stainless steel mesh and dried under infrared light. The mass loading of the active material (I_2- AC) was 1.44 mg/cm^2.

3.3.2 Electrolyte preparation

For the baseline test, the electrolyte used was 100 µL 2M $Zn(OTF)_2$ in DI water. For the experimental test, the electrolyte used was 100 µL 2M $Zn(OTF)_2$ in DI water and G2 solvent with a volume ratio of 3:1, 1:1, and 1:3.

3.3.3 Fabrication of batteries and electrochemical measurements

For the asymmetrical cell, the bare Cu foil was used as a working electrode and the bare Zn foil was used as a counter electrode with 100 µL electrolyte and glass fiber acting as the separator. For the symmetrical cell, first of all, bare zinc foils and copper foils served as electrodes with electrolytes to assemble the Zn//Cu cell to get thin Zn plating on copper foils. Each Zn//Cu cell run under conditions of 3 mA cm^{-2} and 3 mAh cm^{-2}. Then two thin Zn that was plated on the copper foils served as electrodes to assemble the Zn symmetric cell. The full cell was assembled with bare Zn anode and I-AC cathodes. All the cells were assembled into CR2032 coin cells in the air

atmosphere. For the low-temperature test, assembled coin cells were placed inside a freezer. The 2D/3D diffusion curves were measured by the chronoamperometry (CA) method under a constant voltage of -150 mV over 120s. Cyclic voltammetry (CV) was tested with Zn//Cu asymmetrical cell and Zn//I_2- AC full cell. EIS testing was performed with Zn//I_2- AC full cell. All the CA, CV, and EIS tests were carried out on the BioLogic electrochemical workstation. Galvanostatic charge-discharge tests of asymmetrical cells, symmetrical cells, and full cells were tested on the Neware battery testing system.

3.3.4 Characterization

X-ray Diffraction (XRD) measurement was presented on an Ultima IV (Rigaku) diffractometer equipped with a Cu Kα X-ray source. Scanning electron microscope (SEM, Zeiss EVO M10) was used to analyze the structure of nano-sized material. Raman spectra were obtained on a Raman spectrometer (Renishaw inVia Qontor) equipped with a laser wavelength of 532 nm. The X-ray photoelectron spectrometer (XPS) was performed on Kratos AXIS Ultra. H Nuclear magnetic resonance spectrum (NMR) was conducted on Bruker AVANCE III.

3.3.5 Theoretical calculation

Molecular Dynamic (MD) simulations were performed using Materials Studio. The model of water molecules, G2 molecules, and OTF^- ions were built separately. For each built model, the charge distribution of each atom was assigned manually. The charge distribution of each atom was calculated by using Multiwfn. First of all, an amorphous cell was assigned 50 Zn^{2+} ions, 100 OTF^- ions, 1040 water molecules, and 44 G2 molecules. After the amorphous cell was successfully created, the forcite model was used to calculate the dynamics of the structure. The ensemble used was NPT in which the temperature was assigned to 298K, the pressure was assigned to 0.0001

GPa and the total simulation time was assigned to 200 ps. Berendsen was used as the barostat. The radial distribution functions (RDFs) were analyzed by using forcite analysis in the Materials Studio. The RDFs were used to analyze the distance between the oxygen atom and Zn^{2+} ions. The coordination number of water molecules, G2 molecules, and OTF^- ions that surround Zn^{2+} ions was calculated by the following formula: $N(r') = 4\pi\frac{N}{V}\int_0^{r'} g(r)r^2dr$. Density functional theory (DFT) calculation was performed to optimize the structure and calculate the binding energy. Gaussview and Gaussian09 were used to create structure and perform calculations. B3LYP with 6-311G was set up in the DFT calculation. The binding energies were obtained by the following equation: $E_b=(E_{Zn}+E_{G2})-E_{Zn+G2}$. Absorption energy was calculated by using the Vienna Ab-initio Simulation Package (VASP) kit. The Zn (002) surface was chosen to build a 5x5 supercell, a vacuum slab with a thickness of 10Å was added to the supercell and the atoms on the last two layers were fixed. The cut-off energy was set as 500eV, the total energy was set as 10^{-6}eV and the atomic force was set as 0.01 eV/Å. The projector augmented wave method (PAW), the generalized gradient approximation (GGA) and the Perdew-Burke-Ernzerhof (PBE) method were selected to calculate the energy. The K point was generated by the gamma point method from the VASP kit. The absorption energy was calculated by the following equation: $E_{ab}=E_{Zn+G2}-(E_{Zn}+E_{G2})$.

3.4 Results and discussion

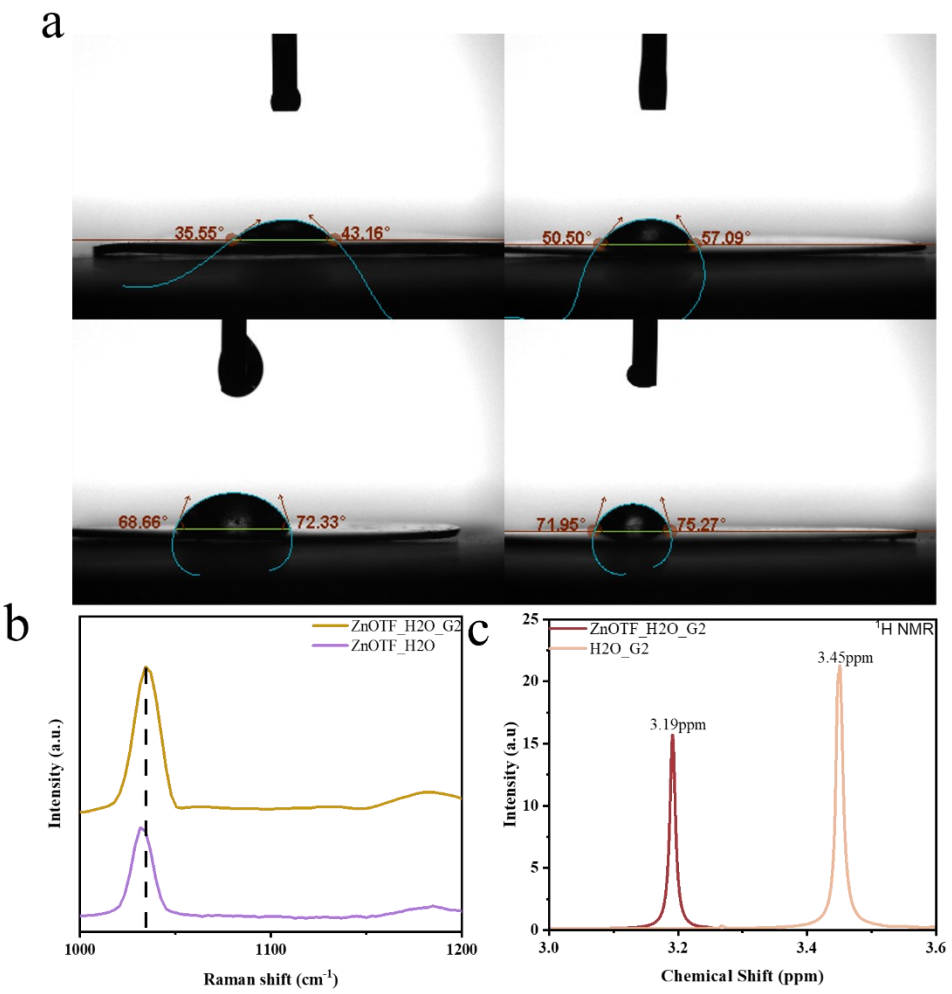

Figure 20. (a) Contact angle measurements of Top left: $H_2O(3)$ - G2(1), Top right: $H_2O(1)$ - G2(1), Bottom left: $H_2O(1)$ - G2(3), Bottom right: bare electrolyte on the Zn electrode. (b) Raman spectroscopy for baseline $Zn(OTF)_2$ electrolyte and $H_2O(3)$ - G2(1) electrolyte. (c) ^1H NMR spectra for baseline $Zn(OTF)_2$ electrolyte and $H_2O(3)$ - G2(1) electrolyte.

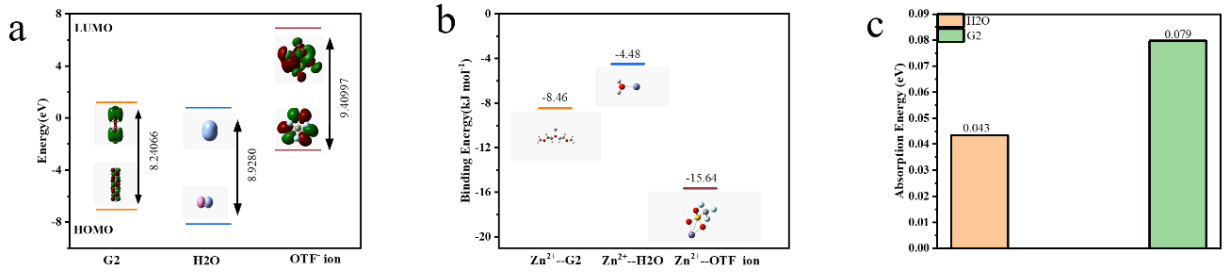

Figure 21. (a) HOMO and LUMO energy levels of Zn-G2, Zn- H_2O, and Zn-OTF^-. (b)Binding Energy of Zn (0 0 2) plane for baseline $Zn(OTF)_2$ electrolyte and $H_2O(3)$ - G2(1) electrolyte. (c) Absorption Energy of Zn (0 0 2) plane for baseline $Zn(OTF)_2$ electrolyte and $H_2O(3)$ - G2(1) electrolyte.

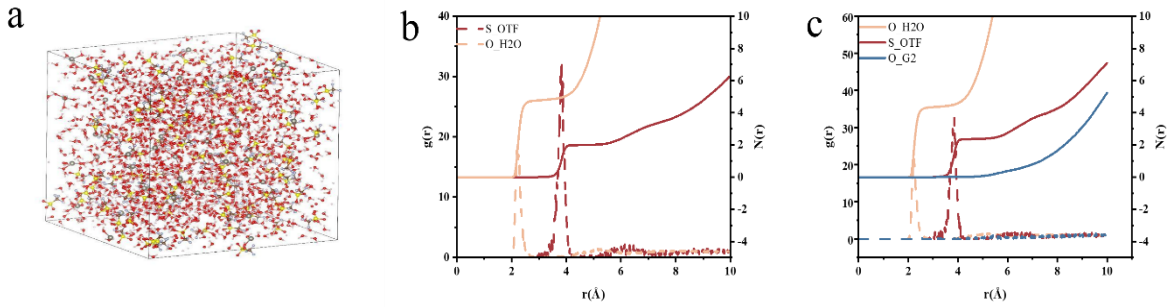

Figure 22. (a) MD amorphous cell for $H_2O(3)$ - G2(1) electrolyte. (b) RDFs and coordination number for baseline $Zn(OTF)_2$ electrolyte. (c) RDFs and coordination number for $H_2O(3)$ - G2(1) electrolyte.

G2 as an organic solvent in the electrolyte can reconstruct the solvation structure and form an inorganic SEI layer on the Zn surface. To determine its function, several samples of electrolytes were prepared in the following: 2M $Zn(OTF)_2$ dissolved in H_2O and G2 solvent with a ratio of 3:1 (denoted as $H_2O(3)$ - G2(1) electrolyte), 2M $Zn(OTF)_2$ dissolved in H_2O and G2 solvent with a ratio of 1:1 (denoted as $H_2O(1)$ - G2(1) electrolyte), 2M $Zn(OTF)_2$ dissolved in H_2O and G2 solvent with a ratio of 1:3 (denoted as $H_2O(1)$ - G2(3) electrolyte) and 2M $Zn(OTF)_2$ dissolved in H_2O solvent. Various theoretical calculations and experimental analyses were utilized to gain an

in-depth understanding of G2 in this co-solvent electrolyte system. In Fig. 20a, the contact angle of the baseline electrolyte and experimental electrolyte were measured to test the wettability. The contact angle is measured by dropping the electrolyte on the Zn electrode. In general, a contact angle of greater than 90°C is considered as hydrophobic and a contact angle of less than 90°C is considered as hydrophilic. The baseline $Zn(OTF)_2$ electrolyte without the G2 solvent has the largest contact angle. With the addition of G2 solvent, the contact angle is getting smaller and the $H_2O(3)$ - G2(1) electrolyte has the smallest contact angle. This result reveals that better wettability is approached with the addition of G2 solvent, which leads to better absorption of G2 on the interface(78).

Raman spectroscopy in the range from 1000 cm^{-1} to 1100 cm^{-1} is shown in Fig. 20b. The peak corresponding to OTF^- ions(69) has slightly shifted to a higher frequency in the $H_2O(3)$ - G2(1) electrolyte. This result indicates the increased number of OTF^- ions in the solvation structure, which proves that the G2 solvent changes the solvation structure by replacing water molecules with OTF^- ions. The ^1H NMR spectra of the G2 solvent show a peak at 3.45ppm which belongs to the $O\text{-}CH_3$ group (Fig. 20c). While adding the G2 solvent into $Zn(OTF)_2$ electrolyte, the ^1H NMR spectra show a downfield chemical shift from 3.45ppm to 3.19ppm. This result reveals that Zn^{2+} doesn't interact with the G2 solvent and the G2 solvent doesn't participate in the $[Zn(H_2O)_6]^{2+}$ solvation sheath. The OTF^- ion is more favorable to interact with the Zn^{2+} cation than the G2 solvent.

To study and analyze the properties and behavior of molecules and ions in the electrolyte, density functional theory (DFT) calculation was performed to calculate the highest occupied molecular orbital (HOMO), lowest unoccupied molecular orbital (LUMO), the binding energy of each molecule and ions against Zn^{2+} and absorption energy on the Zn (0 0 2) plane. As shown in Fig. 21a, the HOMO and LUMO energy levels of G2 molecules, water molecules, and OTF^- ions are analyzed against Zn^{2+}. The HOMO level of Zn-G2 (-7.02eV) and Zn-OTF^- (-2.48eV) are higher than Zn-H_2O (-8.15eV). This proves that the G2 molecule is easier to lose electrons when absorbing on the Zn surface than water molecules. Moreover, the energy gap between the HOMO

and LUMO levels of Zn-G2 (8.24eV) is the smallest compared to Zn-H_2O (8.93eV) and Zn-OTF^- (9.41eV). This reveals that chemical reactions are easier to happen on the Zn surface with the addition of G2 molecules. The binding energy of Zn^{2+}-OTF^- (-15.64 eV) is much larger than Zn^{2+}-G2 (-8.46 eV) and Zn^{2+}-H_2O (-4.48 eV)(114), showing that Zn^{2+} prefers to interact with OTF^- ions rather than interact with G2 molecules in the solution (Fig.21b). The OTF^- ions have a better preference of entering the solvation structure than the G2 molecule. Furthermore, the absorption energy of the G2 molecule and water molecule on the Zn (002) plane were calculated (Fig.21c). The G2 molecule has a larger absorption energy (0.079 eV) than the water molecule (0.043 eV), which indicates that the G2 molecule can help with a better Zn deposition and suppress dendrite growth on the Zn surface(78).

Molecular dynamics (MD) simulations were performed to analyze the solvation structure of the electrolytes with and without the addition of G2 solvent. As shown in Fig. 22a, G2 solvent is added to the system. There are multiple water molecules and OTF^- ions surrounding the Zn^{2+} ions. However, most of the G2 molecules are displayed far away from the Zn^{2+} ions, which indicates that the G2 molecule doesn't enter the Zn^{2+} solvation shell. The Zn^{2+} solvation shell only consists of water molecules and OTF^- ions, which the number of water molecules is larger than the number of OTF^- ions. The radial distribution function (RDFs) and coordination number were analyzed and calculated to study the distribution of neighbor molecules and ions in the Zn^{2+} solvation shell. As presented in Fig. 22b, without the addition of G2 solvent, the peak of the Zn-O_H_2O pair displays at 2.1Å and the peak of Zn-S_OTF^- displays at 3.9Å. The length of the S-O bond in OTF^- ions is around 1.5Å, therefore, the distance distribution of the Zn-O_OTF^- pair is nearly close to the distance distribution of the Zn-O_H_2O pair. The coordination number of the Zn-O_H_2O pair is 4.8 and the coordination number of Zn-S_OTF^- is 2.0, which presents a solvation structure that has four or five dipolar water molecules and two OTF^- ions coordinating with one Zn^{2+} cation. By comparison, after the addition of G2 solvent, the peak distribution of the Zn-O_H_2O pair and Zn-S_OTF^- pair doesn't change (Fig. 22c). However, the coordination number of Zn-O_H_2O pair decreases to 4.36, the coordination number of Zn-S_OTF^- increases to 2.38 and the coordination

number of Zn-O_G2 is 0.10. The addition of G2 solvent reconstructs the solvation structure by allowing more OTF^- ions to replace the water molecules. The mechanism of G2 solvent in the $Zn(OTF)_2$ electrolyte system is that G2 solvent allows more OTF^- ions to participate in the Zn^{2+} solvation structure. The $Zn(OTF)_2$ salts don't dissolve in the G2 solvent, more water molecules are used to dissolve the G2 solvent and the G2 solvent repels OTF^- ion in this system. Therefore, the G2 solvent stays far away from the Zn^{2+} cation, and the repelled OTF^- ion is capable of entering the solvation structure and replacing the missing water molecule. Further MD simulation for an increasing volume of G2 in the electrolyte (H_2O(1) - G2(1)) also shows the same conclusion, where the coordination number of Zn-O_H_2O is 4.20, the coordination number of Zn-S_OTF^- is 2.35 and the coordination number of Zn-O_G2 is 0.01 (Fig. 23).

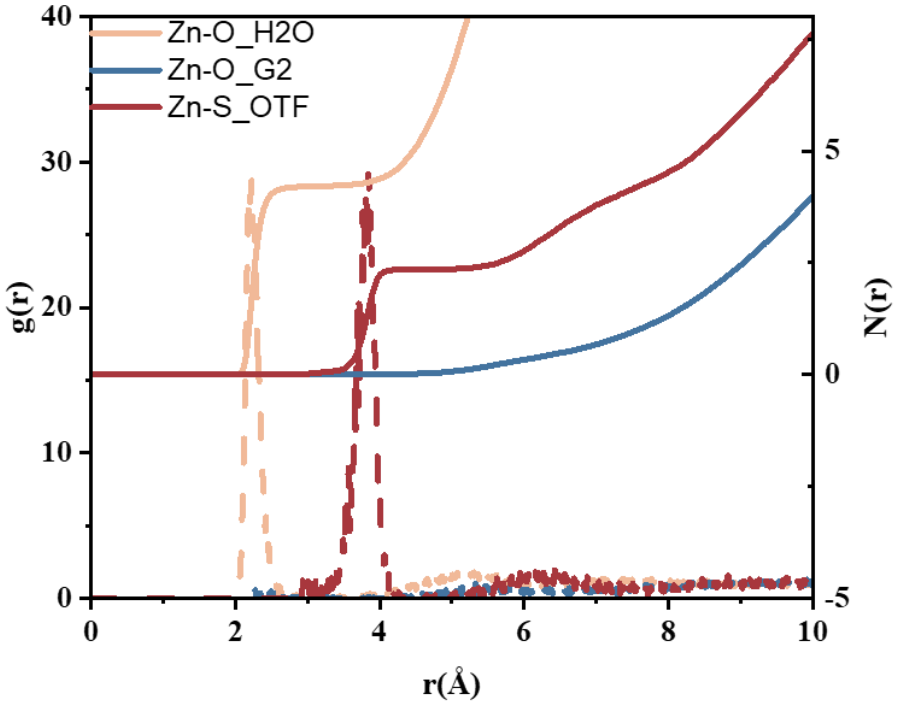

Figure 23. RDFs and coordination number for H_2O(1) - G2(1) electrolyte.

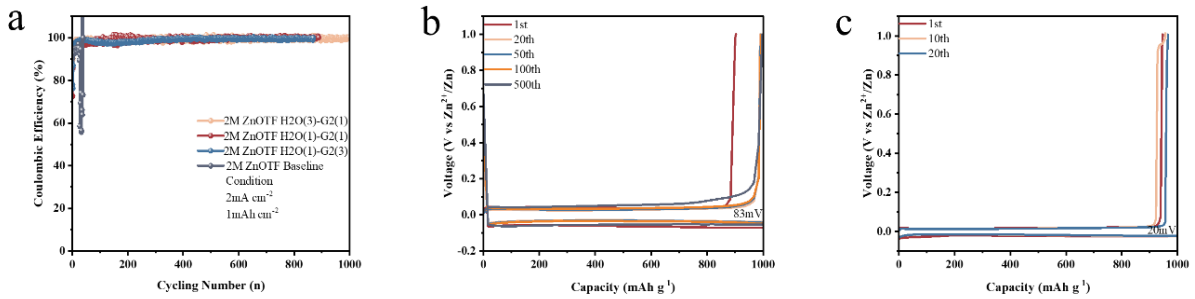

Figure 24. (a) Coulombic efficiency (CE) of Zn//Cu asymmetric cells with and without different volume ratios of G2 in the electrolyte. (b) Voltage profiles of asymmetric cell with $H_2O(3)$ - G2(1) electrolyte. (c) Voltage profiles of asymmetric cells without G2.

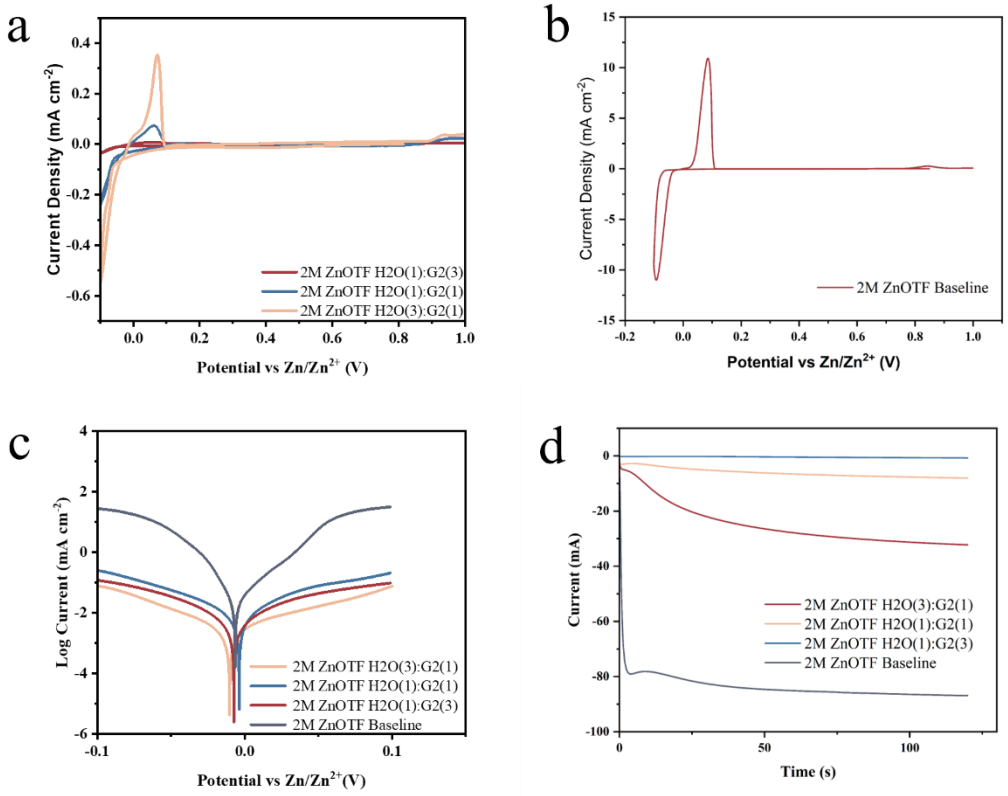

Figure 25. (a) Cyclic voltammetry (CV) with different volume ratios of G2 in the electrolyte. (b) Cyclic voltammetry (CV) of baseline $Zn(OTF)_2$ electrolyte. (c) Linear polarization curve of electrolyte with and without different volume ratios of G2. (d) Chronoamperometry (CA) with different volume ratios of G2 in the electrolyte.

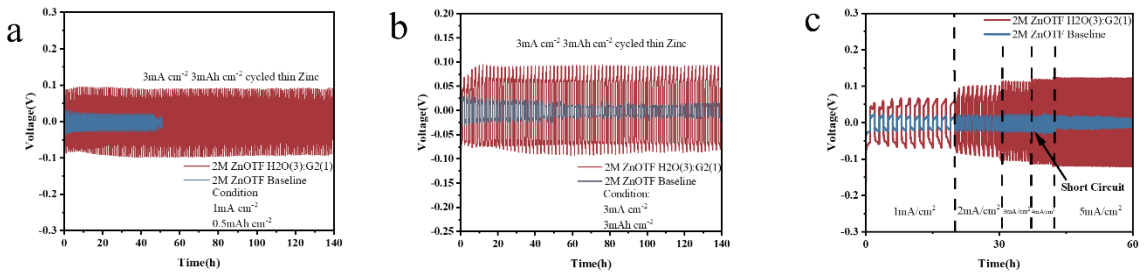

Figure 26. (a) Cycling performance of symmetric cells at 1 mA cm^{-2} and 0.5 mAh cm^{-2} with $H_2O(3)$ - G2(1) electrolyte and baseline $Zn(OTF)_2$ electrolyte. (b) Cycling performance of symmetric cells at 3 mA cm^{-2} and 3 mAh cm^{-2} with $H_2O(3)$ - G2(1) electrolyte and baseline $Zn(OTF)_2$ electrolyte. (c) Cycling rate performance of symmetric cells.

To examine the effect of the G2 molecule on smoothing Zn deposition and restricted dendrite growth, a Zn//Cu asymmetric cell was first assembled to analyze the stability. In Fig. 24a, the baseline $Zn(OTF)_2$ electrolyte has an average CE of 95% for a short 47 cycles and then becomes unstable. For the $H_2O(3)$ - G2(1), $H_2O(1)$ - G2(1) and $H_2O(1)$ - G2(3) electrolytes, the cells all show stable and high CEs of 99.7% for more than 900 cycles, which lead to the high reversibility of Zn plating and stripping. Furthermore, a stable charge and discharge curve of the Zn//Cu asymmetric cell after different cycles were obtained, with a small acceptable voltage polarization of 83mV (Fig. 24b) and a voltage polarization of 20mV (Fig. 24c). To further examine the protection on the Zn surface, cyclic voltammetry (CV) was tested and shown in Fig. 25a. Before the nucleation of Zn on the copper surface, there is already a drop of current density that appears at an overpotential of 0.1V. This indicates that there is an interfacial reaction that happened before Zn^{2+} plating on the copper foil, which is the formation of an inorganic SEI layer on the surface. The $H_2O(3)$ - G2(1) electrolyte has the largest current density, and the current density decreases as the volume of the G2 solvent increases. This is because the viscosity of the electrolyte increases as the addition of G2 solvent increases. The $H_2O(3)$ - G2(1) electrolyte has the best Zn^{2+} diffusion and plating kinetic among all the above G2-added electrolytes. The CV curve of the electrolyte without G2 doesn't present any current drop before Zn nucleation (Fig. 25b).

Since reactions occurred on the CV curve, surface corrosion needed to be analyzed by performing a Tafel plot (Fig. 25c). The corrosion current decreases with the addition of G2 solvent and the $H_2O(3)$ - G2(1) electrolyte has the smallest corrosion current. This result further proves that the Zn surface was protected after the G2 solvent was added to the electrolyte due to the formation of the SEI layer. The 2D and 3D diffusion is also tested from chronoamperometry (CA) and it shows a better diffusion as the volume of G2 solvent increases (Fig. 25d). Suppression of Zn dendrite growth was further evaluated by assembling and testing symmetric cells with and without the G2 solvent. To erase the factor of nearly unlimited zinc in the symmetric cell, the zinc foil was first assembled in a Zn//Cu asymmetric cell at 3 mA cm^{-2} and 3 mAh cm^{-2}. Then the thin zinc foil was collected and used to assemble symmetric cells. In Fig. 26a, the cell of baseline $Zn(OTF)_2$ electrolyte cycled for only 50h at 1 mA cm^{-2} and 0.5 mAh cm^{-2}, which indicates uneven Zn deposition and growth of Zn dendrite. In comparison, the cell of $H_2O(3)$ - G2(1) electrolyte performed a longer cycling life of 140h. At a high current density of 3 mA cm^{-2} and capacity of 3 mAh cm^{-2}, the symmetric cell with G2 solvent shows better cycling hours of 140h than the baseline $Zn(OTF)_2$ electrolyte (Fig. 26b). Moreover, the symmetric cells at different current density were tested and the cell of $H_2O(3)$ - G2(1) electrolyte has the better rate performance compared to the baseline $Zn(OTF)_2$ electrolyte (Fig. 26c). Short circuit appeared at the current density of 4 mA cm^{-2} for the cell without G2 solvent while a stable voltage fluctuation was obtained with G2 solvent.

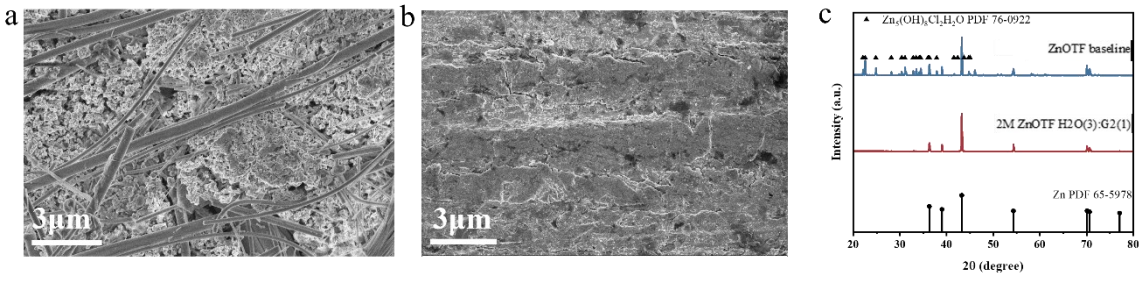

Figure 27. (a) SEM image of cycled Zn electrode without G2. (b) SEM image of cycled Zn electrode with $H_2O(3)$ - G2(1). (c) XRD of cycled Zn electrode with and without G2.

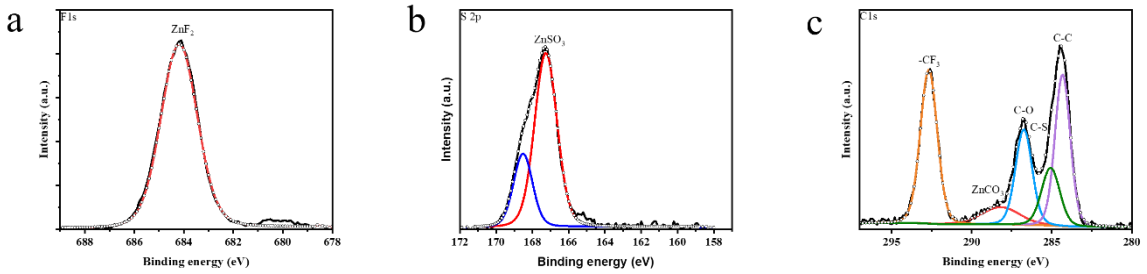

Figure 28. (a) XPS of F 1s spectra with G2. (c) XPS of S 2p spectra with G2. (c) XPS of C 1s spectra with G2.

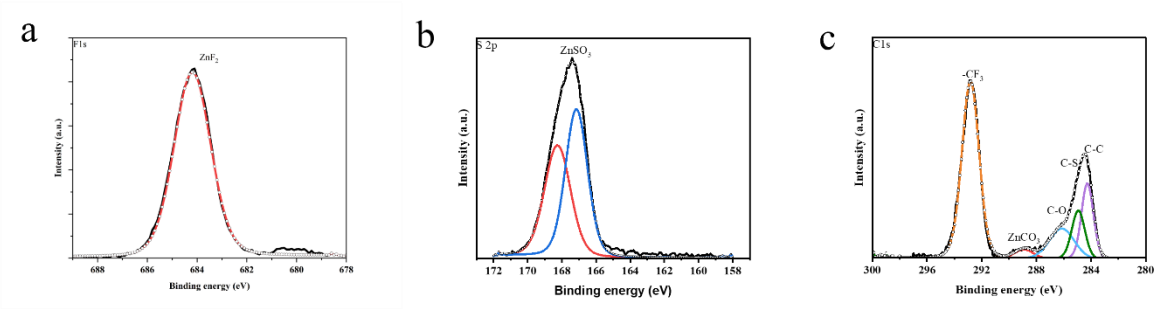

Figure 29. (a) XPS of F 1s spectra without G2. (c) XPS of S 2p spectra without G2. (c) XPS of C 1s spectra without G2.

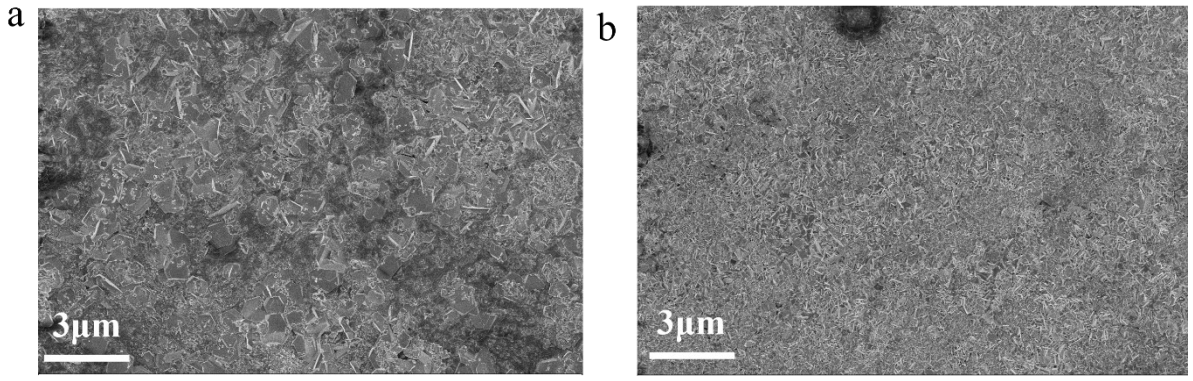

Figure 30. (a) SEM image of Zn foil soaked in H_2O(3) - G2(1) electrolyte. (b) SEM image of Zn foil soaked in baseline $Zn(OTF)_2$ electrolyte.

Then the possible composition of the SEI layer and zinc surface protection is found by taking SEM, XRD, and XPS. The Zn deposition was first investigated by taking SEM on two Zn electrodes that

were cycled for 100h. In Fig. 27a, without the G2 solvent, cracks and serious amounts of Zn dendrite growth, which are caused by uneven Zn^{2+} depositions were observed. In comparison, a much smoother Zn surface with uniform Zn^{2+} deposition is observed with G2 solvent (Fig. 27b). The corresponding XRD is performed to find out whether there is a by-product forming on the surface. In Fig. 27c, the XRD shows that a by-product of $Zn_5(OH)_8Cl_2H_2O$ is formed on the Zn surface, which the OH^- is from the hydrogen evolution reaction. While with the addition of G2 solvent, the XRD shows only the Zn peak, and no by-product peak is found.

Then the composition of the SEI layer was investigated from XPS. For the H_2O(3) - G2(1) electrolyte, F 1s spectra illustrate an inorganic component of ZnF_2 at 684.19 eV (Fig. 28a), which is a reported peak from other articles(88, 90, 115). The F^- comes from the reduction of the OTF^- ion. S 2p spectra demonstrate an inorganic component of $ZnSO_3$ at 167eV (Fig. 28b)(115). These two inorganic components come from the decomposition of OTF on the surface. C 1s spectra present multiple organic components of C-C (284.3 eV), C-O (286.7 eV), C-S (285.0 eV), CF_3 (292.7 eV), and an inorganic component of $ZnCO_3$ (288.2 eV) (Fig. 28c)(90, 115). In comparison, the F 1s spectra and S 2p spectra show a similar trend without the G2 solvent (Fig. 29a-b). The C 1s spectra present the same organic and inorganic components except the intensity of $ZnCO_3$ is weaker without G2 solvent (Fig. 29c). The decomposition and reduction of $Zn(OTF)_2$ produces CF_3^- and OH^-, which further react with the CO_2 from air and forms CO_3^{2-}. Additionally, the G2 solvent reacts with Zn on the surface and forms $ZnCO_3$. The organic and inorganic (ZnF_2-$ZnCO_3$-$ZnSO_3$) hybrid SEI layer suppresses the self-corrosion and dendrite growth on the surface and promotes uniform Zn deposition.

To further examine the protective layer on resisting corrosion, the Zn foils were soaked in the electrolyte with and without the G2 solvent. The SEM image shows a large number of flakes ($ZnOTF_x(OH)_y.nH_2O$) on the Zn surface without G2 solvent (Fig. 30a)(87). The bare Zn foil is not capable to suppress the hydrogen evolution reaction along with the reduction of Zn and $Zn(OTF)_2$, which only leads to serious corrosion on the surface. By adding the G2 solvent to the electrolyte, the by-product significantly decreases (Fig.30b), which successfully stops the continuous free

water molecule from penetrating the surface and promotes irreversible corrosion.

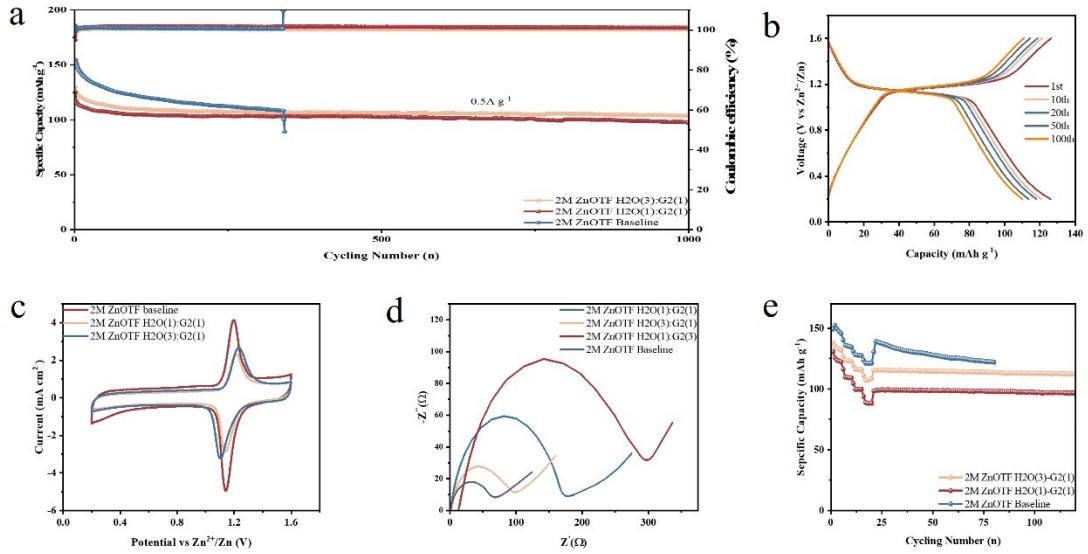

Figure 31. (a) Long-term cycling performance of full cell coupled with I_2- AC cathode at 0.5 A g^{-1}. (b) Charge and discharge profile at different cycles. (c) CV profile of Zn//I_2- AC full cell. (d) EIS of Zn//I_2- AC full cell. (e) Rate performance of Zn//I_2- AC full cell.

The potential full cell application of Zn anode coupled with Iodine-Activated Carbon (I_2- AC) cathode was investigated. In Fig. 31a, the cell of $Zn(OTF)_2$ electrolyte has an initial discharge specific capacity of 152 mAh g^{-1} at the current density of 0.5 A g^{-1} and fails at 338 cycles. After the addition of G2 solvent, the cell of $H_2O(3)$ - G2(1) electrolyte has an initial capacity of 129 mAh g^{-1} and a capacity retention of 80% for 1000 cycles. The cell of $H_2O(1)$ - G2(1) electrolyte has an initial capacity of 125 mAh g^{-1} and a capacity retention of 78.4% for 1000 cycles. Significant improvement in long-term cycling stability is achieved. The charge and discharge curve for the full cell of $H_2O(3)$ - G2(1) electrolyte is shown in Fig. 31b, which shows a stable Zn plating and stripping in a wide voltage window from 0.2V to 1.6V. The full cell CV curve shows a decreased current density for $Zn(OTF)_2$ electrolytes with the addition of G2 solvent. The suppressed current density leads to a more uniform Zn deposition on the surface (Fig. 31c). The EIS plot shows an increase of impedance with an increase of G2 solvent in the electrolyte (Fig. 31d). This is because the addition of G2 solvent increases the viscosity of the electrolyte. In Fig.

31e, as the volume of the G2 solvent decreases, the higher discharge capacity is obtained from the full cell rate performance test at the current density from 0.5 A g^{-1} to 2 A g^{-1}. The result indicates that the G2 solvent doesn't affect the I_2- AC cathode and only has the improvement of Zn deposition on the Zn anode.

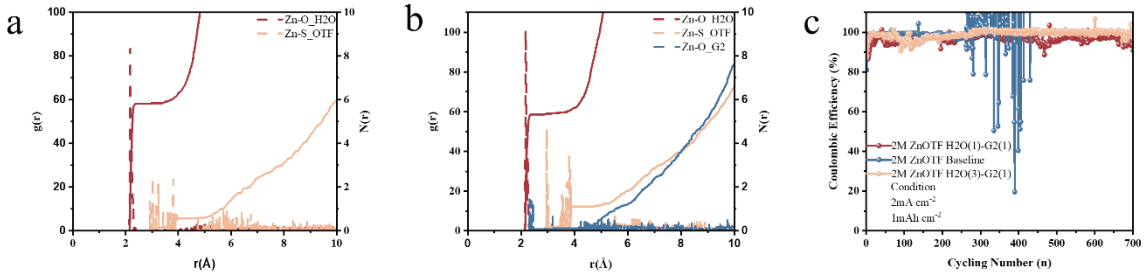

Figure 32. (a) RDFs and coordination number for baseline $Zn(OTF)_2$ electrolyte. (b) RDFs and coordination number for $H_2O(3)$ - G2(1) electrolyte. (c) Coulombic efficiency (CE) of Zn//Zn asymmetric cells with and without G2.

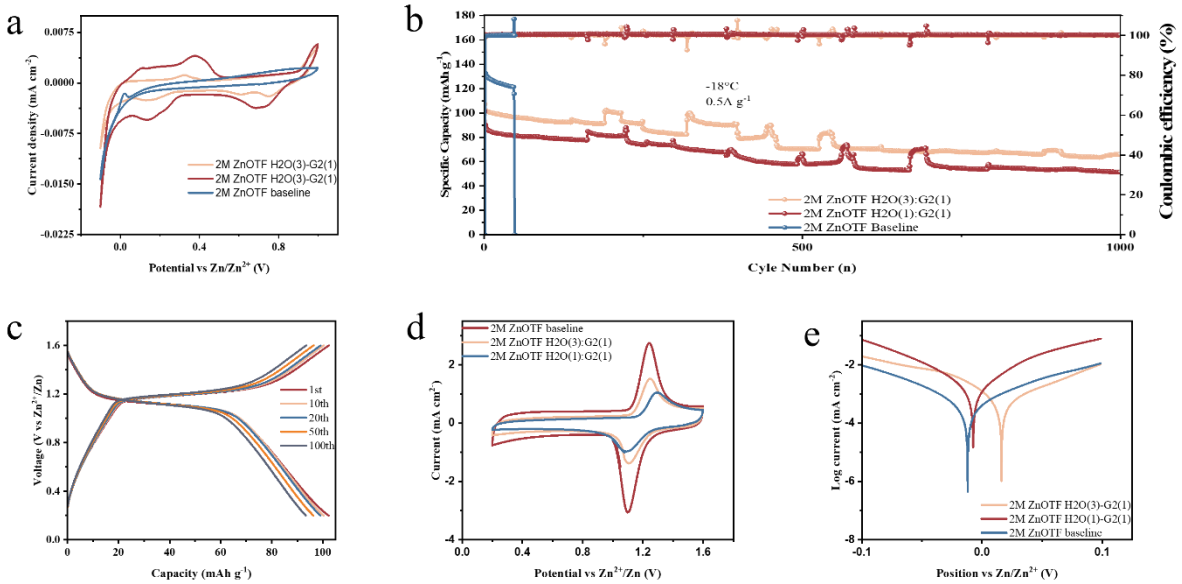

Figure 33. (a) Cyclic voltammetry (CV) with and without G2 in the electrolyte. (b) Long-term cycling performance of Zn// I_2- AC full cell at 0.5 A g^{-1}. (c) Charge and discharge profile at different cycles. (d) CV profile of Zn//I_2- AC full cell. (e) Linear polarization curve of with and without G2.

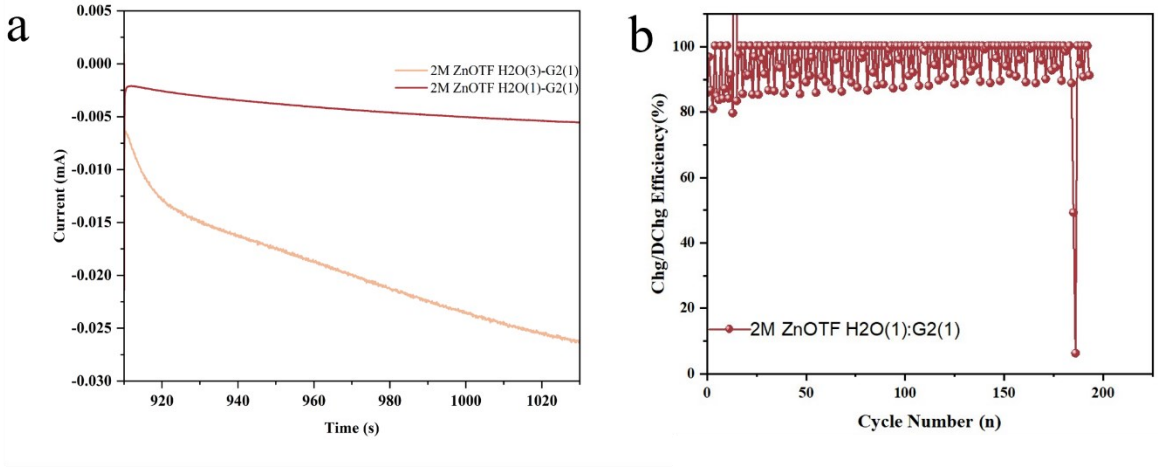

Figure 34. (a) Chronoamperometry (CA) with different volume ratios of G2 in the electrolyte. (b) Coulombic efficiency (CE) of Zn//Cu asymmetric cells in $H_2O(1)$ - G2(1) electrolyte at 40°C.

The impact of G2 solvent was further investigated at a low-temperature condition. MD simulations were again performed at a temperature of -18°C to analyze the function of the G2 molecule in the Zn^{2+} Solvation structure. Without the addition of G2 solvent (Fig. 32a), the coordination number of the Zn-O_H_2O pair is 5.83 and the coordination number of the Zn-S_OTF^- pair is 0.16. In Fig. 32b, with the addition of G2 solvent, the coordination number of Zn-O_H_2O pair decreases to 5.33, the coordination number of Zn-S_OTF^- increases to 1.10 and the coordination number of Zn-O_G2 is 0.11. These results reveal that the addition of G2 solvent in the electrolyte still can reconstruct the solvation structure at a low temperature. G2 has a low melting point of -64 °C and water has a melting point of 0 °C. While G2 is dissolved in water, the melting point of the mixed solution will be intermediate and the solution will retain a liquid state at -18°C. Similar to the simulation at room temperature, the G2 molecule is still capable to repel OTF^- ions and allowing more OTF^- ions to take place in the water molecule around Zn^{2+} cation in the solvation sheath.

Zn//Cu asymmetric cell was assembled and tested at 2 mA cm^{-2} and 1 mAh cm^{-2}. As presented in Fig. 32c, the cell of baseline $Zn(OTF)_2$ electrolyte has an average CE of 98.2% for a short 300 cycles and then becomes unstable. The $H_2O(3)$ - G2(1) electrolyte has an initial CE of 93% for the first 150 cycles and then the CE increases to 99.5% for 700 cycles. An average CE of 93% for 700

cycles was obtained for the H_2O(1) - G2(1) electrolyte. The addition of G2 solvent results in great stability which indicates a smooth Zn deposition. CV curve was tested to examine the diffusion kinetic and a significant decrease of current density was obtained for the baseline $Zn(OTF)_2$ electrolyte compared in the room temperature CV curve(Fig. 33a). Both the H_2O(3) - G2(1) electrolyte and the H_2O(1) - G2(1) electrolyte have larger current density, which indicates that the G2 added electrolyte has better diffusion and interfacial electrochemical reaction kinetics at low temperature. The Zn//I_2- AC full cell was assembled and put in a small freezer to test the long-term cycling performance at the current density of 0.5 A g^{-1} (Fig.33b). The full cell with baseline $Zn(OTF)_2$ electrolyte presents a discharge specific capacity of 120 $mAh\ g^{-1}$ and quickly die at 47 cycles. For the H_2O(3) - G2(1) electrolyte, the full cell delivers an initial discharge specific capacity of 107 mAh g^{-1} and a capacity retention of 65% for 1000 cycles. For the H_2O(1) - G2(1) electrolyte, the full cell delivers an initial discharge specific capacity of 102 mAh g^{-1} and a capacity retention of 53% for 1000 cycles. The tested temperature in the freezer can't be maintained at exactly -18°C due to uncontrollable action, therefore, the discharge specific capacity varies up and down occasionally. The baseline $Zn(OTF)_2$ electrolyte suffers from poor diffusion and reaction kinetic while the full cells with the addition of G2 solvent show better stability.

The charge and discharge curve for the full cell of H_2O(3) - G2(1) electrolyte is shown in Fig. 33c. The curve shows a stable Zn plating and stripping in a wide voltage window from 0.2V to 1.6V. The full cell CV curve shows a lower current density with the G2 solvent, which reveals that a suppressed current density is obtained, and this allows uniform Zn deposition (Fig.33d). Tafel curve was also tested (Fig. 33e) and H_2O(3) - G2(1) electrolyte has the largest corrosion potential (0.015V) compare with the H_2O(1) - G2(1) electrolyte (-0.007V) and the baseline $Zn(OTF)_2$ electrolyte (-0.017V). The more negative the potential, the greater the potential difference between the anode and the cathode, which leads to a greater thermodynamic trend of the reaction. The more positive potential from the G2-added electrolyte indicates a possible slow self-corrosion. The 2D and 3D diffusion is also tested from chronoamperometry (CA) and it shows a better diffusion as the volume of G2 solvent increases (Fig. 34a). Furthermore, an asymmetric cell is tested at an even

lower temperature of -40°C(Fig. 34b). The CE is varying from 100% to 80% in the period. Therefore, we analyzed that the G2 solvent can enhance the cycling stability in the zinc-ion battery system.

3.5 Conclusion

In summary, the organic solvent of G2 is analyzed and formulated with $Zn(OTF)_2$ electrolyte for uniform Zn deposition and a better suppression of Zn dendrite growth. The theoretical calculation, Raman spectra, and ^1H NMR revealed that the G2 solvent allows more OTF^- ions to participate in the Zn^{2+} Solvation structure and coordinate with Zn^{2+}. Water molecule from the $[Zn(H_2O)_6]^{2+}$ is replaced and results in a better Zn desolvation. The CV curve and XPS spectra indicate the formation of the SEI layer on the Zn surface. The organic and inorganic (ZnF_2-$ZnCO_3$- $ZnSO_3$) layer was formed due to the decomposition and reduction of G2 and OTF^- ions. This SEI layer helps uniform Zn deposition, suppress dendrite growth and resist self-corrosion on the Zn surface. A high CE of 99.7% was observed. Cycling life of 140h for limited Zn foil at 1 mA cm^{-2} and 0.5 mAh cm^{-2} was obtained. The full cell coupled with I_2- AC has capacity of 107 mAh g^{-1} and capacity retention of 80% for a long and stable cycling life of 1000 cycles. These results show great reversibility of Zn plating and stripping. Besides, the theoretical calculation and experimental results at a low temperature of -18°C were obtained and G2 solvent functions at such temperature. Therefore, the application of G2 solvent with $Zn(OTF)_2$ electrolyte is considered a practical strategy to improve and protect the Zn anode.

Chapter 4 Conclusion and Future Work

Aqueous zinc-ion batteries have been considered a promising energy storage system for increasing demand of efficient and sustainable development due to the advantages of low cost, high safety, and environmentally friendly. Even though the Zn anode still suffers from the growth of Zn dendrite and parasite side reactions, the strategy of electrolyte engineering has been well-analyzed and used to address these problems. The electrolyte is the medium that connects the anode and cathode and allows ions to transfer. By adjusting the electrolyte, several parameters including the ionic conductivity, Zn^{2+} solvation structure, interfacial reaction, and decomposition are affected, which are related to the Zn^{+2} diffusion and uniform Zn^{2+} deposition. This results in high CE and excellent cycling stability for the battery.

In Chapter 1, a brief literature review that collects the recent progress of electrolyte engineering in zinc-ion batteries is prepared. Five types of electrolyte modification (highly concentrated electrolyte, organic solvent, metal-ion additive, SEI forming additive, and surfactant) are analyzed from both theoretical calculation and experimental data. The mechanism of solvation structure manipulation and SEI layer formation for each material is discussed in detail.

In Chapter 2, the methodology and the corresponding characterization technique for analyzing the solvation structure, Zn surface protection and SEI layer are outlined.

In Chapter 3, a complete research project of G2 organic solvent enabling stable zinc ion battery is demonstrated. The theoretical simulation and calculation reveal that G2 solvent can repel OTF^- anions in the electrolyte and allows more OTF^- anions to enter the solvation structure and replace the water molecules. This reduces the energy barrier for Zn desolvation and inhibits water decomposition, which further inhibits the hydrogen evolution reaction. The XPS spectra of cycled Zn electrode show the formation of organic and inorganic (ZnF_2-$ZnCO_3$- $ZnSO_3$) layer on the Zn surface, which allows uniform Zn^{2+} deposition. The asymmetric cell shows a high CE of 99.7% from 1000 cycles. The symmetric cell shows better cycling stability for 140h. The full cell shows excellent long cycling stability of 1000 cycles. Furthermore, the G2 organic solvent expands the

operating temperature to -18°C. The theoretical simulation shows the same mechanism as at room temperature.

This research shows a unique perspective on the organic solvent used in the electrolyte. As discussed in Chapter 1, the organic molecules from high donor number organic solvents tend to enter the solvation structure and replace the water molecules. However, in my research, the G2 molecules don't enter the solvation structure even though the donor number of G2 is greater than water. G2 molecules are beneficial for OTF^- entering the solvation structure. The mechanism behind this phenomenon is very interesting. For future research, the relation and mechanism between different Zn-salts and organic solvents need to be further considered and analyzed. Furthermore, the viscosity of the electrolyte increases with the development of organic solvent. For future works, the research could focus on the adjustment of electrolyte viscosity by applying development of salt or additive.

References

1. Wang B, Xu H, Hao J, Du J, Wu C, Ma Z, et al. Mini-Review on the Regulation of Electrolyte Solvation Structure for Aqueous Zinc Ion Batteries. Batteries. 2023;9(2):73.

2. Cao J, Zhang D, Zhang X, Zeng Z, Qin J, Huang YJE, et al. Strategies of regulating Zn 2+ solvation structures for dendrite-free and side reaction-suppressed zinc-ion batteries. The Royal Society of Chemistry. 2022;15(2):499-528.

3. Du W, Ang EH, Yang Y, Zhang Y, Ye M, Li CCJE, et al. Challenges in the material and structural design of zinc anode towards high-performance aqueous zinc-ion batteries. Energy & Environmental Materials. 2020;13(10):3330-60.

4. Yan H, Zhang X, Yang Z, Xia M, Xu C, Liu Y, et al. Insight into the electrolyte strategies for aqueous zinc ion batteries. Coordination Chemistry Reviews. 2022;452:214297.

5. Guo S, Qin L, Zhang T, Zhou M, Zhou J, Fang G, et al. Fundamentals and perspectives of electrolyte additives for aqueous zinc-ion batteries. Energy Storage Materials. 2021;34:545-62.

6. Zhang Q, Yang Z, Ji H, Zeng X, Tang Y, Sun D, et al. Issues and rational design of aqueous electrolyte for Zn-ion batteries. SusMat. 2021;1(3):432-47.

7. Blanc LE, Kundu D, Nazar LFJJ. Scientific challenges for the implementation of Zn-ion batteries. Joule. 2020;4(4):771-99.

8. Geng Y, Pan L, Peng Z, Sun Z, Lin H, Mao C, et al. Electrolyte additive engineering for aqueous Zn ion batteries. Energy Storage Materials. 2022.

9. Shen Q, Wang Y, Han G, Li X, Yuan T, Sun H, et al. Recent Progress in Electrolyte Additives for Highly Reversible Zinc Anodes in Aqueous Zinc Batteries. Batteries. 2023;9(5):284.

10. Yuan L, Hao J, Kao C-C, Wu C, Liu H-K, Dou S-X, et al. Regulation methods for the Zn/electrolyte interphase

and the effectiveness evaluation in aqueous Zn-ion batteries. Energy & environmental Science. 2021;14(11):5669-89.

11. Liu S, Liu JJE, Materials E. Reshaping Electrolyte Solvation Structure for High-Energy Aqueous Batteries. Energy & Environmental Materials. 2022;5(3):686-7.

12. Yuan L, Hao J, Kao C-C, Wu C, Liu H-K, Dou S-X, et al. Regulation methods for the Zn/electrolyte interphase and the effectiveness evaluation in aqueous Zn-ion batteries. The Royal Society of Chemistry. 2021;14(11):5669-89.

13. Wang X, Li X, Fan H, Ma LJN-ML. Solid electrolyte interface in zn-based battery systems. Nano-Micro Letters. 2022;14(1):205.

14. Huang J, Guo Z, Ma Y, Bin D, Wang Y, Xia YJSM. Recent progress of rechargeable batteries using mild aqueous electrolytes. Small methods. 2019;3(1):1800272.

15. Mansfeld F, Gilman SJJotES. The effect of lead ions on the dissolution and deposition characteristics of a zinc single crystal in 6 N KOH. Journal of the electrochemical society. 1970;117(5):588.

16. Zhang N, Cheng F, Liu J, Wang L, Long X, Liu X, et al. Rechargeable aqueous zinc-manganese dioxide batteries with high energy and power densities. Nature Communications. 2017;8(1):405.

17. Tang X, Wang P, Bai M, Wang Z, Wang H, Zhang M, et al. Unveiling the reversibility and stability origin of the aqueous V2O5–Zn batteries with a ZnCl2 "water-in-salt" electrolyte. ADVANCED SCIENCE. 2021;8(23):2102053.

18. Patil N, de la Cruz C, Ciurduc D, Mavrandonakis A, Palma J, Marcilla RJAEM. An ultrahigh performance zinc-organic battery using poly (catechol) cathode in Zn (TFSI) 2-based concentrated aqueous electrolytes. ADVANCED ENERGY MATERIALS. 2021;11(26):2100939.

19. Zhang L, Liu Z, Wang G, Feng J, Ma QJN. Developing high voltage Zn (TFSI) 2/Pyr 14 TFSI/AN hybrid electrolyte for a carbon-based Zn-ion hybrid capacitor. The Royal Society of Chemistry. 2021;13(40):17068-76.

20. Suo L, Borodin O, Gao T, Olguin M, Ho J, Fan X, et al. "Water-in-salt" electrolyte enables high-voltage aqueous lithium-ion chemistries. Science. 2015;350(6263):938-43.

21. Jiang L, Liu L, Yue J, Zhang Q, Zhou A, Borodin O, et al. High-voltage aqueous Na-ion battery enabled by inert-cation-assisted water-in-salt electrolyte. ADVANCED MATERIALS. 2020;32(2):1904427.

22. Olbasa BW, Fenta FW, Chiu S-F, Tsai M-C, Huang C-J, Jote BA, et al. High-rate and long-cycle stability with a dendrite-free zinc anode in an aqueous Zn-ion battery using concentrated electrolytes. ACS Applied Energy Materials. 2020;3(5):4499-508.

23. Wang F, Borodin O, Gao T, Fan X, Sun W, Han F, et al. Highly reversible zinc metal anode for aqueous batteries. nature materials. 2018;17(6):543-9.

24. Zhang C, Holoubek J, Wu X, Daniyar A, Zhu L, Chen C, et al. A ZnCl 2 water-in-salt electrolyte for a reversible Zn metal anode. chemComm. 2018;54(100):14097-9.

25. Clarisza A, Bezabh HK, Jiang S-K, Huang C-J, Olbasa BW, Wu S-H, et al. Highly Concentrated Salt Electrolyte for a Highly Stable Aqueous Dual-Ion Zinc Battery. Applied Materials & Interfaces. 2022;14(32):36644-55.

26. Chang N, Li T, Li R, Wang S, Yin Y, Zhang H, et al. An aqueous hybrid electrolyte for low-temperature zinc-based energy storage devices. The Royal Society of Chemistry. 2020;13(10):3527-35.

27. Li X, Wang H, Sun X, Li J, Liu Y-NJAAEM. Flexible wide-temperature zinc-ion battery enabled by an ethylene glycol-based organohydrogel electrolyte. Applied Materials & Interfaces. 2021;4(11):12718-27.

28. Naveed A, Yang H, Yang J, Nuli Y, Wang JJACIE. Highly reversible and rechargeable safe Zn batteries based on a triethyl phosphate electrolyte. Angewandte Chemie. 2019;58(9):2760-4.

29. Cao L, Li D, Hu E, Xu J, Deng T, Ma L, et al. Solvation structure design for aqueous Zn metal batteries. Journal of the American Chemical Society. 2020;142(51):21404-9.

30. Dong Y, Miao L, Ma G, Di S, Wang Y, Wang L, et al. Non-concentrated aqueous electrolytes with organic solvent additives for stable zinc batteries. The Royal Society of Chemistry. 2021;12(16):5843-52.

31. Zhang Y, Zhu M, Wu K, Yu F, Wang G, Xu G, et al. An in-depth insight of a highly reversible and dendrite-free

Zn metal anode in an hybrid electrolyte. Journal of Materials Chemistry A. 2021;9(7):4253-61.

32. Ma G, Miao L, Dong Y, Yuan W, Nie X, Di S, et al. Reshaping the electrolyte structure and interface chemistry for stable aqueous zinc batteries. Energy Storage Materials. 2022;47:203-10.

33. Wang P, Xie X, Xing Z, Chen X, Fang G, Lu B, et al. Mechanistic Insights of Mg2+-Electrolyte Additive for High-Energy and Long-Life Zinc-Ion Hybrid Capacitors. ADVANCED ENERGY MATERIALS. 2021;11(30):2101158.

34. Wang J, Zhang L, Zhang C, Zhang JJJops. Effects of bismuth ion and tetrabutylammonium bromide on the dendritic growth of zinc in alkaline zincate solutions. Journal of power sources. 2001;102(1-2):139-43.

35. Wan F, Zhang L, Dai X, Wang X, Niu Z, Chen JJNc. Aqueous rechargeable zinc/sodium vanadate batteries with enhanced performance from simultaneous insertion of dual carriers. Nature Communications. 2018;9(1):1656.

36. Hu Z, Zhang F, Zhao Y, Wang H, Huang Y, Wu F, et al. A Self-Regulated Electrostatic Shielding Layer toward Dendrite-Free Zn Batteries. ADVANCED MATERIALS. 2022;34(37):2203104.

37. Chang G, Liu S, Fu Y, Hao X, Jin W, Ji X, et al. Inhibition role of trace metal ion additives on zinc dendrites during plating and striping processes. ADVANCED MATERIALS INTERFACES. 2019;6(23):1901358.

38. Xu Y, Zhu J, Feng J, Wang Y, Wu X, Ma P, et al. A rechargeable aqueous zinc/sodium manganese oxides battery with robust performance enabled by Na2SO4 electrolyte additive. Energy Storage Materials. 2021;38:299-308.

39. Abdulla J, Cao J, Zhang D, Zhang X, Sriprachuabwong C, Kheawhom S, et al. Elimination of zinc dendrites by graphene oxide electrolyte additive for zinc-ion batteries. Applied Energy Materials. 2021;4(5):4602-9.

40. Bayaguud A, Luo X, Fu Y, Zhu CJAEL. Cationic surfactant-type electrolyte additive enables three-dimensional dendrite-free zinc anode for stable zinc-ion batteries. ACS Energy Letters. 2020;5(9):3012-20.

41. Yao R, Qian L, Sui Y, Zhao G, Guo R, Hu S, et al. A versatile cation additive enabled highly reversible zinc metal anode. ADVANCED ENERGY MATERIALS. 2022;12(2):2102780.

42. Lin Y, Mai Z, Liang H, Li Y, Yang G, Wang CJE, et al. Dendrite-free Zn anode enabled by anionic surfactant-

induced horizontal growth for highly-stable aqueous Zn-ion pouch cells. Energy & environmental Science. 2023;16(2):687-97.

43. Zhou W, Chen M, Tian Q, Chen J, Xu X, Han X, et al. Stabilizing zinc deposition with sodium lignosulfonate as an electrolyte additive to improve the life span of aqueous zinc-ion batteries. Journal of Colloid and Interface Science. 2021;601:486-94.

44. Lu H, Zhang X, Luo M, Cao K, Lu Y, Xu BB, et al. Amino acid-induced interface charge engineering enables highly reversible Zn anode. ADVANCED FUNCTIONAL MATERIALS. 2021;31(45):2103514.

45. Jin Y, Han KS, Shao Y, Sushko ML, Xiao J, Pan H, et al. Stabilizing zinc anode reactions by polyethylene oxide polymer in mild aqueous electrolytes. ADVANCED FUNCTIONAL MATERIALS. 2020;30(43):2003932.

46. Glatz H, Tervoort E, Kundu DJAam, interfaces. Unveiling critical insight into the Zn metal anode cyclability in mildly acidic aqueous electrolytes: implications for aqueous zinc batteries. Applied Materials & Interfaces. 2019;12(3):3522-30.

47. Owusu K, Pan X, Yu R, Qu L, Liu Z, Wang Z, et al. Introducing Na2SO4 in aqueous ZnSO4 electrolyte realizes superior electrochemical performance in zinc-ion hybrid capacitor. materialstoday Energy. 2020;18:100529.

48. Zhang N, Cheng F, Liu Y, Zhao Q, Lei K, Chen C, et al. Cation-deficient spinel ZnMn2O4 cathode in Zn (CF3SO3) 2 electrolyte for rechargeable aqueous Zn-ion battery. Journal of the American Chemical Society. 2016;138(39):12894-901.

49. Zhang C, Shin W, Zhu L, Chen C, Neuefeind JC, Xu Y, et al. The electrolyte comprising more robust water and superhalides transforms Zn-metal anode reversibly and dendrite-free. carbon energy. 2021;3(2):339-48.

50. Wang L, Zhang Y, Hu H, Shi H-Y, Song Y, Guo D, et al. A Zn (ClO4) 2 electrolyte enabling long-life zinc metal electrodes for rechargeable aqueous zinc batteries. Applied Materials & Interfaces. 2019;11(45):42000-5.

51. Li W, Wang K, Zhou M, Zhan H, Cheng S, Jiang KJAam, et al. Advanced low-cost, high-voltage, long-life aqueous hybrid sodium/zinc batteries enabled by a dendrite-free zinc anode and concentrated electrolyte. Applied Materials & Interfaces. 2018;10(26):22059-66.

52. Zhu Y, Yin J, Zheng X, Emwas A-H, Lei Y, Mohammed OF, et al. Concentrated dual-cation electrolyte strategy for aqueous zinc-ion batteries. The Royal Society of Chemistry. 2021;14(8):4463-73.

53. Chen S, Lan R, Humphreys J, Tao SJESM. Salt-concentrated acetate electrolytes for a high voltage aqueous Zn/MnO2 battery. Energy Storage Materials. 2020;28:205-15.

54. Xu W, Zhao K, Huo W, Wang Y, Yao G, Gu X, et al. Diethyl ether as self-healing electrolyte additive enabled long-life rechargeable aqueous zinc ion batteries. Nano Energy. 2019;62:275-81.

55. Huang H, Xie D, Zhao J, Rao P, Choi WM, Davey K, et al. Boosting Reversibility and Stability of Zn Anodes via Manipulation of Electrolyte Structure and Interface with Addition of Trace Organic Molecules. ADVANCED ENERGY MATERIALS. 2022;12(38):2202419.

56. Liu Z, Wang R, Ma Q, Wan J, Zhang S, Zhang L, et al. A Dual-Functional Organic Electrolyte Additive with Regulating Suitable Overpotential for Building Highly Reversible Aqueous Zinc Ion Batteries. ADVANCED FUNCTIONAL MATERIALS. 2023:2214538.

57. Li R, Li M, Chao Y, Guo J, Xu G, Li B, et al. Hexaoxacyclooctadecane induced interfacial engineering to achieve dendrite-free Zn ion batteries. Energy Storage Materials. 2022;46:605-12.

58. Ma G, Di S, Wang Y, Yuan W, Ji X, Qiu K, et al. Zn metal anodes stabilized by an intrinsically safe, dilute, and hydrous organic electrolyte. Energy Storage Materials. 2023;54:276-83.

59. Cao J, Zhang D, Chanajaree R, Yue Y, Zeng Z, Zhang X, et al. Stabilizing zinc anode via a chelation and desolvation electrolyte additive. ADVANCED POWDER MATERIALS. 2022;1(1):100007.

60. Qin R, Wang Y, Zhang M, Wang Y, Ding S, Song A, et al. Tuning Zn2+ coordination environment to suppress dendrite formation for high-performance Zn-ion batteries. Nano Energy. 2021;80:105478.

61. Zhou X LY, Zhang Q, Miao L, Zhang K, Yan Z, Li F, Chen J. Exploring the interfacial chemistry between zinc anodes and aqueous electrolytes via an in situ visualized characterization system. ACS Applied Materials & Interfaces. 2020;12(49):55476-82.

62. Hao J, Yuan L, Ye C, Chao D, Davey K, Guo Z, et al. Boosting zinc electrode reversibility in aqueous electrolytes by using low-cost antisolvents. Angewandte Chemie. 2021;60(13):7366-75.

63. Shi J XK, Liu L, Liu C, Zhang Q, Li L, Zhou X, Liang J, Tao Z. Ultrahigh coulombic efficiency and long-life aqueous Zn anodes enabled by electrolyte additive of acetonitrile. Electrochimica Acta. 2020:358:136937.

64. Wang N YY, Qiu X, Dong X, Wang Y, Xia Y. Stabilized rechargeable aqueous zinc batteries using ethylene glycol as water blocker. ChemSusChem. 2020;13(20):5556-64.

65. Hou Z TH, Gao Y, Li M, Lu Z, Zhang B. Tailoring desolvation kinetics enables stable zinc metal anodes. Journal of Materials Chemistry A. 2020;8(37):19367-74.

66. Etman AS CM, Sun J, Younesi R. Acetonitrile-Based Electrolytes for Rechargeable Zinc Batteries. Energy Technology. 2020;8(9):2000358.

67. Song X HH, Shiraz MH, Zhu H, Khosrozadeh A, Liu J. Enhanced reversibility and electrochemical window of Zn-ion batteries with an acetonitrile/water-in-salt electrolyte. Chemical Communications. 2021;57(10):1246-9.

68. Nigatu TA, Bezabh HK, Taklu BW, Olbasa BW, Weng Y-T, Wu S-H, et al. Synergetic effect of water-in-bisalt electrolyte and hydrogen-bond rich additive improving the performance of aqueous batteries. Journal of power sources. 2021;511:230413.

69. Liu S, Mao J, Pang WK, Vongsvivut J, Zeng X, Thomsen L, et al. Tuning the electrolyte solvation structure to suppress cathode dissolution, water reactivity, and Zn dendrite growth in zinc-ion batteries. ADVANCED FUNCTIONAL MATERIALS. 2021;31(38):2104281.

70. Naveed A, Yang H, Shao Y, Yang J, Yanna N, Liu J, et al. A highly reversible Zn anode with intrinsically safe organic electrolyte for long-cycle-life batteries. ADVANCED MATERIALS. 2019;31(36):1900668.

71. Cui J, Liu X, Xie Y, Wu K, Wang Y, Liu Y, et al. Improved electrochemical reversibility of Zn plating/stripping: a promising approach to suppress water-induced issues through the formation of H-bonding. materialstoday Energy. 2020;18:100563.

72. Feng R CX, Qiu Q, Wu J, Huang J, Liu J, Liu Y. Cyclic Ether–Water Hybrid Electrolyte-Guided Dendrite-Free Lamellar Zinc Deposition by Tuning the Solvation Structure for High-Performance Aqueous Zinc-Ion Batteries. ACS Applied Materials & Interfaces. 2021;13(34):40638-47.

73. Feng D, Cao F, Hou L, Li T, Jiao Y, Wu PJS. Immunizing aqueous Zn batteries against dendrite formation and side reactions at various temperatures via electrolyte additives. nano micro small. 2021;17(42):2103195.

74. Zhang Q, Luan J, Fu L, Wu S, Tang Y, Ji X, et al. The three-dimensional dendrite-free zinc anode on a copper mesh with a zinc-oriented polyacrylamide electrolyte additive. Angewandte Chemie. 2019;58(44):15841-7.

75. Du H, Wang K, Sun T, Shi J, Zhou X, Cai W, et al. Improving zinc anode reversibility by hydrogen bond in hybrid aqueous electrolyte. chemical Engineering Journal. 2022;427:131705.

76. Wang A, Zhou W, Huang A, Chen M, Tian Q, Chen JJJoC, et al. Developing improved electrolytes for aqueous zinc-ion batteries to achieve excellent cyclability and antifreezing ability. Journal of Colloid and Interface Science. 2021;586:362-70.

77. Wu Y, Zhu Z, Shen D, Chen L, Song T, Kang T, et al. Electrolyte engineering enables stable Zn-ion deposition for long-cycling life aqueous Zn-ion batteries. Energy Storage Materials. 2022;45:1084-91.

78. Deng W, Xu Z, Wang XJESM. High-donor electrolyte additive enabling stable aqueous zinc-ion batteries. Energy Storage Materials. 2022;52:52-60.

79. Luo M, Wang C, Lu H, Lu Y, Xu BB, Sun W, et al. Dendrite-free zinc anode enabled by zinc-chelating chemistry. Energy Storage Materials. 2021;41:515-21.

80. Ma L, Chen S, Li H, Ruan Z, Tang Z, Liu Z, et al. Initiating a mild aqueous electrolyte Co 3 O 4/Zn battery with 2.2 V-high voltage and 5000-cycle lifespan by a Co (III) rich-electrode. Energy & Environmental Science. 2018;11(9):2521-30.

81. Guo X, Zhang Z, Li J, Luo N, Chai G-L, Miller TS, et al. Alleviation of dendrite formation on zinc anodes via electrolyte additives. ACS Energy Letters. 2021;6(2):395-403.

82. Zeng X, Mao J, Hao J, Liu J, Liu S, Wang Z, et al. Electrolyte design for in situ construction of highly Zn2+-conductive solid electrolyte interphase to enable high-performance aqueous Zn-ion batteries under practical conditions. ADVANCED MATERIALS. 2021;33(11):2007416.

83. Wu C, Sun C, Ren K, Yang F, Du Y, Gu X, et al. 2-methyl imidazole electrolyte additive enabling ultra-stable Zn anode. chemical Engineering Journal. 2023;452:139465.

84. Hao J, Li B, Li X, Zeng X, Zhang S, Yang F, et al. An in-depth study of Zn metal surface chemistry for advanced aqueous Zn-ion batteries. ADVANCED MATERIALS. 2020;32(34):2003021.

85. Han J, Euchner H, Kuenzel M, Hosseini SM, Gross A, Varzi A, et al. A thin and uniform fluoride-based artificial interphase for the zinc metal anode enabling reversible Zn/MnO2 batteries. ACS Energy Letters. 2021;6(9):3063-71.

86. Wang N, Zhang Y, Yuan J, Hu L, Sun M, Li Z, et al. A Synergistic Strategy of Organic Molecules Introduced a High Zn2+ Flux Solid Electrolyte Interphase for Stable Aqueous Zinc-Ion Batteries. ACS Applied Materials & Interfaces. 2022;14(42):48081-90.

87. Yang Y, Qu G, Wei H, Wei Z, Liu C, Lin Y, et al. Weakly Solvating Effect Spawning Reliable Interfacial Chemistry for Aqueous Zn/Na Hybrid Batteries. ADVANCED ENERGY MATERIALS. 2023;13(12):2203729.

88. Li D, Cao L, Deng T, Liu S, Wang CJACIE. Design of a solid electrolyte interphase for aqueous Zn batteries. Angewandte Chemie. 2021;60(23):13035-41.

89. Zeng X, Xie K, Liu S, Zhang S, Hao J, Liu J, et al. Bio-inspired design of an in situ multifunctional polymeric solid–electrolyte interphase for Zn metal anode cycling at 30 mA cm− 2 and 30 mA h cm− 2. Energy & environmental Science. 2021;14(11):5947-57.

90. Cao L, Li D, Pollard T, Deng T, Zhang B, Yang C, et al. Fluorinated interphase enables reversible aqueous zinc battery chemistries. Nature Nanotechnology. 2021;16(8):902-10.

91. Guan K, Tao L, Yang R, Zhang H, Wang N, Wan H, et al. Anti-corrosion for reversible zinc anode via a hydrophobic interface in aqueous zinc batteries. ADVANCED ENERGY MATERIALS. 2022;12(9):2103557.

92. Qiu Q, Chi X, Huang J, Du Y, Liu YJC. Highly stable plating/stripping behavior of zinc metal anodes in aqueous zinc batteries regulated by quaternary ammonium cationic salts. ChemElectroChem. 2021;8(5):858-65.

93. Hu Q, Hu J, Li Y, Zhou X, Ding S, Zheng Q, et al. Insights into Zn anode surface chemistry for dendrite-free Zn ion batteries. The Royal Society of Chemistry. 2022;10(20):11288-97.

94. Hao J, Long J, Li B, Li X, Zhang S, Yang F, et al. Toward high-performance hybrid Zn-based batteries via deeply understanding their mechanism and using electrolyte additive. ADVANCED FUNCTIONAL MATERIALS. 2019;29(34):1903605.

95. Meng Q, Zhao R, Cao P, Bai Q, Tang J, Liu G, et al. Stabilization of Zn anode via a multifunctional cysteine additive. chemical Engineering Journal. 2022;447:137471.

96. Miao Z, Liu Q, Wei W, Zhao X, Du M, Li H, et al. Unveiling unique steric effect of threonine additive for highly reversible Zn anode. Nano Energy. 2022:107145.

97. Yan M, Dong N, Zhao X, Sun Y, Pan HJAEL. Tailoring the stability and kinetics of Zn anodes through trace organic polymer additives in dilute aqueous electrolyte. ACS Energy Letters. 2021;6(9):3236-43.

98. Niu B, Li Z, Luo D, Ma X, Yang Q, Liu Y-E, et al. Nano-scaled hydrophobic confinement of aqueous electrolyte by a nonionic amphiphilic polymer for long-lasting and wide-temperature Zn-based energy storage. Energy & environmental Science. 2023;16(4):1662-75.

99. Chao D, Zhou W, Xie F, Ye C, Li H, Jaroniec M, et al. Roadmap for advanced aqueous batteries: From design of materials to applications. Science Advances. 2020;6(21):eaba4098.

100. Fang G, Zhou J, Pan A, Liang SJAEL. Recent advances in aqueous zinc-ion batteries. ACS Energy Letters. 2018;3(10):2480-501.

101. Song M, Tan H, Chao D, Fan HJJAFM. Recent advances in Zn-ion batteries. ADVANCED FUNCTIONAL MATERIALS. 2018;28(41):1802564.

102. Zeng Z, Zeng Y, Sun L, Mi H, Deng L, Zhang P, et al. Long cyclic stability of acidic aqueous zinc-ion batteries

achieved by atomic layer deposition: the effect of the induced orientation growth of the Zn anode. The Royal Society of Chemistry 2021;13(28):12223-32.

103. Yan H, Li S, Nan Y, Yang S, Li BJAEM. Ultrafast zinc–ion–conductor interface toward high-rate and stable zinc metal batteries. ADVANCED ENERGY MATERIALS. 2021;11(18):2100186.

104. Yang Q, Liang G, Guo Y, Liu Z, Yan B, Wang D, et al. Do zinc dendrites exist in neutral zinc batteries: a developed electrohealing strategy to in situ rescue in-service batteries. ADVANCED MATERIALS. 2019;31(43):1903778.

105. Kao-ian W, Mohamad AA, Liu WR, Pornprasertsuk R, Siwamogsatham S, Kheawhom SJB, et al. Stability Enhancement of Zinc-Ion Batteries Using Non-Aqueous Electrolytes. Chemistry Europe. 2022;5(5):e202100361.

106. Cao J, Zhang D, Chanajaree R, Yue Y, Zeng Z, Zhang X, et al. Stabilizing zinc anode via a chelation and desolvation electrolyte additive. Energy Powder Materials. 2022;1(1):100007.

107. Zheng X, Ahmad T, Chen WJESM. Challenges and strategies on Zn electrodeposition for stable Zn-ion batteries. Energy Storage Materials. 2021;39:365-94.

108. Liu C, Xie X, Lu B, Zhou J, Liang SJAEL. Electrolyte strategies toward better zinc-ion batteries. ACS Energy Letters. 2021;6(3):1015-33.

109. Yang J, Yan H, Hao H, Song Y, Li Y, Liu Q, et al. Synergetic modulation on solvation structure and electrode interface enables a highly reversible zinc anode for zinc–iron flow batteries. ACS Energy Letters. 2022;7(7):2331-9.

110. Qiu H, Du X, Zhao J, Wang Y, Ju J, Chen Z, et al. Zinc anode-compatible in-situ solid electrolyte interphase via cation solvation modulation. Nature Communications. 2019;10(1):5374.

111. Westman K, Dugas R, Jankowski P, Wieczorek W, Gachot G, Morcrette M, et al. Diglyme based electrolytes for sodium-ion batteries. ACS Applied Energy Materials. 2018;1(6):2671-80.

112. Han S-D, Rajput NN, Qu X, Pan B, He M, Ferrandon MS, et al. Origin of electrochemical, structural, and transport properties in nonaqueous zinc electrolytes. ACS Applied Materials & Interfaces. 2016;8(5):3021-31.

113. Shah D, Mjalli FSJPCCP. Effect of water on the thermo-physical properties of Reline: An experimental and molecular simulation based approach. The Royal Society of Chemistry. 2014;16(43):23900-7.

114. Chen Y, Gong F, Deng W, Zhang H, Wang XJESM. Dual-function electrolyte additive enabling simultaneous electrode interface and coordination environment regulation for zinc-ion batteries. Energy Storage Materials. 2023;58:20-9.

115. Di S, Nie X, Ma G, Yuan W, Wang Y, Liu Y, et al. Zinc anode stabilized by an organic-inorganic hybrid solid electrolyte interphase. Energy Storage Materials. 2021;43:375-82.